

INAUGURAL - DISSERTATION

zur

Erlangung der Doktorwürde

der

Gesamtfakultät für Mathematik, Ingenieur- und

Naturwissenschaften

der

Ruprecht-Karls-Universität Heidelberg

Vorgelegt von

M.Sc. Bahareh Ebrahimi Pour

geboren in Ahvaz, Iran

Tag der mündlichen Prüfung: 10.06.2025

Structures and Functions of Synthetic and Native Biomembranes

Gutachter:

Prof. Dr. Motomu Tanaka

Prof. (apl.) Dr. Reiner Dahint

Structures and Functions of Synthetic and Native Biomembranes

The main objective of this thesis is to quantitatively investigate the structure and function of a new class of artificial membrane models and two types of native biomembranes by the combination of unique physical techniques.

In chapter 4, the specific recognition of heavy metal ions by plant-inspired polymer (pAA-Cys5) mimicking plant phytochelatin protein was quantitatively detected by using two experimental techniques. **In section 4.1**, the binding of Cd^{2+} to DOPE-pAA-Cys5 was detected by using a high electron mobility transistor (HEMT) device based on GaN/AlGaN/GaN heterostructures. By precisely controlling the average intermolecular distance between pAA-Cys5 brushes, the sensitivity of the pAA-Cys5-functionalized device could be quantitatively assessed from the change in carrier mobility in the two-dimensional electron gas (2DEG) layer. **In section 4.2**, simultaneous grazing-incidence X-ray fluorescence (GIXF) and specular X-ray reflectivity (XRR) unraveled the spatial distribution of Cd^{2+} ions in the close proximity of the air/water interface, and the ion specificity of pAA-Cys5 was assessed by comparison with Ca^{2+} ions.

In chapter 5, the structures of native biomembranes in the direction perpendicular to the membrane surface were characterized using high-energy XRR, neutron reflectivity (NR), and attenuated total reflection Fourier transform infrared (ATR-FTIR) spectroscopy. The direct spreading of native biomembranes enabled the maintenance of the amount, composition, and orientation of membrane proteins, which cannot be achieved by artificially reconstituted membrane systems. In this study, two types of membrane systems were investigated; sarcoplasmic reticulum membrane purified from rabbit muscle (**section 5.1**) and healthy and malaria-infected human erythrocyte ghost membranes (**section 5.2**). Ex-situ combination of XRR and ATR-FTIR could unravel both structural features of membranes and spectroscopic fingerprints of membrane proteins in SR membranes. Moreover, NR of healthy and malaria-infected erythrocyte membranes can be attributed to the clusters of adhesion proteins. The obtained results demonstrate that the complementary combination of surface-sensitive techniques is a powerful tool for the characterization of structures and functions of artificial and native membranes.

Strukturen und Funktionen synthetischer und nativer Biomembranen

Das Ziel dieser Arbeit ist es, die Struktur und Funktion einer neuen Klasse von künstlichen Membranmodellen und zwei Arten von nativen Biomembranen durch die Kombination neuartiger physikalischer Techniken quantitativ zu untersuchen.

In Kapitel 4 wurde die spezifische Erkennung von Schwermetallionen durch ein von Pflanzen inspiriertes Polymer (pAA-Cys5), welches das pflanzliche Phytochelatin-Protein nachahmt, mit Hilfe von zwei experimentellen Techniken quantitativ untersucht.

Im Abschnitt 4.1 wurde die Bindung von Cd^{2+} an DOPE-pAA-Cys5 mit Hilfe eines High-Electron-Mobility-Transistors (HEMT) auf der Grundlage von GaN/AlGaIn/GaN-Heterostrukturen nachgewiesen. Durch die genaue Kontrolle des durchschnittlichen intermolekularen Abstands zwischen den pAA-Cys5-Bürsten konnte die Empfindlichkeit der pAA-Cys5-funktionalisierten Sensoroberfläche anhand der Änderung der Ladungsträgerbeweglichkeit in der zweidimensionalen Elektronengasschicht (2DEG) quantitativ bewertet werden. **Im Abschnitt 4.2** wurden mittels gleichzeitiger Grazing-Incidence-Röntgenfluoreszenz (GIXF) und Röntgenreflektometrie (XRR) die räumliche Verteilung der Cd^{2+} -Ionen in unmittelbarer Nähe der Luft/Wasser-Grenzfläche analysiert, wobei die Ionenspezifität von pAA-Cys5 durch den Vergleich mit Ca^{2+} -Ionen bewertet wird.

Kapitel 5 widmet sich der strukturellen Charakterisierung nativer Biomembranen in der Richtung senkrecht zur Membranoberfläche durch den Einsatz von hochenergetischer Röntgenreflektometrie (XRR), Neutronenreflektometrie (NR) und abgeschwächter Totalreflexions-Fourier-Transformations-Infrarotspektroskopie (ATR-FTIR). Die direkte Beschichtung nativer Biomembranen garantiert die Beibehaltung ihrer natürlichen Proteinzusammensetzung, ihrer Orientierung und Menge. Diese Aspekte können in künstlich gebildeten Membransystemen nicht vollständig reproduziert werden. In dieser Arbeit wurden zwei Arten von Membransystemen untersucht, nämlich isolierte Membranen des Sarkoplasmatischen Retikulums aus Kaninchenmuskelgewebe (**Abschnitt 5.1**) sowie gesunde und malariainfizierte menschliche Erythrozyten, sogenannte "Geistermembranen" (**Abschnitt 5.2**). Die Kombination aus XRR und ATR-FTIR ermöglicht eine de-

taillierte strukturelle und spektroskopische Charakterisierung der Membranproteine der SR-Membran. Zudem ließen sich durch NR-Untersuchungen von gesunden und malaria-infizierten Erythrozytenmembranen charakteristische Cluster von Adhäsionsproteinen nachweisen.

Die erhaltenen Ergebnisse zeigen, dass die gezielte Kombination oberflächensensitiver Techniken ein leistungsstarkes Instrument zur umfassenden Charakterisierung von Strukturen und Funktionen künstlicher und nativer Membranen darstellt.

Acknowledgements

I would like to thank

Prof. Dr. Motomu Tanaka for his continuous support, scientific guidance, and patience during discussions. I am grateful for the opportunities to participate in experiments at the ILL and ESRF in Grenoble and to broaden my scientific experience at Kyoto University.

Prof. (apl.) Dr. Reiner Dahint for kindly acting as the second referee for this work and my final examination and collaboration work.

Prof. Dr. Martin Eickhoff for providing the HEMT substrates and for the valuable collaboration.

Dr. Masakai Nakahata for kindly providing the DOPE-pAA-Cys5 polymer.

Dr. Stefan Kaufmann and **Dr. Wasim Abuillan** for insightful discussions, proofreading of my thesis, and enjoyable conversations, which made this journey both productive and motivating.

Dr. Akihisa Yamamoto for his guidance and support during my stay in Japan.

Dr. Oleg Konovalov and **Alexei Vorobiev** for their help with the scattering experiments in Grenoble (ESFR and ILL) and for being available to answer any questions we had.

Dr. Judith Thoma, **Dr. Felix Weissenfeld**, and **Dr. Sven Mehlhose** for the insightful discussions, fun conversations, and assistance with proofreading.

Dr. Andreas Stöcklin for his support and valuable input during the publication process of my first paper.

AK Tanaka for creating a positive atmosphere in the office and lab, and Zahra for the good times we shared.

My family for their constant support and encouragement throughout this journey.

Especially my sisters, Najmeh, Neda, and Mahtab, who have always been there for me and have been my biggest cheerleaders throughout my life.

My husband, Robert, who has always motivated me during difficult times, brightened my days with thoughtful gifts and surprises and encouraged me to keep moving forward.

Contents

1	Introduction	2
1.1	Specific ion recognition by plant-inspired polymers	3
1.2	Structural Analysis of Native Biomembranes	9
2	Theory	12
2.1	Self-assembly of membranes	12
2.2	Polymerbrushes	14
2.3	Fundamentals on GaN-based HEMTs	18
2.3.1	Crystallographic structure	18
2.3.2	Space charge regions of Semiconductors-Electrolytes	21
2.3.3	Current-Voltage (I-V) Characteristic of transistors	22
2.4	High-Energy specular X-ray and Neutron reflectivity	23
2.4.1	Fresnel reflectivity of a flat surface	26
2.4.2	Reflection from a layered sample	27
2.5	Grazing incidence X-ray fluorescence (GIXF)	28
2.6	Atomic Force Microscopy (AFM)	29
2.7	Ellipsometry	31
2.8	Contact Angle	32
3	Materials and Methods	34
3.1	Materials	34
3.1.1	Chemicals	34
3.1.2	Substrates and Sample preparation	34
3.1.3	Fabrication of supported membrane by vesicle fusion	35
3.1.4	Octadecyltrimethoxysilane (ODTMS) functionalization of substrates	36
3.1.5	Trimethylsilylcellulose (TMSC) substrate coating	36
3.1.6	Erythrocyte ghost membrane preparation	36
3.1.7	Isolation of Sarcoplasmic Reticulum (SR) vesicle	37

CONTENTS

3.1.8	Analysis of SR membrane Protein by SDS-PAGE	38
3.1.9	Immunofluorescence imaging of Sarcoplasmic reticulum and Erythrocyte membrane	38
3.1.10	Synthesis of DOPE-pAA-Cys5 lipopolymer	39
3.2	Methods	40
3.2.1	Contact angle	40
3.2.2	Atomic force microscopy (AFM)	40
3.2.3	Specular X-ray reflectivity (XRR) and neutron reflectivity (NR)	40
3.2.4	Grazing incidence x-ray fluorescence (GIXF)	41
3.2.5	Ellipsometer	42
3.2.6	I-V measurement of DOPC/PE-pAA-Cys5 membrane by source/measurement unit	42
4	Ion-specific recognition on the membrane surface	44
4.1	Detection of Heavy Metal Ions in Aqueous Environment Using GAN/AlGaN High Electron Mobility Transistors Functionalized with Plant-Inspired Polymers	44
4.1.1	Characterization of lipid monolayer incorporating DOPE-pAA-Cys5	44
4.1.2	Sensing of Cd ²⁺ and Ca ²⁺ ions in the presence of supporting salt (buffer 1)	45
4.1.3	Sensitivity and Selectivity of Sensor Response in the Presence and Absence of Supporting salt	49
4.2	Specific localization of ions in Plant-Inspired polymers at the air/water interface	52
4.2.1	Pressure-Area Isotherms of DOPE-pAA-Cys5 monolayer	52
4.2.2	Influence of M ²⁺ ions on pAA-Cys5 monolayer (XRR and GIXF)	54
5	Structural Characterization of Native Biomembranes	61
5.1	Structural and Spectroscopic characterization of supported Sarcoplasmic Reticulum (SR) Membranes on solid substrates	61
5.1.1	Immunofluorescence staining and SDS-PAGE of SR membrane	61

CONTENTS

5.1.2	Structural Analysis of Supported SR Membranes Using XRR and NR	62
5.1.3	Characterization of supported SR membranes after enzymatic degradation using XRR and NR	65
5.1.4	In situ Monitoring of Proteolytic Digestion by ATR-FTIR	67
5.2	Fine-structure characterization of polymer-supported healthy and infected ghost cell membrane by Neutron Reflectivity	70
5.2.1	Preanalysis of polymer support and erythrocyte ghost membrane	70
5.2.2	Cellulose characterization in dry and hydrated state	71
5.2.3	Healthy and infected erythrocyte ghost membrane on cellulose	75
6	Conclusion	78
7	Appendix	81
7.1	Ion sensing eGFP monolayer on HEMT	81
7.1.1	Introduction	81
7.1.2	Experimental	82
7.1.3	Result and Discussion	83
7.2	Structural and Spectroscopic characterization of supported Sarcoplasmic Reticulum (SR) Membranes on solid substrates (SI)	89
	References	103
	List of Figures	104
	List of Tables	108

1 Introduction

Biological membranes, which separate the intercellular from the extracellular space, are critical components of living systems. They consist mainly of lipids and membrane-associated proteins, such as integral-, peripheral-, and lipid-anchored proteins. These proteins occupy up to 50% of the cell membrane by weight [1].

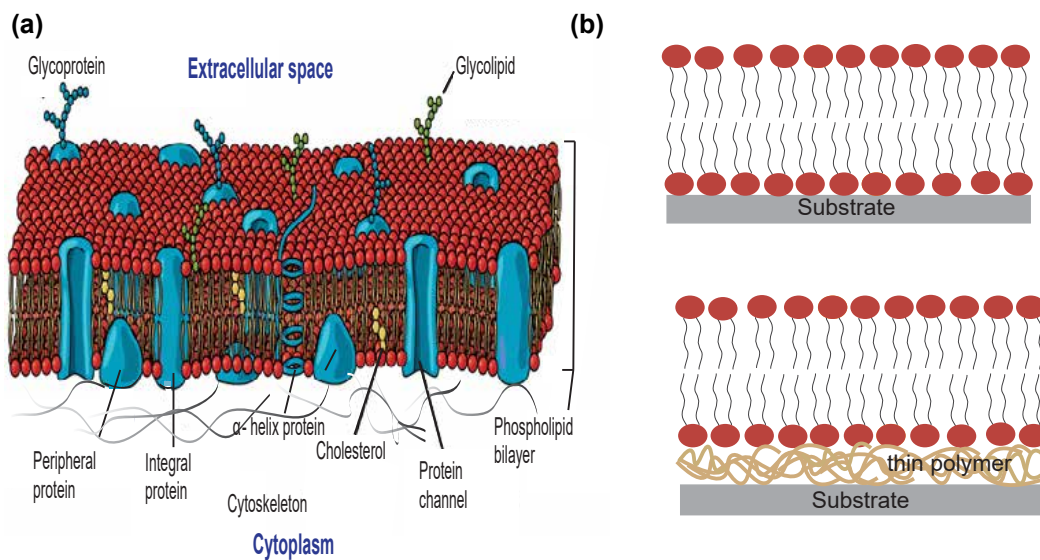


Figure 1.1: (a) Schematic-illustration of an eukaryotic cell membrane, adapted from [2], (b) Supported membranes on a solid substrate and a polymer support.

The outer surface of a cell membrane is coated with a variety of carbohydrate chains connected to the head groups of lipids and proteins, called glycocalyx, whereas the inner surface is coupled to cytoskeleton networks (Figure 1.1a). The lipid bilayer creates a fluid character, while the embedded proteins and carbohydrates are present for communication, transport, and reactions across the membrane. This structural arrangement makes the membrane a selective filter for nutrients, wastes, and metabolites by regulating many biochemical processes [3].

In 1925, Gorter and Gendel [4] introduced the lipid bilayer model as a structural description of the cell membrane as a double layer of lipids. Based on this, Singer and Nicolson [5] introduced the fluid mosaic model in 1972, representing the fluid nature of self-assembled

lipids and proteins [6]. As native cell membranes contain numerous molecular components, artificial membrane models have gained considerable interest over the past 50 years. The model membranes with the reduced number of components allow for the investigation of physical and chemical interactions within the membrane in a controlled environment.

Various models have been developed, among which planar lipid membranes deposited on solid surfaces have become one of the most widely used cell membrane models [7] [8] [3]. This model membrane can be deposited directly on a solid support, such as glass or silica, or a thin polymer layer (Figure 1.1b) [9] [3]. The structures of nm-thick lipid membranes on planar substrates can be characterized by a variety of different experimental methods, e.g. surface plasmon resonance (SPR) [10] [11], quartz crystal microbalance with dissipation control (QCM-D) [12] [13], X-ray reflectivity (XRR) [14] [15] and neutron reflectivity (NR) [16] [17]. Rossetti et al. demonstrated the deposition of phospholipid membranes on cellulose supports with different thicknesses and characterized the structures in the direction perpendicular to the surface by using high-energy specular X-ray reflectivity and neutron reflectivity [15]. Despite the major progress achieved by artificial membrane models, they have some fundamental problems. For example, artificial model membranes are not able to accommodate a large number of proteins, e.g., 50 wt%, like native membranes do [1]. Moreover, it is technically very difficult to incorporate different proteins in a controlled manner. One straightforward strategy to overcome these problems is to deposit native biomembranes on bare or on polymer-coated substrates [18].

The main objective of this thesis is to quantitatively investigate the structure and function of a new class of artificial membrane models and two types of native biomembranes by combining unique physical techniques.

1.1 Specific ion recognition by plant-inspired polymers

Plants have a highly abundant protein, phytochelatins, which selectively captures and detoxifies heavy metal ions in soil and groundwater (Figure 1.2a) [19]. Phytoremediation, the use of plants for environmental remediation, has already been applied, and its application

prospects have been growing in recent years [20].

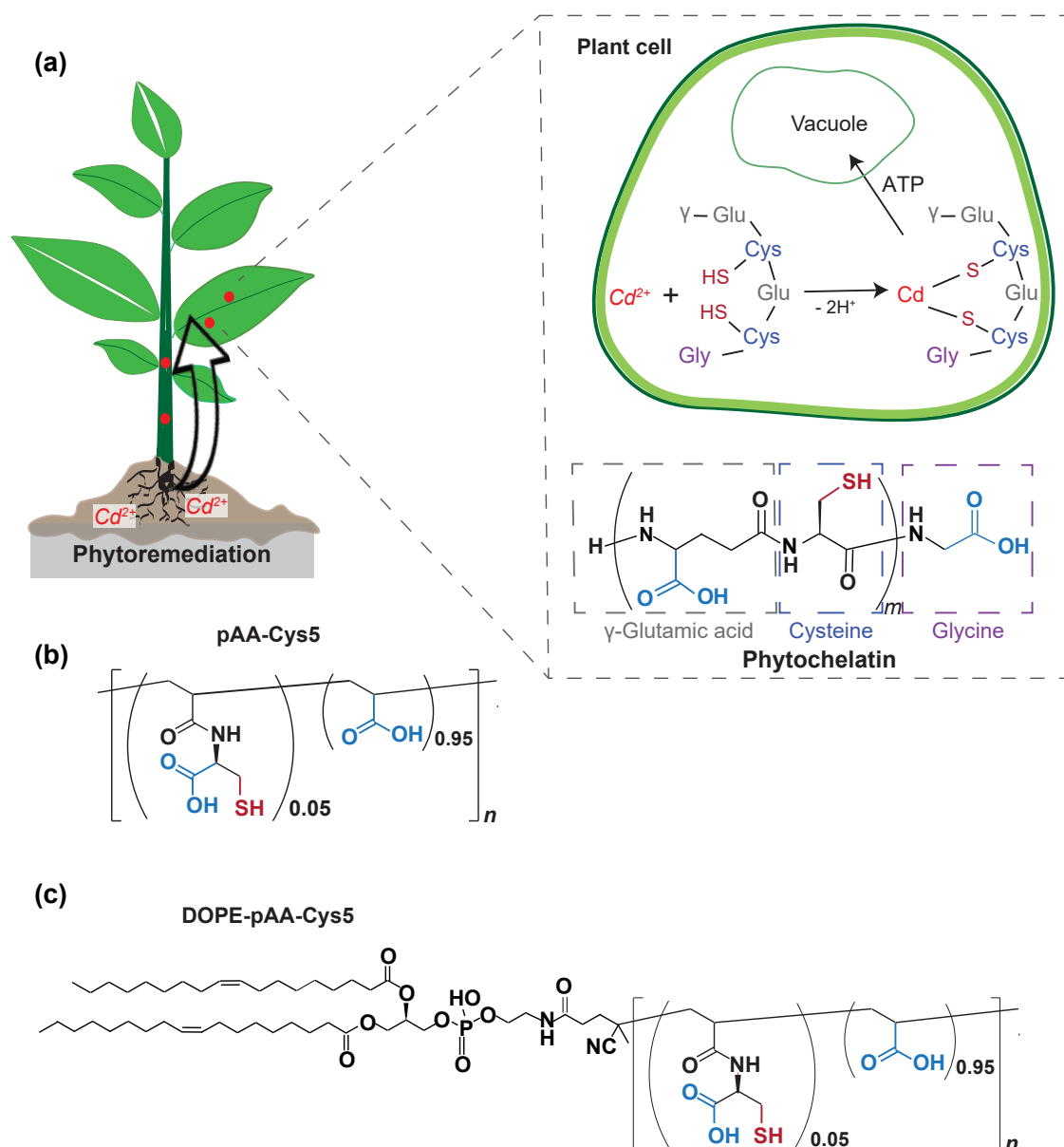


Figure 1.2: Plant-inspired material for the selective capture of heavy metal ions (e.g., Cd^{2+}). (a) Neutralization of Cd^{2+} ions by phytochelatins in plant cells, (b) Chemical structure of phytochelatins-inspired polymer (pAA-Cys5) and (c) Lipopolymer (DOPE-pAA-Cys5).

Inspired by the structures of phytochelatins consisting of oligomers of glutathione, Nakahata et al. synthesized polyacrylic acid-based copolymers containing carboxylate and thiolate moieties, called pAA-Cys5 (Figure 1.2b) [19]. The copolymer was synthesized by radical copolymerization of acrylic acid (AA) and cysteine-coupled AA by the reversible

addition-fragmentation chain transfer (RAFT) method. Using titration calorimetry, they demonstrated that the coexistence of both moieties is necessary to achieve an outstanding affinity to Cd^{2+} ions, which is characterized by a dissociation constant, $K_D \sim 1 \text{ nM}$ for Cd^{2+} ion. Notably, pAA-Cys5 has four to five orders of magnitude lower affinity to abundant divalent cations like Ca^{2+} and Mg^{2+} , which enables the treatment of polluted groundwater [19].

In chapter 4, the specific recognition of heavy metal ions by phytochelatin-inspired pAA-Cys5 was quantitatively detected by using two unique physical techniques. In this study, pAA-Cys5 attached to the phospholipid head group (DOPE-pAA-Cys5), Figure 1.2c) was used in order to optimize the arrangement of lipids and lipopolymers by self-assembly [21] [19]. The lipopolymer used in this study was synthesized by Dr. Masaki Nakahata (Osaka University, Japan). In this study, the specific binding of Cd^{2+} ions to pAA-Cys5 was detected electrochemically by using a GaN-based transistor (section 4.1) and surface-sensitive X-ray fluorescence of Cd near the air/water interface (section 4.2).

In section 4.1, the specific binding of Cd^{2+} to DOPE-pAA-Cys5 was detected by using a high electron mobility transistor (HEMT) device based on GaN/AlGaIn/GaN heterostructures. GaN is known to possess outstanding chemical and electrochemical stability over a wide frequency range [22]. The electronic properties of GaN can be modulated flexibly by doping and band gap engineering by alloying with In or Al. Here, GaN surfaces were functionalized by successive wet chemical oxidation and silanization [23] [24]. Finally, the monolayers of lipid/lipopolymer mixtures can be deposited on hydrophobic, silane-coated GaN surfaces by vesicle fusion (Figure 1.3a) [25] [21]. Owing to the self-assembly of lipid and lipopolymer molecules, the average intermolecular distance between pAA-Cys5 brushes, $\langle d \rangle$ can be controlled with nm accuracy simply by adjusting the molar fraction of DOPE-pAA-Cys5 χ , $\langle d \rangle = \sqrt{\frac{A}{\chi}}$, by assuming that the area occupied by one lipid molecule A is 0.6 nm^2 [7]. The electrochemical sensing of Cd^{2+} ions to pAA-Cys5 was performed by measuring the current-voltage (I-V) characteristics using a self-built liquid cell [26]. As the device used in this study, fabricated by the group of Prof. Dr. Martin Eickhoff (University of Bremen), is an open-gate HEMT, the gate voltage was controlled

with respect to an Ag/AgCl reference electrode. The change in the surface charge density and, hence, the change in the surface potential caused by the binding of ions was detected as the change in carrier mobility in the two-dimensional electron gas layer (Figure 1.3b).

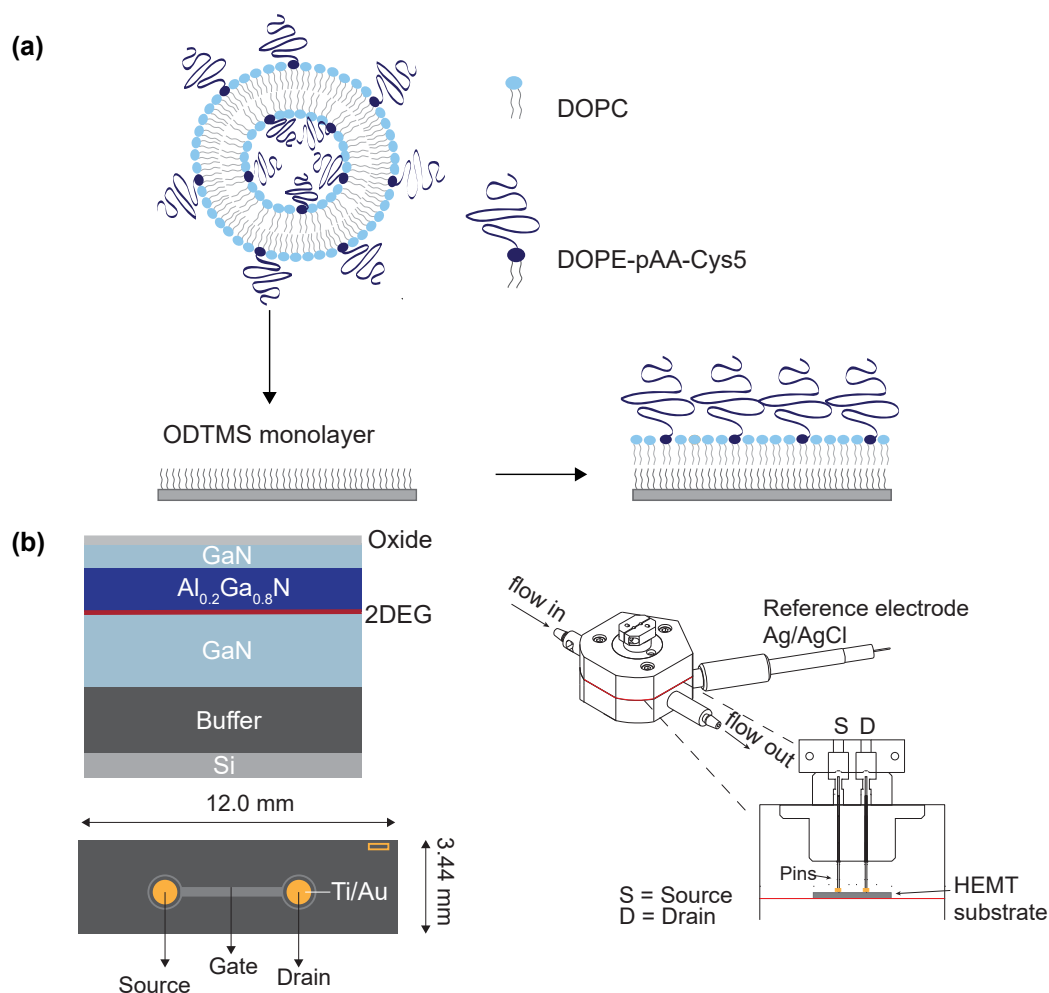


Figure 1.3: (a) Fabrication of a supported lipid monolayer incorporating DOPE-pAA-Cys5 on silanized GaN, (b) GaN/AlGaN/GaN heterostructure, device geometry, and electrochemical cell used in this study.

In section 4.2, the amount of Cd²⁺ ions captured by DOPE-pAA-Cys5 and their spatial distribution were detected by the simultaneous measurement of grazing-incidence X-ray fluorescence (GIXF) and specular X-ray reflectivity (XRR) at ID10 beamline of European Synchrotron Radiation Facility (ESRF) Grenoble, France (Figure 1.4a). The combination of GIXF and XRR enables the determination of the spatial distribution of

chemical elements from their emission spectra with Å accuracy [27] [28] [29]. Commonly used X-ray and neutron scattering experiments are not capable of localizing individual elements in nm-thick biological membranes because these techniques are sensitive to electron density and scattering length density. Here, a mixed monolayer of phospholipid containing DOPE-pAA-Cys5 was deposited at the air/water interface, and GIXF and XRR were measured simultaneously. By changing the angle of illumination across the critical angle of total reflection, the penetration depth of the evanescent field propagating into water is modulated. Namely, one can obtain the angular/depth-dependent X-ray fluorescence signals from different core levels of elements (Figure 1.4b), such as K-K α (3.3 keV), Ca-K α (3.7 keV), and Cd-L α (3.1 keV).

The depth profile of element $c_i(z)$ can be determined using the measured fluorescence signal $I_i^f(z, \alpha)$ and the illumination profile $I^{ill}(z, \alpha)$: $I_i^f \propto \int I^{ill}(z, \alpha) c_i(z) \exp(-z/L_i) dz$, where c_z represents the concentration of the element I at a depth z . The reduction of the fluorescence emission between position z and the detector is represented by the exponential term, where L indicates the attenuation length of water at the specific fluorescence line. Of note, the electron density profile is necessary to calculate the illumination profile, which is nothing but the electromagnetic wave reflected and refracted within the ultrathin films [30] [28]. In this study, the spatial distribution of Cd $^{2+}$ ions in the close proximity of the air/water interface was measured in the absence and presence of Cd $^{2+}$. To verify the specificity of Cd $^{2+}$ binding to pAA-Cy5, the corresponding data were collected in the presence of Ca $^{2+}$ ions.

1 INTRODUCTION

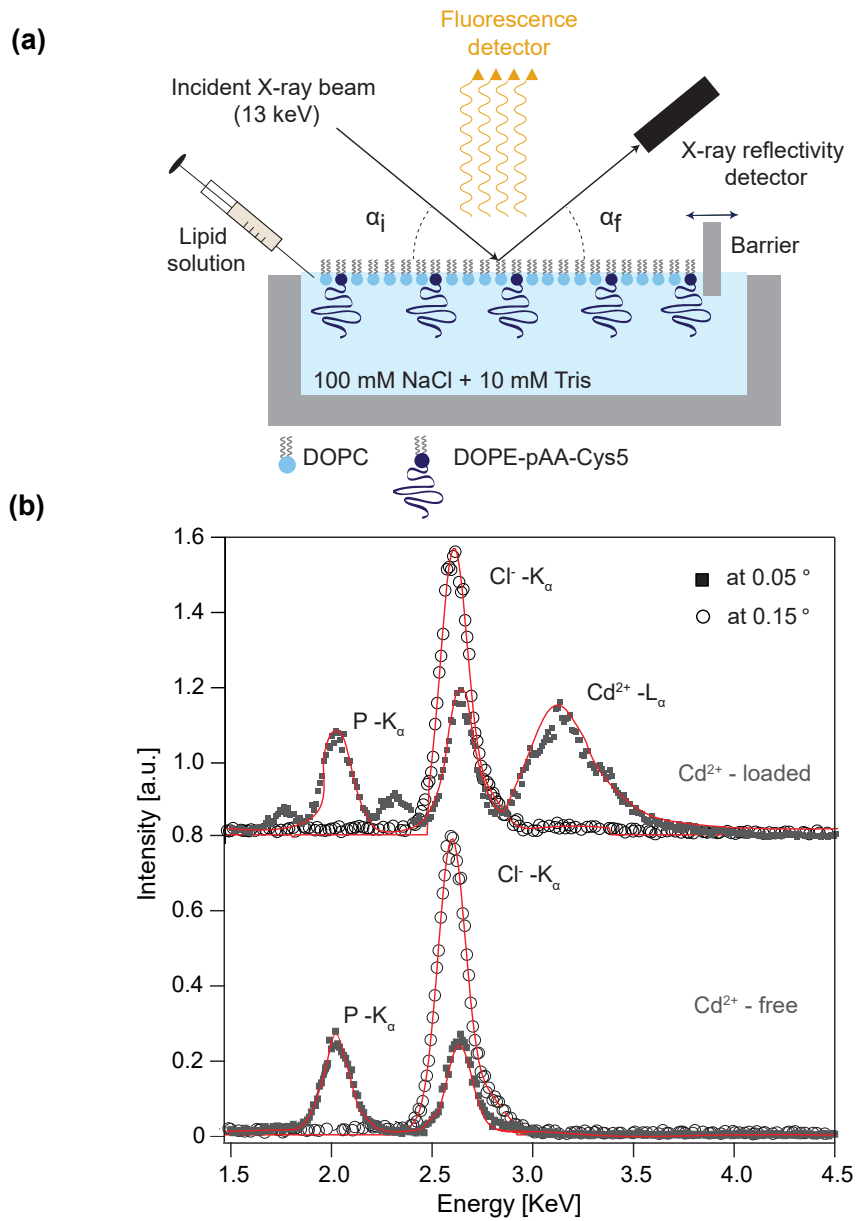


Figure 1.4: Fluorescence spectra of DOPC/DOPE-pAA-Cys5 monolayer on Cd^{2+} -free and Cd^{2+} loaded buffer.

1.2 Structural Analysis of Native Biomembranes

In chapter 5, the structures of native biomembranes in the direction perpendicular to the membrane surface were characterized by using high-energy XRR, neutron reflectivity (NR), and attenuated total reflection Fourier transform infrared (ATR-FTIR) spectroscopy. Nature strictly controls the amount, distribution, and orientation of various membrane-associated proteins *in vivo*. Artificial membrane systems can accommodate membrane proteins by reconstitution, but the amount, orientation, and composition of membrane proteins can hardly reach the level of native cell membranes. In fact, it is very difficult to go beyond the protein: lipid molar ratio of 1:5000 in dealing with integral membrane proteins possessing large (10 nm) extracellular domains [3]. A possible solution to these problems is to spread native cells on planar substrates. This approach was first demonstrated using human erythrocyte 'ghosts' (cells without cytoplasm) spread on 10 nm thick cellulose films [31]. This study investigates two types of membrane systems: sarcoplasmic reticulum membrane purified from rabbit muscle (**section 5.1**) and healthy and malaria-infected human erythrocyte ghost membranes (**section 5.2**).

In section 5.1, sarcoplasmic reticulum (SR) membranes from rabbit muscle were deposited on silicon substrates and characterized by the combination of spectral ellipsometry (SE), high-energy XRR, NR, and ATR-IR spectroscopy. ATR-FTIR measurements were performed under collaboration with Christian Busch in Prof. Dr. Reiner Dahint's group (PCI, Heidelberg University). *In vivo*, SR membranes form tubular networks around myofibrils. The main function of SR membranes is to store Ca^{2+} and maintain the cytosolic $[\text{Ca}^{2+}]$ level constant. Sarcoplasmic/endoplasmic reticulum Ca^{2+} -ATPase, called SERCA, is an active ion pump that pumps Ca^{2+} against a concentration gradient across the membrane. During the excitation of skeletal muscle, this gradient relaxes the elevated $[\text{Ca}^{2+}]$ (Figure 1.5). Previous reports showed that SR membranes can coat the surface of glass substrates with and without polymer coating [32]. SR membranes can also be deposited on the surface of 10 μm -large silica microparticles, sustaining the Ca^{2+} -dependent ATP hydrolysis function [33]. Following the optimization of the preparative conditions by SE, the detailed structures in the direction perpendicular to the membrane were probed by XRR. ATR-FTIR data showed

strong signals from amide I and amide II bands of the native SR membranes containing a large amount of Ca^{2+} -ATPase, which could not be achieved by the reconstitution in artificial lipid membranes. The ex-situ combination of XRR and ATR-FTIR enables the real-time monitoring of enzymatic digestion of Ca^{2+} -ATPase, suggesting the potential of the in situ combination of reflectivity and vibrational spectroscopy to unravel both structure and dynamics of complex biological membranes.

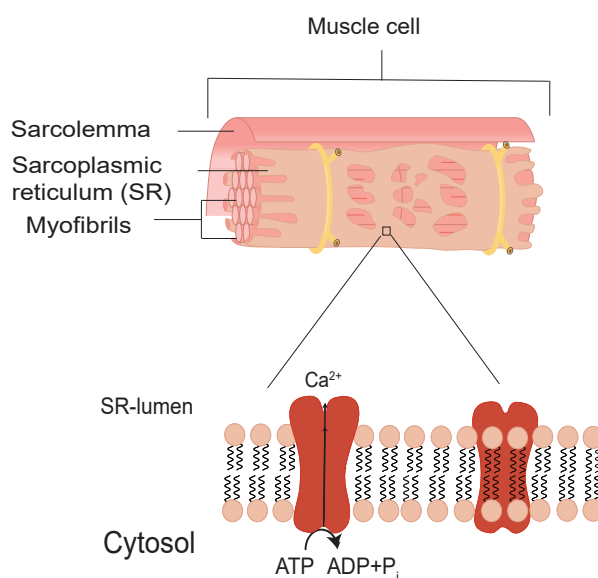


Figure 1.5: Illustration of SR membranes in vivo

In section 5.2, healthy (Figure 1.6a) and malaria-infected human erythrocyte ghost membranes were deposited onto silicon substrates coated with a 15 nm-thick cellulose film. The "ghost" membranes, membranes with no cytoplasm, were prepared by osmotic lysis and resealing (see section 3.1 for details). The structures perpendicular to the membrane surface were characterized by NR. Malaria-infected human erythrocytes were prepared by Prof. Dr. Michael Lanzer's group (CIID, Heidelberg University). One of the most lethal human malaria parasites, *Plasmodium falciparum*, is known to change the structure and function of the host cell while growing in erythrocytes. Infected erythrocytes acquire the capability to adhere to the surface of vascular endothelium, which enables them to escape from the clearance in the spleen [34]. As shown in Figure 1.6b, infected erythrocytes ex-

press a cluster of adhesion protein, called PfEMP1. These clusters, called protein “knobs,” are connected to the remodeled cytoskeletal networks and thus modulate the membrane structures, cytoplasmic molecular networks, mechanical properties, and adhesion function [35] [36] [37]. Previously, Tanaka et al. showed that erythrocyte “ghost” membranes can be spread on substrates coated with 10 nm-thick cellulose films [31]. Furthermore, they demonstrated that one can prepare micropatterns of native erythrocyte membranes by using lithographic patterning of cellulose supports [32]. In this study, healthy and infected ghost cells were prepared by osmotic lysis and resealing and deposited on cellulose films. The structures in the direction perpendicular to the membrane surface were characterized by NR in D₂O to maximize the contrast in scattering length density.

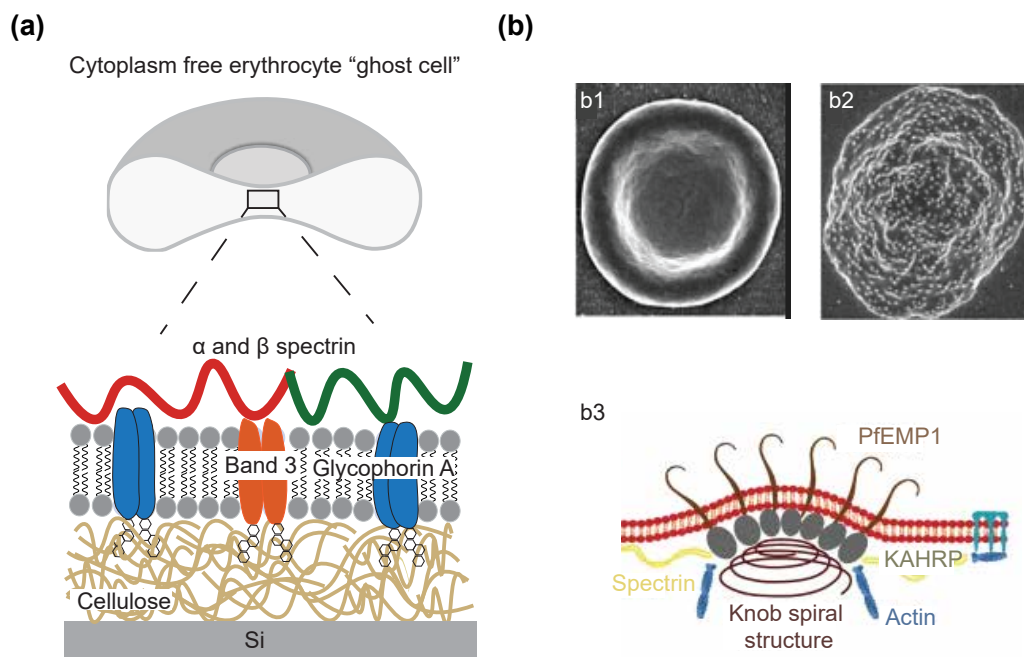


Figure 1.6: (a) Healthy erythrocyte "ghost cell" onto silicon substrates coated with cellulose film, (b) SEM images of b1, healthy erythrocyte and b2, infected erythrocyte [38]. b3 scheme of simplified membrane model showing knob structure of PfEMP1 [37].

2 Theory

2.1 Self-assembly of membranes

Amphiphilic compounds possess a water-attracting head and a water-repelling tail, which leads to their natural tendency to organize into bilayers or micelles when in water. This self-assembly process is primarily driven by the hydrophobic effect.

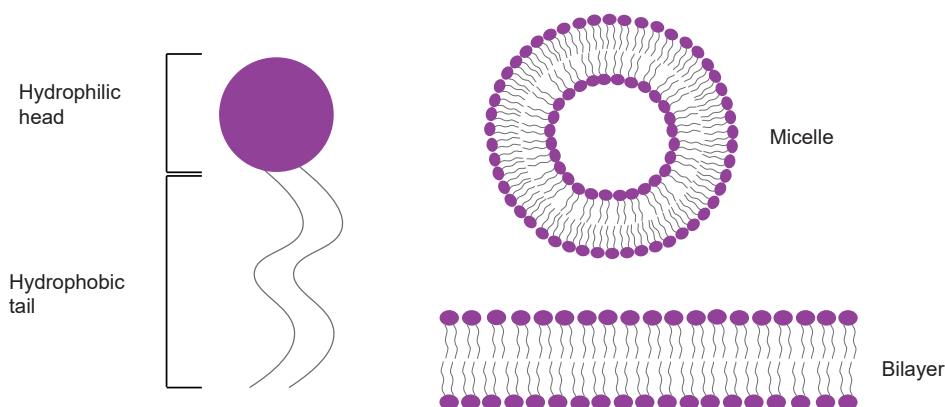


Figure 2.1: Structure of lipids.

This effect is primarily due to the structured hydrogen bonding network in water. The driving force behind this self-assembly is the desire to minimize disruption to the hydrogen bond network of water. From the thermodynamic point of view, this process can be explained through the change in Gibbs free energy ΔG is given by equation 1. The system seeks a lower energy state, forming ordered structures.

$$\Delta G = \Delta H - T\Delta S \quad (1)$$

Where ΔH represents the change in enthalpy, T the temperature and ΔS the change in entropy. When a lipid molecule is transferred into water, a more ordered structure of water molecules is formed around the hydrocarbon chain. This is known as the clathrate cage, the trapping of hydrophobic groups in a water cavity. Therefore, the entropy of transfer ΔS is always negative. The change in enthalpy is unfavorable; it can be either positive or negative [39] [40] [41]. In terms of the change in the Gibbs free energy, the change is

positive, here energy must be expended to introduce a lipid molecule into water (disruption of the hydrogen-bonding network of the water).

More specifically, the change in Gibbs free energy corresponds to the change in chemical potential that is needed for a lipid molecule to be transferred from a standard state $\mu_{HC,ref}$ (assuming that the hydrocarbon chain is in a pure hydrocarbon environment), into water. This can be described as the following

$$\mu_{HC,ref} - \mu_{HC,w} = RT \ln X_{HC,w}, \quad (2)$$

$X_{HC,w}$ represents the mole fraction of the lipids in water. The experimental determination of the difference in chemical potential can be achieved by analyzing the solubility of the hydrocarbon chain in water, as described by equation 2. According to research by McAuliffe et al., there is a direct correlation between the length of hydrocarbon chains and their solubility in water. Specifically, as the length of these polymer chains increases, their ability to dissolve in water decreases. Further, McAuliffe et al. reported that the energy required to attach another methyl group to the hydrocarbon chain was found to be $6 \times 10^{-12} J$, corresponding to the energy of 20% of that of a hydrogen bond [42] [43]. The addition of the methyl groups forces the water molecules to pack more closely to the hydrocarbon chains. Following the Gibbs phase rule, a lipid in water and a lipid in a bilayer can only be in equilibrium at a fixed value of $X_{HC,w}$, which is known as the critical aggregate concentration. By rearranging the equation 2 to a logarithmic expression, one can obtain,

$$X_{HC,w}^* = X_{HC,bilayer} e^{\left(\frac{\Delta\mu}{kT}\right)} \quad (3)$$

The critical aggregate value for a single-chain lipid, Iyso-DPPC, is about 10^{-4} M, while for the double-chain lipid, DPPC, it is 10^{-12} M. These values show that only low concentrations of lipids are required to initiate spontaneous lipid micelle formation [44].

2.2 Polymerbrushes

Polymer brushes consist of long macromolecules that covalently bond to a surface by one chain end. If the density is sufficiently high enough, the polymer extends outward. a surface by one chain end. If the density is sufficiently high enough, the polymer extends outward. They are sensitive to changes in temperature, pH, and the type of solvent used. Due to these properties, they can be utilized to study adhesion and friction, control fluid flow, and regulate drug release. Polymer brushes are used in surface modification in the medical field, membrane studies, and future water purification systems [45].

There are two main approaches for synthesizing polymers on a solid substrate: the "grafting from" method and the "grafting to" method. For the "grafting from" approach, the polymer is directly grown from the substrate using living chain growth polymerization. For this purpose, an initiator is immobilized onto the surface of a substrate and then polymerized to the target numbers of monomers from the initiator. In this study, the "grafting to" approach was applied. For this purpose, the polymer is pre-synthesized with a narrow molecular weight distribution and attached to a functional group on the designated surface binding sites. With this method, the degree of polymerization can be determined prior to the grafting process [46].

In order to simplify the analysis, one may begin by considering a single-chain polymer modeled as a random coil under the "freely joint chains" assumption. In this model, only the chain connection to the monomer with no directional limitation on the angles is considered [47]. By assuming that a chain is made of N monomers with b being the monomer length, the end-to-end vector \vec{L} of a coil size is described as [47]

$$\vec{L} = \sum_{i=1}^N \vec{b}_i. \quad (4)$$

By taking the means square of the end-to-end distance, expanding the sum, and selecting N cases where $i = j$ the following equation is obtained

$$\langle L^2 \rangle = Nb^2 + \left\langle \sum_{i \neq j} b_i b_j \right\rangle. \quad (5)$$

Considering the free random walk (random end-to-end oriented vectors), where there is no relationship between links N , the cross terms disappear (their sum approaches zero), leading to the following equation

$$\langle L^2 \rangle = Nb^2. \quad (6)$$

Considering the Boltzmann principle, to calculate the entropy and enthalpy of the free joint chains, the distribution function $P(L)$, where L is the end-to-end distance, is applied. This can be expressed as a Gaussian function [48]

$$P(L) = \left[\frac{3}{2\pi \langle L^2 \rangle} \right]^{\frac{3}{2}} \exp \left[-\frac{3}{2} \frac{L^2}{\langle L^2 \rangle} \right]. \quad (7)$$

The entropy $S(L)$ can be extracted from the Boltzmann equation

$$S(L) = \frac{3k_B L^2}{2 \langle L^2 \rangle}. \quad (8)$$

As the chain stretches, the entropy $S(L)$ decreases, and this leads to an increase in the Gibbs free energy $G(L)$

$$G(L) = G(0) + \frac{3}{2} \frac{k_B T}{\langle L^2 \rangle} L^2. \quad (9)$$

With this assumption, it can be said that the polymer chain is constrained to be in a harmonic potential with the following spring constant K

$$K = \frac{3k_B T}{\langle L^2 \rangle}. \quad (10)$$

With increasing temperature, the strength of the spring increases, also known as the entropic spring. Here, it must be considered that, in reality, a polymer chain cannot rotate freely; it requires finite bond angles [49] [50] [51]. This constraint on the rotation leads to an increase in the length of the segment with the use of a geometric factor C_g . Thus, the Kuhn's law is given as [52]

$$\langle L^2 \rangle = C_g N' b^2 = N' \lambda^2, \quad (11)$$

2 THEORY

where Kuhn length λ is given as [52]

$$\lambda = b\sqrt{C_g}. \quad (12)$$

For real polymer chains, the free joint chain model is modified by the segment length (λ) and the unit number N' . In terms of the volume uptake of two monomers, they cannot occupy the same space, which can be described by the Flory finite exclusion model. This finite excluded volume arises from considering the repulsion between the i th and j th spheres, similar to a Van der Waals gas.

$$w_{ij} = \nu k_B T \delta(r_j - r_i) \quad (13)$$

Here ν represents the empirical parameter of the excluded volume given in the units of m^3 and $\delta(r_j - r_i)$ the Dirac's delta function for hard spheres. The monomer concentration for a fixed volume R^3 and N monomers is given as $c_m = N/R^3$. The repulsion energy density is given in the units per volume as

$$w_{ij} = \nu k_B T P = \nu k_B T c_m^2. \quad (14)$$

Considering the probability of two monomers collision $P = c_m^2$. The repulsion of the inner energy ΔU_{rep} , by taking into account that the polymer volume remains R^3 is shown as

$$\Delta U_{rep} = R^3 w_{ij} = \frac{\nu k_B T N^2}{R^3}. \quad (15)$$

The elastic energy

$$\Delta G_{ela} = \frac{3 k_B T}{2 \langle L^2 \rangle} L^2 = \frac{3 k_B T}{2 N b^2} R^2. \quad (16)$$

This represents the counterbalance to the repulsive interaction leading to the total free energy

$$\Delta G_{total} = \Delta U_{rep} + \Delta G_{ela}. \quad (17)$$

By minimizing the total free energy $d\Delta G_{total}/dR = 0$, the mean radius of polymer $\langle R \rangle$

also known as the Flory radius R_F is written as [53]

$$\langle R \rangle = (b^2\nu)^{\frac{1}{5}} N^{\frac{3}{5}}. \quad (18)$$

It has to be noted that equation 18 is only valid for chains in bulk. For the case of polymer chains in two dimensions, the following is given as $\langle R \rangle \propto N^{\frac{3}{d+2}}$ in dimensions D [49] [53]. Since it is difficult to experimentally determine the average end-to-end distance $\langle L \rangle$, the radius of gyration R_g is applied to describe the dimensions of a polymer chain. It is defined as the average distance of the monomer to the center of gravity of the chain segment

$$R_g^2 = \frac{1}{N} \left\langle \sum_{k=1}^N (r_k - r_{av})^2 \right\rangle. \quad (19)$$

In the presence of polymer chains undergoing 3-dimensional random walk, the equation is simplified to

$$R_g = \frac{1}{\sqrt{6}} \langle L \rangle. \quad (20)$$

Specifically, the radius of gyration is influenced by the size of the polymer chain, the number of polymer chains, and the solvent in which it is placed [51] [54].

Depending on the choice of solvent, the polymer chain swells in a good solvent (high affinity towards the polymer chain) or shrinks in a poor solvent (low affinity toward the chain). Depending on the size of the polymer chains (R_g) and the average distance between the grafting sites (d), polymer chains grafted to the surface can have distinct conformations.

They can be divided into three conformations: the (a) pancake, (b) mushroom, and (c) brush conformations (indicated in Figure 2.2). In the case of the pancake and mushroom conformations, the distance d is more significant than R_g . When it comes to pancake formation, the polymer chains are more strongly attracted to the surface. In contrast, for mushroom formation, if there isn't any interaction between the polymer chains, they will stay coiled in a compact shape. If, on the other hand, $d < R_g$, the polymer chains start to interact with each other, and a repulsive interaction between the surface of the substrate and

the polymer occurs. This results in the formation of tethered brushes known as polymer brushes [55] [56] [57] [58].

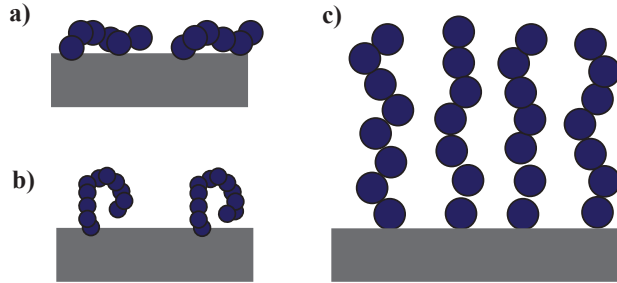


Figure 2.2: Graphical representation of different grafting regimes, (a) Pancake, (b) Mushroom and (c) Polymer brush.

2.3 Fundamentals on GaN-based HEMTs

Due to its unique properties, Gallium Nitride (GaN) has attracted considerable interest as a semiconductor material. With a bandgap of approximately 3.4 eV at room temperature, GaN finds applications in optoelectronics, e.g., blue and UV LEDs and laser diodes [59]. The crystalline structure provides high electron mobility and breakdown field strength and allows operation at high temperatures (thermal conductivity). This makes it suitable for use in high-frequency devices. To optimize the application performance of GaN, it is essential to understand the crystalline structure/arrangement of GaN and the associated defect dynamics.[60] [61].

2.3.1 Crystallographic structure

Gallium Nitride (GaN) is a III-Nitride semiconductor that crystallizes in two primary structures: the zinc blende structure, also referred to as the cubic phase, and the wurtzite structure. Since GaN/AlGaN HEMTs are grown on wurtzite, only this structure is discussed in this thesis. The wurtzite crystal structure is a hexagonal close-packed lattice (HCP). This crystal structure influences the electrical, optical, and mechanical properties of this compound.

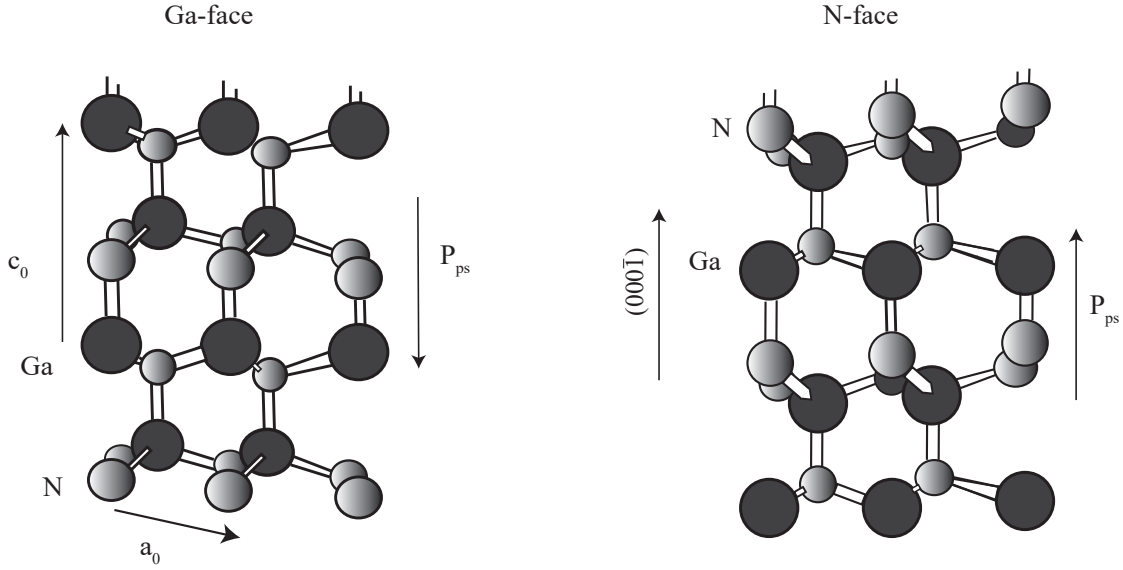


Figure 2.3: Crystal structure of GaN adapted from ref. [62]

In GaN, each Gallium (Ga) atom is tetrahedrally coordinated with four nitrogen (N) atoms, forming Ga-N covalent bonds, while three Ga atoms surround each N atom [59] [63]. The atoms are mainly covalently bonded, but there are also ionic contributions due to the different electronegativity [64]. This arrangement results in the alternating layers of Ga and N atoms stacked along the c -axis, with hexagonal symmetry in the basal plane. The wurtzite lattice is characterized by three key parameters: a_0 which represents the edge length of the hexagon; c_0 the height of the hexagonal lattice cell, and the ratio of the bonding length between nitrogen and Gallium, along the c -direction in units of c_0 . For an ideal wurtzite crystal the c_0/a_0 ratio is 1.633 and the value for u_0 is 0.375. The degree of non-ideality is an important measure of the polarization strength of III-nitrides and is given in table 1 for AlN and GaN.

Table 1: Lattice constants, spontaneous polarization of GaN and AlN [65]

Wurtzite	GaN	AlN
a_0 [Å]	3.189	3.112
c_0 [Å]	5.185	4.982
c_0/a_0	1.633	1.619
P_{sp} [C/m ²]	-0.081	-0.029

The GaN crystal structure can be grown in two directions, the Ga-face or N-face along

the c -axis, which determines the direction of spontaneous polarization. The spontaneous polarization, short P_{sp} depends both on the asymmetry of the structure in the c -axis and the ratio of c_0/a_0 . This polarization creates a dipole moment along the c -axis, which influences the behavior of charge carriers and optical transitions in GaN-based devices. From GaN to AlN, the spontaneous polarization increases (c_0 increases and c_0/a_0 decreases). The spontaneous polarization for $\text{Al}_x\text{Ga}_{1-x}\text{N}$ layer is given as [65]

$$P_{SP}(x) = (-0.052x - 0.029)C/m^2, \quad (21)$$

where x represents the aluminum mole fraction in the material. The AlGaN barrier layer is grown pseudomorphically on top of the GaN layer. In addition to the spontaneous polarization, piezoelectrical polarization is also present. The lattice mismatch between GaN and AlGaN in GaN-based HEMT structures causes the AlGaN layer to experience tensile strain. This leads to the generation of piezoelectric polarization P_{PE} due to the piezoelectric properties of AlGaN and is expressed as

$$P_{PE}(x) = 2\frac{a - a_0}{a_0} \left(e_{31} - e_{33} \frac{C_{13}}{C_{33}} \right), \quad (22)$$

where a is the lattice constant of the deposited and stretched or strained material, e_{33} and e_{31} are the piezoelectric constants, C_{13} , C_{33} are the elastic constants. The total polarization P is the sum of spontaneous polarization P_{SP} and piezoelectric polarization P_{PE}

$$P(x) = P_{SP}(x) + P_{PE}(x). \quad (23)$$

The polarization sheet charge density σ at the interface of a GaN/ $\text{Al}_x\text{Ga}_{1-x}\text{N}$ is defined as

$$\sigma(x) = P(x) + P_{SP,GAN}. \quad (24)$$

In a Ga-face structure with AlGaN as the barrier layer and GaN as the buffer layer, the polarization-induced sheet charge density at the interface is positive ($+\sigma$). The band gap difference between AlGaN and GaN forms a band discontinuity at the material interface. In order to compensate for the polarization-induced charges at the lower interface of

GaN/AlGaN, the charge carrier will flow to and accumulate at the interface, by band bending, forming the two-dimensional electron gas (2DEG), which is confined in a triangular quantum well with a sheet carrier concentration n_s . The formation of a 2DEG leads to a drop below the Fermi level E_F . In an N-face GaN/AlGaN structure, the spontaneous and piezoelectric polarizations are opposite, resulting in a negative polarization of the sheet charge density ($-\sigma$) at the upper GaN/AlGaN interface.

The sheet carrier concentration n_s in the 2DEG can be influenced by the design of the $\text{Al}_x\text{Ga}_{1-x}\text{N}$ layer, including the thickness d , aluminum mole fraction x , and the temperature T . Increasing Al_x and thickness d of the layer increases the carrier concentration n_s . For the temperatures, an inverse behavior is observed, where the temperature exponentially decreases until $T < 100$ K [66] [65].

2.3.2 Space charge regions of Semiconductors-Electrolytes

The electron affinity χ_e is a physical measure of the energy required to move an electron from the surface of the semiconductor into the vacuum outside the surface. For metals, the electron affinity χ_m equals the work function ϕ_m and is an intrinsic property of the metal. The electron affinity of a semiconductor varies depending on the band structure at its surface [67][68]. This is shown by

$$\chi_e = \phi_W - \phi_{BB} - (E_C - E_F), \quad (25)$$

where ϕ_W represents the work function, ϕ_{BB} the band bending, E_C the conduction band, and E_F the fermi energy level. ϕ_W describes the difference in energy between the Fermi level E_F , defined as the highest energy state occupied by electrons in a material, and the level of the vacuum. When a semiconductor is brought into contact with another phase (e.g., liquid, gas, metal), electrical charges are redistributed, and a double layer is formed. This redistribution results from the difference in work functions or Fermi levels, leading to band bending and the creation of a space charge region [68]. Changes in the surface charge, including ion accumulation, pH variations, and molecular dipoles, directly affect the formation of the space charge region. At the same time, the sensitivity to these influences

is given by the semiconductor electron affinity [69]. In addition, the space charge region is further affected by employing an external bias potential (U_{bias}). Suppose the system (semiconductor - electrolyte or metal) is assumed to be in thermodynamic equilibrium. In that case, no electron transfer will occur across the interface, and the Fermi levels of these two materials will be the same; no band bending is taking place (flat-band potential U_{fb}).

Three scenarios can take place at the interface between a n-type semiconductor and the electrolyte when a positive or negative Voltage is applied: By applying a negative voltage ($V < 0$), charges are adsorbed on the surface of the semiconductor, resulting in a downward band bending of the conduction band and valence band by forming an accumulation layer. Applying a positive voltage ($V > 0$) depletes most carriers near the surface. The semiconductor's valence band rises above the Fermi level as the voltage increases. As a result, holes dominate as the majority carriers at the surface, while electrons dominate as the majority carriers in the bulk, also known as the inverted regime. The opposite response occurs at the interface for a p-type semiconductor [68] [70] [71] [72].

2.3.3 Current-Voltage (I-V) Characteristic of transistors

Electrochemical biosensors designed to detect biomolecules have attracted considerable attention in recent years. They effectively convert chemical reactions at the surface into measurable changes in electrical properties. Among the variety of biosensors available, field-effect transistors have gained considerable interest in medical and environmental applications.

High electron mobility transistors (HEMTs) are particularly promising in this area [73]. This semiconductor allows electrons to move more freely. It is more stable to degradation or shift in electrical response than conventional silicon-based transistors, resulting in faster switching speeds and better high-frequency performance. The heterostructure design, consisting of different layers of semiconducting materials and band gaps, allows the formation of a two-dimensional electron gas (2DEG) at the hetero-interface of two semiconductor layers, particularly in this study for AlGaIn/GaN. To obtain the current-voltage curves, a bias/gate potential V_G is applied to the gate of the transistor. In this way,

the number of electrons in the 2DEG, the carrier mobility, and the system's conductivity are modulated [70] [65] [73].

This information is obtained by recording the output and transfer curves. The output curves are the result of the measurement of the drain current (I_{DS}) against the voltage applied between the drain and source contacts (V_{DS}) at a given range of V_G values. The transfer curves are obtained by measuring I_{DS} versus the applied gate voltage (V_G) at a given range drain-to-source potentials (V_{DS}). The transfer curves are used to identify the linear region of the system. From the slope of the measured transfer curve, the transconductance g_m can be determined. Transconductance, often referred to as transistor gain, quantifies the sensitivity of the drain current to changes in the gate voltage [68]. For an n-type AlGaIn, the transconductance can be given as the following [74]

$$g_m = \frac{\partial I}{\partial V} = \mu C_s \frac{W}{L} (V_G - V_{th}), \quad (26)$$

where μ indicates the mobility of the charge carriers, C_s the capacity per unit area of the gate, W and L the width and the length of the channel, V_G the gate voltage, and V_{th} the threshold voltage. The threshold voltage V_{th} is obtained by extrapolation of the linear regression I_{DS} [74] [73].

2.4 High-Energy specular X-ray and Neutron reflectivity

X-ray and neutron reflectivity are surface-sensitive techniques used to measure the near-surface structures of thin films and multilayered systems. It measures the reflected intensity of a monochromatic X-ray or neutron beam as a function of the angle of incidence and provides information on the surface and interface roughness, density, and thickness of the sample [75].

X-rays are subject to refraction and reflection when they come into contact with interfaces of different electron densities. This typically occurs when they pass between a gas or vacuum interface and a solid or liquid material boundary. The refractive index n of a matter

2 THEORY

in the X-ray region is given by [75][56]

$$n = 1 - \delta + i\beta, \quad (27)$$

where δ represents the real part of the refractive index, which is associated with the material's electron density, and β represents the imaginary part of the refractive index, which accounts for the absorption of X-rays by the material. The real part of the refractive index is related to ρ_e , the electron density, the classical electron radius $r_e = 2.818 \times 10^{-15}$, and the wavelength λ as for the real part of the refractive index

$$\delta = \frac{\lambda^2}{2\pi} r_e \rho_e = \frac{\lambda^2}{2\pi} SLD, \quad (28)$$

δ is in the typical range of 10^{-5} to 10^{-6} and can be expressed in terms of SLD.

The imaginary part β lies in the order of 10^{-8} and is related to the attenuation coefficient $1/\mu$.

$$\beta = \frac{\mu\lambda}{4\pi} \quad (29)$$

In the case of neutrons, the refractive index n , the real part δ and the imaginary part β are given as

$$\delta = \frac{\mu\lambda}{4\pi} Nb, \quad \beta = \frac{\mu\lambda}{4\pi}. \quad (30)$$

Here, the variable N represents the atomic density and b the coherent scattering. The absorption coefficient is μ [76].

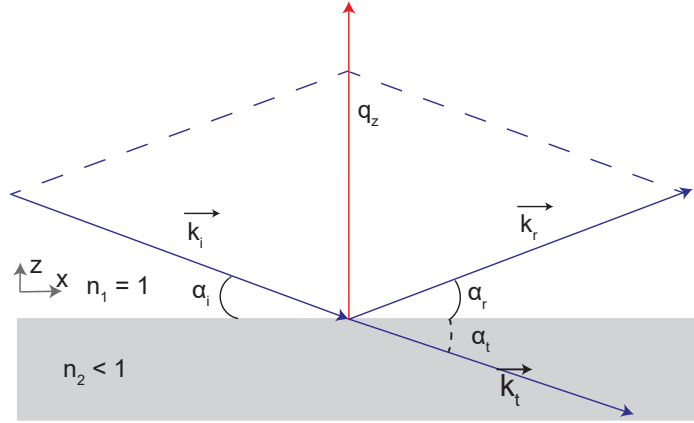


Figure 2.4: Graphic representation of reflection and refraction of an incident beam on a smooth surface.

According to Snell's law, assuming a smooth interface between two media with the refractive indices of n_1 and n_2 , (see Figure 2.4), an incident beam under the angle α_i can be reflected from the interface of medium 1 with an angle $\alpha_i = \alpha_r$ and can be refracted in medium 2 with an angle of α_t .

As the index of refraction in the X-ray region is less than one for any material, X-rays from air or vacuum entering a solid or liquid will be refracted away from the normal to the surface. To describe this relationship, Snell's law is used [75]

$$n_1 \cdot \cos \alpha_i = n_2 \cdot \cos \alpha_t. \quad (31)$$

For incident angles below the critical angle α_c , the phenomenon of total internal reflection takes place, where the X-rays do not penetrate into the medium and are reflected ($n_1 < n_2$)

$$\alpha_c \approx \sqrt{2\delta}. \quad (32)$$

For the interface between vacuum and silicon, the critical angle α_c is in the range of $\alpha_c = 0.22^\circ$ at $\lambda = 1.54 \text{ \AA}$ [56]. For incident angles exceeding α_c , the X-ray beam undergoes both reflection and refraction, resulting in an exponential attenuation of the reflected intensity R . The reflectivity is given as the function of the momentum transfer q_z in the z -direction

$$q_z = \frac{4\pi}{\lambda} \sin\alpha_i. \quad (33)$$

2.4.1 Fresnel reflectivity of a flat surface

The Fresnel equations describe the reflection (r) and transmission (t) of an incident ray (i) on an ideal smooth surface [77]. The reflection coefficient is given by Snell's law and Maxwell's equations for electromagnetic wave propagation in matter, given by

$$r(\alpha_i) = \frac{\sin\alpha_i - \sqrt{n^2 \cos^2\alpha_i}}{\sin\alpha_i + \sqrt{n^2 \cos^2\alpha_i}}. \quad (34)$$

In case of a small incident angle α_i with no absorption, the equation 34 can be written as

$$r(\alpha_i) = \frac{\alpha_i - \sqrt{\alpha_i^2 - \alpha_c^2}}{\alpha_i + \sqrt{\alpha_i^2 - \alpha_c^2}}. \quad (35)$$

Here, the reflectivity R is equal to the square of the reflection coefficient. Taking into account the absorption of the X-ray beam by the material, the Fresnel reflectivity is expressed as

$$R(\alpha_i) = rr^* = \left| \frac{\alpha_i - \sqrt{\alpha_i^2 - \alpha_c^2 - 2i\beta}}{\alpha_i + \sqrt{\alpha_i^2 - \alpha_c^2 - 2i\beta}} \right|^2 = \left| \frac{q_z - \sqrt{q_z^2 - q_c^2 - \frac{32i\Pi^2\beta}{\lambda^2}}}{q_z + \sqrt{q_z^2 - q_c^2 - \frac{32i\Pi^2\beta}{\lambda^2}}} \right|^2. \quad (36)$$

Equation 36 can be simplified if the momentum transfer q_z is significantly larger than q_c , the Fresnel reflectivity R_F can be given as

$$R_F(q_z) = \frac{q_c^4}{16q_z^4}. \quad (37)$$

The reflectivity curve can be divided into three different regions [75] [78]:

- 1) The plateau region where total external reflection $R_F(q_z) = 1$ occurs, for $q < q_c$ is given.
- 2) Followed by a sharp decrease with angle increments, for $q = q_c$.
- 3) Decrease of the reflectivity according to the power law by $1/q_z^4$, for $q_z > 3q_c$.

2.4.2 Reflection from a layered sample

The shape of the reflectance curve provides valuable qualitative information about the sample's thickness, electron density, and interfacial roughness. The thickness of the film can be determined by the observation of distinct minima, known as Kiessing fringes, which appear as the film thickness increases [56].

These fringes are caused by constructive and destructive interference between reflected rays at the interfaces. As a result, the distance between these minima is directly proportional to the film thickness d .

$$d = \frac{2\pi}{\Delta q_z} \quad (38)$$

The most negligible thickness detectable by X-ray reflectivity is influenced by the maximum q_z , which can be affected by beam flux and focus. In addition, the electron density difference between the film and the substrate is related to the amplitude of the fringes. Information about the smoothness or roughness of the interface between the layers can be obtained from the shape of the reflectivity curve. As the intensity decreases, the fringes become broader and less defined. According to Born's approximation [56], the reflectivity of a rough surface, assuming that the intensity of the incident beam remains constant, is adjusted as follows

$$R(q_z) = R^F(q_z) \cdot e^{-q_z^2 \sigma^2}, \quad (39)$$

σ represents the surface's root mean square (RMS) roughness; according to the equation, the surface roughness (σ) increases, which causes the exponential term of the X-ray reflectivity intensity to decrease more rapidly. In other words, rougher surfaces lead to a faster decrease in the reflected intensity as the scattering vector magnitude q_z increases [75][78]. In order to fit the reflectivity data, the Parratt software is used [79]. This software allows the definition of individual layers. These are characterized by a specific thickness d , SLD, roughness (σ). The smooth transition between the layers is modelled by considering the changes in these parameters across the interfaces [79].

2.5 Grazing incidence X-ray fluorescence (GIXF)

Grazing Incidence X-ray fluorescence (GIXF) analyzes materials' elemental composition and depth distribution, specifically thin films or surfaces. When the incident X-rays interact with the atoms in the sample, they can excite the electrons in the inner shell and cause them to be ejected from the atom. This causes electrons with higher energy levels to fill the vacancies by emitting characteristic X-ray fluorescence radiation. By variation of the X-ray beam's incidence angle, GIXF can probe different depths within the sample. At very small angles of incidence (below the critical angle), the X-rays penetrate only a few nanometers into the sample, providing information about the near-surface region. As the angle of incidence increases (remaining below the critical angle for total reflection), the penetration depth of the probe increases, enabling depth profiling of the material's elemental composition and structure [80][81]. The angle of incidence influences the depth to which the evanescent field penetrates at grazing incidence. This relationship is described by Snell's law (see eq.31), which explains how the angle of refraction corresponds to a given angle of incidence [28]

$$\Lambda(\alpha_i) = \frac{\lambda}{\sqrt{8\pi}} \left[\sqrt{(\alpha_i^2 - \alpha_c^2) + 4\beta^2} - (\alpha_i^2 - \alpha_c^2) \right]^{-1/2}, \quad (40)$$

with $\Lambda(\alpha_i)$ being the penetration depth, β the imaginary part of the refractive index $n = 1 - \delta + i\beta$.

The fluorescence intensity $I_i^f(\alpha)$ of an element i at a distance z from the air-water interface at an angle of incidence α can be written in terms of

$$I_i^f(\alpha) = S \int_0^\infty I^{ill}(z, \alpha) c_i(z) \exp(-z/L_i) dz. \quad (41)$$

After the normalization of the sample's fluorescence signal by the blank buffer signal, S , the proportional constant is scaled out. Further, $c(z)$ represents the concentration of the element i at a depth z . The attenuation of the fluorescence emission between position z and the detector is represented by the exponential term, where L_i indicates the attenuation length of water at the specific fluorescence line, e.g. $L_{Cd-L\alpha} = 57.72 \mu\text{m}$ and $L_{Ca-K\alpha} = 93.71$

μm .

By the use of a slab model, the illumination profile $I^{ill}(z, \alpha)$ can be obtained by the matrix propagation technique. By detailed XRR data analysis, using a slab model, the thickness and electron scattering densities of every layer of the system can be obtained [29]. An asymmetric Gaussian profile can be used to reconstruct the concentration profile of ion species condensed at the head group of a lipid monolayer

$$c_i(z) = c_0 + c_{max} \frac{\sqrt{e}(z - z_{HC})}{z_{max}} \exp\left(-\frac{(z - z_{HC})^2}{2z_{max}^2}\right), \quad (42)$$

c_0 represents the bulk concentration, while z_{HC} represents the alkyl chain and lipid head-group interface [28][27]. The analysis also provides the concentration maximum c_{max} and the corresponding z-position of the maximum, z_{max} . The Levenberg-Marquardt non-linear least squares optimization [82] was used to improve the model.

2.6 Atomic Force Microscopy (AFM)

Atomic Force Microscopy (AFM) characterises the surface topography and properties of conductive and non-conductive materials. As it scans, it generates images based on measuring the intermolecular forces between a sharp tip and the sample's surface. This technique can be used to probe material in a vacuum, air, or liquid environment with nanoscale resolution [83]. To probe a surface, a sharp tip that is attached to a cantilever acts as a spring for measurement. The cantilever interacts with the sample surface. A piezoelectric scanner moves the cantilever in the z-direction to allow oscillation of the cantilever while maintaining a set distance. The substrate is then moved in the XY-direction under the cantilever by an additional piezo motor. The interactions between the sample surface and the tip are controlled by a laser beam focused on the back of the cantilever and directed to a position-sensitive quadrant photodiode with short PSPD. In the last step, a position-sensitive detector receives the reflected light from the surface of the cantilever. The cantilever deflection is calculated from the local displacement of the reflected laser spot on the detector.

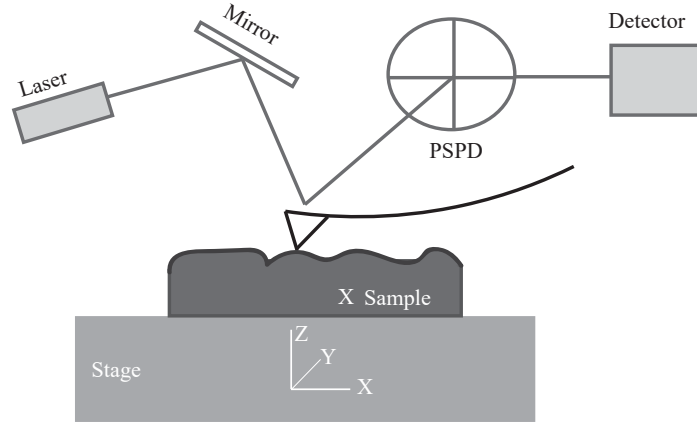


Figure 2.5: Schematic illustration of the AFM setup.

Force maps are generated to investigate mechanical properties, including stiffness, adhesion, and rupture force. The deflection of the cantilever is measured in relation to the vertical movement of the sample as the tip approaches and retracts from it. A raw curve is obtained, plotting the photodiode voltage as a function of the z -scanner position. Using corrections, a Force vs. Separation Distance curve is obtained, plotting the force experienced by the probe as a function of the probe-sample separation distance.

To image the topography of a material, the measured deflection of the cantilever as the tip scans the sample surface is used to create a topographic map of the surface with nanometer resolution. The variations in deflection correspond to the height variations of the sample surface, allowing for detailed mapping of surface features. The Root Mean Square (RMS) roughness is a commonly used measure to characterize the topography of a surface in terms of its roughness. It represents the average deviation of the surface height from the mean value.

$$RMS = \sqrt{\frac{\sum_i (z_i - \bar{z})^2}{N}} \quad (43)$$

Where z_i is the height of the sampling point, \bar{z} is the mean height, and N is the number of data points [84] [85].

AFM can operate in contact mode, tapping mode, and non-contact mode. In contact mode,

when the tip gets closer to the surface, the attractive forces result in the bending of the cantilever. As the distance decreases, the force becomes repulsive. During the scanning process, the tip remains in constant contact with the sample surface, and adjustments are continuously made to maintain this contact. The surface profile is obtained from the deformation of the cantilever tip with the substrate.

In the non-contact mode, the cantilever oscillates very close to the sample at a distance of a few nanometers during the scanning process. The tip-sample interaction forces modify the phase, resonance frequency, and oscillation amplitude. These variations in oscillation compared to the external driving reference oscillation provide information about the surface properties of the sample. Images are generated using van der Waals, electrostatic, or magnetic forces. The advantages of this mode are that the sharpness of the tip is maintained, and the measured substrate is not damaged.

In the tapping mode, also known as the intermittent contact mode, the tip oscillates close to its resonant frequency by periodically tapping the sample's surface. This method results in a more significant deflection signal and allows easier control of the loop [84] [85].

2.7 Ellipsometry

Ellipsometry is a spectroscopic, non-contact, non-invasive measurement technique used to obtain information such as film thickness, surface roughness, interfaces, and optical properties from thin films and multi-layered materials in the range of a few Angstroms. This technique measures and analyzes the change in linear polarized light as it is reflected or transmitted through a thin material surface represented by Δ and ψ . Here, Δ represents the relative phase change and ψ the relative amplitude p- and s- polarized light waves.

Most instruments consist of a light source, a polarizer, a compensator, an analyzer, and a detector. A monochromatic light linearly polarized by the polarizer is passed into the compensator, which introduces a controlled phase shift between the perpendicular and parallel components of the incident light's polarization. This light beam is directed onto the sample's surface at a defined angle of incidence. When the light interacts with the

sample, it undergoes various optical transformations (changes in the polarization state) depending on the properties of the sample, such as thickness d , refractive index n , and roughness σ . From the measurement, the change in p and s components, amplitude, and phase change are detected and expressed as follows

$$\rho = \frac{R_p}{R_s} = \tan(\psi) e^{i\Delta}, \quad (44)$$

where $\tan \psi$ represents the amplitude ratio during reflection, ρ is the complex reflectance ratio, and $\frac{R_p}{R_s}$ denotes the Fresnel reflection coefficient [86]. Ellipsometry does not provide direct information about the thickness d or refractive index n of the sample. Instead, it provides information on the ratio of the complex reflection coefficients for p-polarised and s-polarised light, known as ellipsometric parameters. These parameters can be used to determine sample thickness and optical constants by comparison with theoretical models or reference measurements [86][87].

2.8 Contact Angle

Contact angle measurement is a quantitative method of assessing the wettability of a substrate by determining the equilibrium angle at the intersection of the solid/liquid and liquid/vapor interfaces (see Fig.2.6).

When a droplet contacts a solid surface, three phases interact: solid, liquid, and vapor. Molecules at phase boundaries experience unbalanced forces compared to the bulk, leading to changes in coordination numbers and the formation of surface tension. The Interfacial energy (γ) is defined as the change in free energy per unit area when a new interface is formed [88]

$$\gamma_i = \left(\frac{\partial G}{\partial A} \right)_{P,T,n}, \quad (45)$$

where γ is the interfacial energy, G the change of the total surface free energy per surface area (A), pressure (P) and at constant temperature (T).

At equilibrium state, the Gibbs free energy G is minimized with respect to surface area A ,

2.8 Contact Angle

leading to

$$dG = \sum_i \gamma_i dA_i = 0. \quad (46)$$

The surface area change due to droplet placement is described as follows [89]

$$dA_{SL} = dA_{SV} = \cos(\theta) dA_{LV}. \quad (47)$$

The following is given for the Gibbs free energy

$$dG = (\gamma_{SV} - (\gamma_{SL} + \gamma_{LV} \cos(\theta))) dA_{SL}. \quad (48)$$

In the state of thermodynamic equilibrium between the three phases, the contact angle [89] [90] is solely determined by the interfacial energies as expressed in the young equation

$$\gamma_{SV} = \gamma_{SL} + \gamma_{LV} \cos(\theta), \quad (49)$$

where γ_{LV} , γ_{SV} and γ_{SL} are the liquid-vapour, solid-vapour and solid-liquid interfacial tensions respectively, and θ is the equilibrium contact angle [91][92].

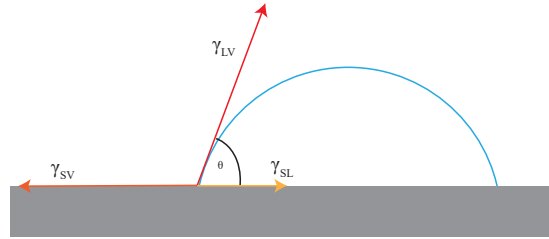


Figure 2.6: Illustration of a droplet on a solid surface showing the Solid-Liquid (SL), Solid-Vapor (SV), and Liquid-Vapor (LV) interfaces.

From the measured contact angle, the wettability of the surface can be determined. If the contact angle on the surface is less than 10° , the surface is hydrophilic, while if the contact angle is more significant than 90° , the surface is considered hydrophobic. The surface is considered superhydrophobic if the contact angle is more significant than 90° and up to 150° [93].

3 Materials and Methods

3.1 Materials

3.1.1 Chemicals

Tris(hydroxymethyl)aminomethane was purchased from Carl Roth GmbH (Karlsruhe, Germany). 1,2-dioleoyl-sn-glycero-3-phosphocholine (DOPC) was purchased from Avanti Polar Lipids (Alabaster, AL, USA). Texas red 1,2 dihexadecanoyl-sn-glycerol-3-phosphoethanolamine triethylammonium salt (Texas Red-DHPE) from AAT Bioquest, Germany. N-octadecyltrimethoxysilane (ODTMS) was purchased from Abcr (Karlsruhe, Germany). Unless otherwise stated, all chemicals were purchased from Merck KGaA (Darmstadt, Germany) and used without purification. In all experiments, Ultrapure water (Millipore, Molsheim, France) with a resistivity of 18.2 M Ω cm was used.

3.1.2 Substrates and Sample preparation

HEMT substrates

High electron mobility transistors (HEMT) substrates composed of GaN/AlGaN/GaN, with Al_{0.25}, GaN_{0.75}, and N (20 nm) heterostructures were grown on Si (111) substrates by metal-organic chemical vapor deposition (MOCVD). The substrates were gifts from Fujitsu Ltd. (Kawasaki, Japan) and were further treated by Prof. Dr. Eickhoff (Bremen, Germany).

Silicon substrates

Single-sided polished native oxide Silicon [100] wafers were used for X-ray reflectivity (XRR) and spectroscopic ellipsometer (SE) measurements and were purchased from Si-Mat (Ladensberg, Germany). The wafers were cut into 24.5 × 13 mm rectangular pieces for XRR measurements. Further Silicon blocks [111] with native oxide coating (80 × 50 × 15 mm³) were purchased from Siliziumbearbeitung Holm (Tann, Germany) and were used for neutron reflectivity.

Glass substrates

For immunofluorescence measurements, 28 mm diameter round glass slides were glued to an Ibidi bottomless Petri dish (ibidi GmbH, Munich, Germany). Polydimethylsiloxane served as the gluing agent, prepared from a base and a curing agent (SYLGARD 184, Dow Corning Co., USA).

RCA cleaning

Prior to experimental use, substrates were cleaned according to the modified RCA protocol [94]. In brief, substrates were sonicated in acetone, ethanol, methanol, and water for 3 minutes. They were then immersed in a mixture of 1:1:5 (v/v/v) (H₂O₂):(30%)/(NH₄OH):(25%)/(H₂O) and soaked at 60°C for 30 minutes.

Subsequently, the substrates were washed 10× with Milli-Q water, dried at 70°C and stored in a vacuum chamber at room temperature. Before functionalization, the surface was hydrophilized using UV/Ozone Pro Cleaner (Bioforce Nanosciences) for 15 minutes.

3.1.3 Fabrication of supported membrane by vesicle fusion

While this protocol primarily explains the preparation of DOPC/PE-pAA-Cys5 (98:2 mol%) monolayer, the same method was also applied to other membrane compositions. To begin, the lipids were mixed and dried under nitrogen (N₂) gas. The resulting dry films were then stored in a vacuum overnight. To prepare the membrane, the dry film was suspended in the designated buffer for DOPC/PE-pAA-Cys5, which consisted of 10 mM Tris and 100 mM NaCl. The suspension was sonicated for 30 min. using a titanium tip sonicator S3000 (Misonix Inc., Farmingdale, USA) to yield small unilamellar vesicles (SUVs). To eliminate titanium residues from the vesicle solution caused by tip sonication, the solution was centrifuged (Eppendorf, Hamburg, Germany) for 10 minutes at 15600 rpm. This vesicle solution was stored in the refrigerator at 20°C.

3.1.4 Octadecyltrimethoxysilane (ODTMS) functionalization of substrates

To achieve a hydrophilic surface prior to functionalization with ODTMS, the substrates (HEMT or Si) were placed in a 3:1 mixture of (H₂SO₄):(H₂O₂) for 5 min. Following this step, they were thoroughly rinsed with water and dried under (N₂) gas. In the next step, they were placed in the UV-Ozone cleaner for an additional 20 min. to ensure surface hydrophilicity. After this process, the substrates were submerged in a solution containing 5% (v/v) ODTMS, toluene, and 0.5% (v/v) n-butylamine [95] for 1 hour at 10°C. The substrates were then allowed to stand for an additional 30 minutes. before being rinsed with isopropanol and dried in a vacuum at 70°C. The quality of the ODTMS layer was assessed after every preparation by measuring the contact angle [96].

3.1.5 Trimethylsilylcellulose (TMSC) substrate coating

Substrates were cleaned according to the modified RCA protocol 3.1.2. In this thesis, a stock solution of 1.2 mg/ml trimethylsilylcellulose (TMSC) dissolved in toluene was used and spin-coated onto a silicon or glass substrate using the Delta 10 spin coating (BLE Laboratory Equipment GmbH, Radolfzell am Bodensee) for 240 s at 1000 rpm. After spin coating, the samples were dried for 30 min. at 70° C and then exposed to HCl vapor to obtain the regenerated cellulose, which was subsequently rinsed thoroughly with water. The thickness and roughness of cellulose were individually measured using atomic force microscopy (AFM), X-ray reflectivity (XRR), and Ellipsometry.

3.1.6 Erythrocyte ghost membrane preparation

To prepare red blood cell (RBC) erythrocyte ghost membranes according to (Schwoch and Passow, 1973) [97], a freshly drawn 30 mL blood sample was suspended in 3 mL 100 mM EDTA to prevent blood clotting. The obtained sediment was centrifuged for 10 min. at 4000 ×g and washed 3 × with PBS (containing 50 mM PB and 150 mM NaCl). Erythrocyte ghosts were obtained by osmotic lysis of the Erys by resuspending sedimented cells in 40 × volume of ice-cold salt-free 50 mM phosphate buffer for 10 min. at 4°C. Lysed erythrocyte ghosts were centrifuged at 15000 g for 20 min. , followed by

3.1 Materials

subsequently washing $3 \times$ with PBS buffer. In the final step, the sedimented erythrocyte ghosts were resuspended in 10 mL PBS buffer (resealing) and stored at 4°C . For the determination of the protein concentration, a Bradford assay was used [98]. The malaria-infected sample was kindly prepared by the group of Prof. Dr. Michael Lanzer (CIID, Heidelberg University).

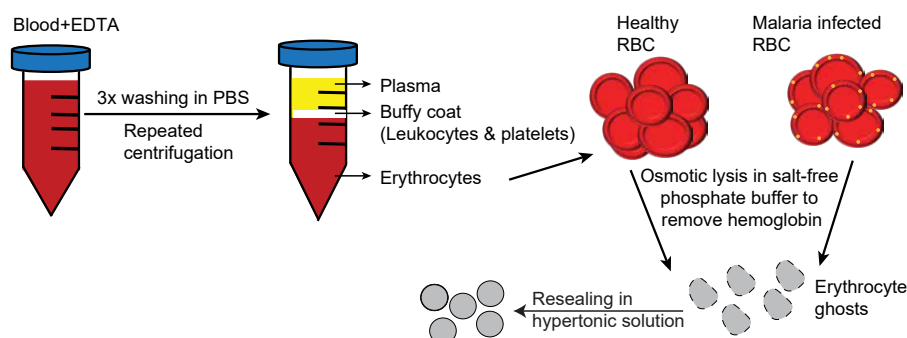


Figure 3.1: Illustration of erythrocyte ghost membrane fabrication.

3.1.7 Isolation of Sarcoplasmic Reticulum (SR) vesicle

The isolation of sarcoplasmic reticulum (SR) membranes was carried out following the method described by Hasselbach and Makinose [99]. To begin, hind leg muscles were carefully extracted from a freshly slaughtered rabbit while keeping the temperature at 4°C to preserve tissue integrity. The complete preparation was performed at 4°C and required several centrifugation steps to obtain the SR vesicles. A total of 500 g of muscle tissue was finely minced and suspended in 1.5 L of pre-chilled buffer A (2.5 mM KH_2PO_4 / 2.5 mM K_2HPO_4 , pH 7.4, 100 mM KCl, 2 mM EDTA, 1 mM DTT, 10 μM leupeptin). The mixture was homogenized for one minute using a Waring blender (Waring Laboratories, Torrington, USA). To remove myofibrils, the homogenate was centrifuged at $6,350 \times g$ for 15 minutes, and the resulting supernatant was adjusted to pH 7.4 using 7 M KOH. Mitochondria were separated by an additional centrifugation step at $8,000 \times g$ for 15 minutes. The obtained supernatant was then centrifuged at $40,000 \times g$ for 60 minutes to isolate crude SR membranes. In the next step, the pellet was resuspended in buffer B (1 mM triethanolamine, pH 7.4, 50 mM KCl, 1 M sucrose, 1 mM DTT, 10 mM leupeptin, and 0.1 μM PMSF) and homogenized using a Potter-Elvehjem tissue homogenizer (Bellco Glass Inc., NJ,

USA) with 15 strokes. This was followed by centrifugation at $4,500 \times g$ for 15 minutes. The resulting supernatant was then diluted with 1.5 times the volume of buffer C (1 mM triethanolamine pH 7.4, 1 M KCl, 160 mM sucrose, 3.35 mM ATP, 3.35 mM (MgCl_2), 1 mM DTT, 10 mM leupeptin, $0.1 \mu\text{M}$ PMSF) and subjected to ultracentrifugation at $80,000 \times g$ for 90 minutes. The resulting pellet, containing SR vesicles, was washed twice in buffer D (1 mM triethanolamine, pH 7.4, 100 mM KCl, 96 mM sucrose, 1 mM DTT, and 10 mM leupeptin) and subsequently resuspended in buffer E (1 mM triethanolamine, pH 7.4, 100 mM KCl, and 0.2% NaN_3). Finally, the SR vesicles were aliquoted into 500 μL portions, frozen in liquid nitrogen, and stored at -80°C for later use [33] [18].

3.1.8 Analysis of SR membrane Protein by SDS-PAGE

To determine the protein composition of the SR membrane, sodium dodecyl sulfate-polyacrylamide electrophoresis (SDS-PAGE) was used [100]. In the first step, 20 μg SR membranes were incubated with 50 μL Laemmli buffer (65 mM Tris/HCl pH 6.8, 3.3 wt% SDS, 5 vol% mercaptoethanol and 10 vol% glycerol) at a 1:1 (v/v) mixing ratio. This was then boiled for 5 minutes at 95°C , followed by gradual cooling to room temperature. 12 μL of this sample was loaded onto a 7.5% (w/v) polyacrylamide gel. The separated proteins were then stained by immersion in Coomassie Brilliant Blue staining for 10 min. and overnight in a destainer containing 25% (v/v) methanol and 10% (v/v) acetic acid. Proteins were identified by molecular weight standards (200 kDa to 10 kDa, Bio-Rad, Munich, Germany).

3.1.9 Immunofluorescence imaging of Sarcoplasmic reticulum and Erythrocyte membrane

SR and erythrocyte ghost membranes were characterized by fluorescence microscopy. In the first step, the SR vesicles were deposited on a glass substrate and incubated for 1 h. Throughout the experiment, all steps were carried out at room temperature. After rinsing three times with buffer E (1 mM triethanolamine, pH 7.4, 100 mM KCl), the surface was passivated with 1 mL of BSA (30 mg/mL) to prevent non-specific adsorption.

To identify (Ca²⁺-ATPase), a monoclonal SERCA2-ATPase antibody (Thermo Fisher Scientific, Karlsruhe, Germany) was added and incubated for 1 h. To remove the unbound antibody, the surface was washed with buffer E. In the last step, a secondary polyclonal antibody (goat anti-mouse IgG) Alexa Fluor 488 (Thermo Fisher Scientific, Karlsruhe, Germany) was incubated for 1 h and subsequently rinsed with buffer E [18]. Images were captured using a Nikon C2 Plus confocal microscope (Nikon Europe, Düsseldorf, Germany) with 63x and 100x objectives. They were processed using Fiji software, ImageJ. The inside labeling of the erythrocyte ghost membrane was performed similarly. PBS buffer was used for the rinsing steps. Band 3 antibody Alexa Fluor 488 (monoclonal mouse) (Novusbio, Wiesbaden, Germany) was used for labeling.

3.1.10 Synthesis of DOPE-pAA-Cys5 lipopolymer

The synthesis of the DOPE-pAA-Cys5 polymer was kindly performed and provided by Dr. Masaki Nakahata of the Department of Materials Engineering Science at Osaka University, Japan. The synthesis of DOPE-pAA-Cys5 polymer was performed by copolymerising S-trityl-cysteine-acrylamide (S-Tri-Cys-AAm) and acrylic acid (AA) with ACVA-DOPE as an initiator. The chain transfer agent used was 2-(dodecylthiocarbonothioylthio)-2-methylpropionic acid (DDMAT), and the trityl group was deprotected by the addition of trifluoroacetic acid (TFA). For this purpose, 0.05 mmol of S-Tri-Cys-AAm, 0.95 mmol of AA, 0.01 mmol of ACVA-DOPE, and 0.01 mmol of DDMAT were dissolved in 1 mL of ethanol and dried with molecular sieves 4 Å. The solution was purged with nitrogen gas. It was sealed and heated in an oil bath to 70° overnight. The solution was poured into 10 mL of diethyl ether with continuous stirring. The precipitate obtained was then centrifuged at 3500 rpm for 5 min, dissolved in 1 mL of TFA, and stirred for 1 h at room temperature. 10 mL of diethyl ether was added to the final solution, and the resulting precipitate was washed twice with an additional 10 mL of diethyl ether and then dried in a vacuum at room temperature. By ¹H-NMR, a molecular weight (M_w) of 15 kDa and a polydispersity index of 1.7 (M_w/M_n) was determined [21].

3.2 Methods

In this section, the methods and instruments used in this thesis are described, including technical specifications and measurement settings.

3.2.1 Contact angle

An Optrel Multiskop goniometer (Sinzing, Germany) was used to conduct static contact angle measurements. The goniometer is equipped with a backlight and a CCD camera. The volume of a water droplet deposited on the surface was 2.5 - 5 μL , performed at room temperature. The captured images were processed using Fiji software, ImageJ, to determine the contact angle accurately.

3.2.2 Atomic force microscopy (AFM)

For AFM measurements, a JPK Nanowizard 3 instrument (JPK Instruments AG, Berlin, Germany) was utilized to image and determine the roughness of dry cellulose. All measurements were conducted in tapping mode on a silicon substrate. An NCHV-A cantilever with a spring constant of 42 N/m and a tip radius of 8 nm (Bruker, Karlsruhe, Germany) was used. The images were taken from scan areas of $10 \times 10 \mu\text{m}^2$ at a scanning speed of 0.3 Hz. They were corrected using the plane correction option provided by the instrument.

3.2.3 Specular X-ray reflectivity (XRR) and neutron reflectivity (NR)

XRR measurements were carried out with a D8 Advance Diffractometer (Bruker, Karlsruhe, Germany). $\text{MoK}\alpha$ ($E = 17.48 \text{ keV}$, $\lambda = 0.0709 \text{ nm}$) was used as the X-ray source to ensure a sufficiently high transmission of the X-ray beam through the bulk water [9]. In a specially designed electrochemical cell with Kapton windows, the sample was positioned horizontally. NR measurements were performed at the Laue Langevin Institute's Super-ADAM beamline (Grenoble, France). In order to increase the contrast in the scattering length density, all the measurements were carried out in deuterated water (D_2O). The measurements were performed within the range ($q_z = 0 - 0.2 \text{ \AA}^{-1}$) with a monochromatic neutron beam ($\lambda = 5.21 \text{ \AA}$). XRR and NR signals have been plotted as a function of

momentum transfer (q_z), which is perpendicular to the surface of the sample,

$$q_z = \frac{(4\pi)}{\lambda} \sin(\alpha_i) \quad (50)$$

, where λ is the wavelength of the beam and α_i is the angle of incidence. Data fitting and analysis were performed with motofit [101]. For NR, background correction, direct beam normalization, and over-illumination correction were performed using pySARED software (provided by ILL). The following constraints were applied to fit both the X-ray reflectivity (XRR) and neutron reflectivity (NR) data: I) The water and silicon layers were kept constant; II) The minimum root-mean-square roughness was set at 3 Å; III) For the analysis of the SR membrane using NR, the membrane was modeled as a single slab due to the limited spatial resolution [18].

3.2.4 Grazing incidence x-ray fluorescence (GIXF)

DOPC/PE-pAA-Cys5 monolayer formation - Filmbalance experiment The isotherms were measured using a Langmuir trough (KSV Nima film balance). At the beginning of each experiment, the trough was thoroughly cleaned with ethanol and then rinsed 10 times with water. After the Langmuir trough was filled with the subphase containing I) 10 mM Tris + 100 mM NaCl, II) + CaCl₂, III) + CdCl₂, IV) + CaCl₂ + CdCl₂, the surface pressure was allowed to equilibrate for 20 min. For this experiment, a stock solution of 98:2 mol% DOPC/PE-pAA-Cys5 was prepared at a concentration of 1 mg/mL. Small droplets of the lipid stock solution were gradually brought into contact with the subphase using a Hamilton syringe to create the monolayer. Before compressing the monolayer, the solvent was evaporated for 30 minutes to ensure the removal of organic solvent residues [102].

XRR and GIXF (Grenoble) XRR and GIXF measurements were conducted at beamline ID10 of the European Synchrotron Radiation Facility (ESRF) in Grenoble. Prior to all measurements, the DOPC/PE-pAA-Cys5 monolayer was compressed to 20 mN/m on the different subphases. As the radiation source, a monochromatic synchrotron beam with a photon energy of 13 keV ($\lambda = 0.95$ Å) was used. The XRR signals were collected with a

linear detector (Mythen 1K, Dectris, Switzerland) [56] [101].

GIXF measurements were performed under identical conditions as for XRR, each subphase in the absence and presence of the DOPC/PE-pAA-Cys5 monolayer. An energy-sensitive detector (Vortex, SII NanoTechnology, USA) was used to record the X-ray fluorescence emitted by elements. All X-ray data were analyzed with respect to the scattering vector component q_z , which is normal to the interface. The parameters extracted from this characterization were used in the next step to calculate the illumination profile of the GIXF. To eliminate systematic differences between conditions in the illumination path, each characteristic element-specific emission line's intensities were normalized to the elastically scattered beam's intensity. The normalized intensity was obtained using Dr. W. Abuillan's self-written multiple Gaussian peak fitting approach in Igor (WaveMetrics, Portland, OR, USA) [102] [103].

3.2.5 Ellipsometer

Ellipsometric analyses were carried out on silicon wafers with a thermal oxide layer thickness d of 144 nm (supplied by Si-Mat, Kaufering, Germany). Using an Optrel Multiskop ellipsometer (Sinzing, Germany), measurements were performed at a specific wavelength, λ of 632.8 nm, and an incident angle of 70° . The obtained data were then subjected to fitting procedures using a custom script developed in the IGOR Pro environment (Wavemetrics, USA).

3.2.6 I-V measurement of DOPC/PE-pAA-Cys5 membrane by source/measurement unit

The current-voltage (I-V) characteristics of the HEMT substrate were studied after functionalizing the substrate with a DOPC/PE-pAA-Cys5 monolayer. The measurements were performed in a custom-designed liquid chamber at specific drain-source voltage (V_{DS}) and gate potential (V_G), utilizing a precision source/measurement unit from Keysight Technologies GmbH, Germany. Two gold needles were used to make contact with the source and the drain of the chip. To investigate the instrument's sensitivity to ionic changes, the

3.2 Methods

chamber was filled with 10 mM Tris buffer, both with and without NaCl, while varying the concentrations of CdCl₂ or CaCl₂ from 10⁻⁹ to 10⁻² M. The measurements were performed under continuous buffer flow at a rate of 200 μL/min. In the final step, 10 mM EDTA was used to wash out the divalent cations, effectively returning the system to its initial state. The drain-source current I_{DS} was monitored against V_G at various V_{DS} levels, ranging from 0 V to 0.3 V. I_{DS} was also measured versus V_{DS} at different V_G values, from -3.6 V to +0.6 V. The threshold voltage was determined from the transfer curve by a linear regression. The V_{th} was determined by the instrument as follows (see Fig.3.2).

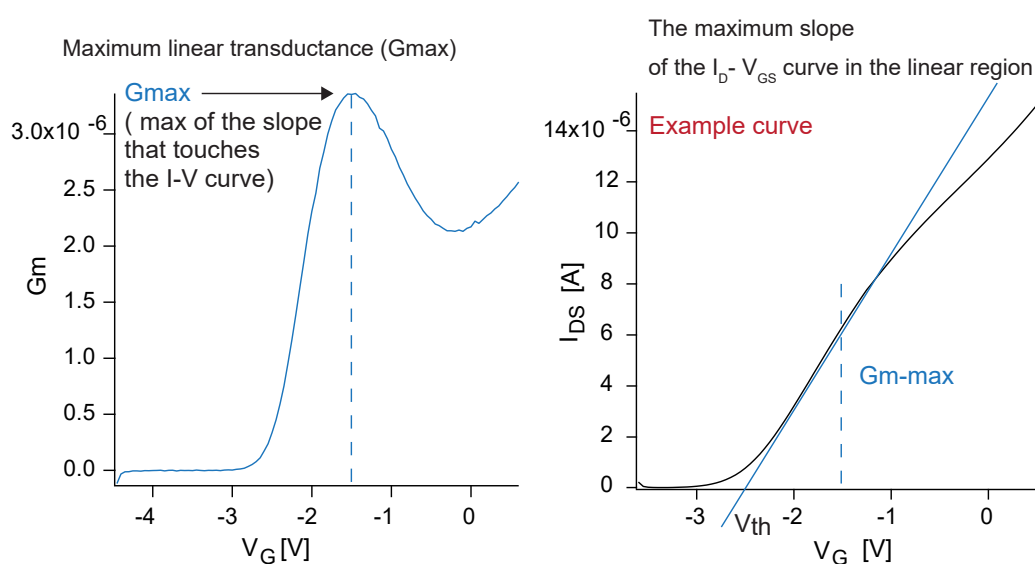


Figure 3.2: Graphical representation for determining the threshold voltage (V_{th}) based on the instrument used.

4 Ion-specific recognition on the membrane surface

4.1 Detection of Heavy Metal Ions in Aqueous Environment Using GAN/AlGaN High Electron Mobility Transistors Functionalized with Plant-Inspired Polymers

In this section, the influence of ionic strength on the transistor response on a HEMT functionalized surface with a DOPC/PE-pAA-Cys5 monolayer using two buffers is investigated. Buffer 1 contained 10 mM Tris and 100 mM NaCl, and Buffer 2 contained only 10 mM Tris. 1 nM – 10 mM CdCl₂ or CaCl₂ was added to buffer 1 or buffer 2 to examine the reactivity to divalent ions Cd²⁺ and Ca²⁺. Further, 10 mM EDTA was added to examine whether the system could be regenerated after removing divalent cations.

4.1.1 Characterization of lipid monolayer incorporating DOPE-pAA-Cys5

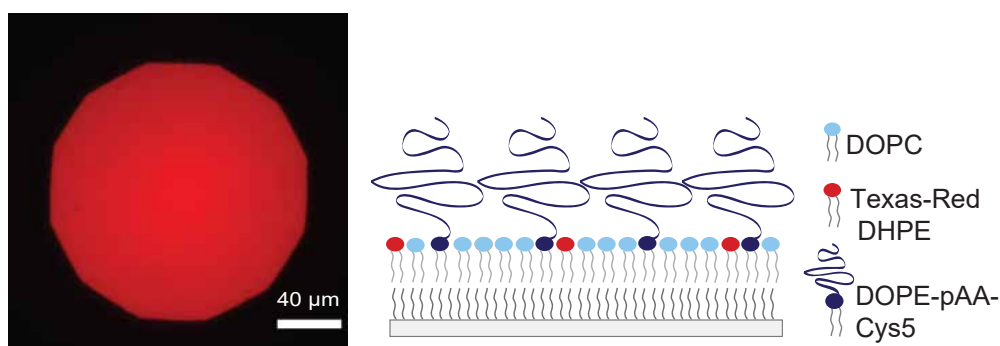


Figure 4.1: Fluorescence microscopy image of a DOPC monolayer incorporating 2 mol% DOPE-pAA-Cys5 deposited on the ODTMS-coated glass substrate, labeled with 0.2 mol% TexasRed DHPE (Illustration of DOPC/PE-pAA-Cys5 monolayer on a glass substrate).

To assess the homogeneity of the DOPC/PE-pAA-Cys5 monolayer, fluorescence microscopy was used for detailed analysis of the membrane's surface. Figure 4.1 illustrates a DOPC monolayer incorporating 2 mol% DOPE-pAA-Cys5 deposited on an ODTMS monolayer through vesicle fusion. By taking into account the area per lipid molecule in the fluid phase $A \approx 0.6 \text{ nm}^2$ and the average distance between the DOPE-pAA-Cys5 molecules

$\langle d \rangle$, which is estimated from the molar fraction of the lipopolymer χ , the average distance $\langle d \rangle$ is determined as follows [21] [19]:

$$\langle d \rangle = (A/\chi_{lipo})^{0.5} \sim 5.5 \text{ nm} \quad (51)$$

Homogeneous monolayer formation was confirmed by confocal fluorescence imaging with Nikon C2 Plus (Nikon Europe, Düsseldorf, Germany). For that purpose, the ODTMS lipid monolayer was deposited on a glass substrate, and 0.2 mol% TexasRed DHPE was used to label the lipid matrix [19] [104]. The fluorescence image indicates a saturated relative fluorescence intensity signal with a homogeneous monolayer distribution (Figure 4.1).

4.1.2 Sensing of Cd^{2+} and Ca^{2+} ions in the presence of supporting salt (buffer 1)

Prior to the deposition of the lipopolymer monolayer, the hydrophobic nature of the ODTMS-coated surface was confirmed by measuring the water contact angle, which was found to be $\theta \geq 90^\circ$. This value is required for the deposition of a lipid monolayer by vesicle fusion [25] [105].

Figure 4.2a represents the HEMT functionalized surface with a DOPC/PE-pAA-Cys5 monolayer in the presence of $0 - 10^{-2}$ M CdCl_2 in buffer 1. Here, the drain-source current (I_{DS}) is plotted against the gate voltage (V_{G}). Buffer 1 simulates physiological conditions, containing 100 mM NaCl buffered with 10 mM Tris (pH 7.4). The $I_{\text{DS}} - V_{\text{G}}$ curve in Figure 4.2a shows the average and standard deviation from three independent measurements. The increase in the data near the onset of I_{DS} ($V_{\text{G}} = -2.5 \sim -1.5$ V) is shown in Figure 4.2b. The increase in Cd^{2+} concentration results in a continuous shift of the $I_{\text{DS}} - V_{\text{G}}$ curves, while the slope remains nearly unchanged. The data point Ctrl (black symbol) in Figure 4.2c refers to the control measurement taken after vesicle fusion once the system reaches a steady state. The obtained data indicate that the binding of Cd^{2+} ions to the pAA-Cys5 lipopolymer results in a shift of the threshold voltage V_{th} . V_{th} is obtained by the linear extrapolation of the maximum transconductance G_{max} (see theory section 3.2). The maximum transconductance G_{max} remained almost constant throughout the experiment, $G_{\text{max}} \approx 8.2 \mu\text{S}$.

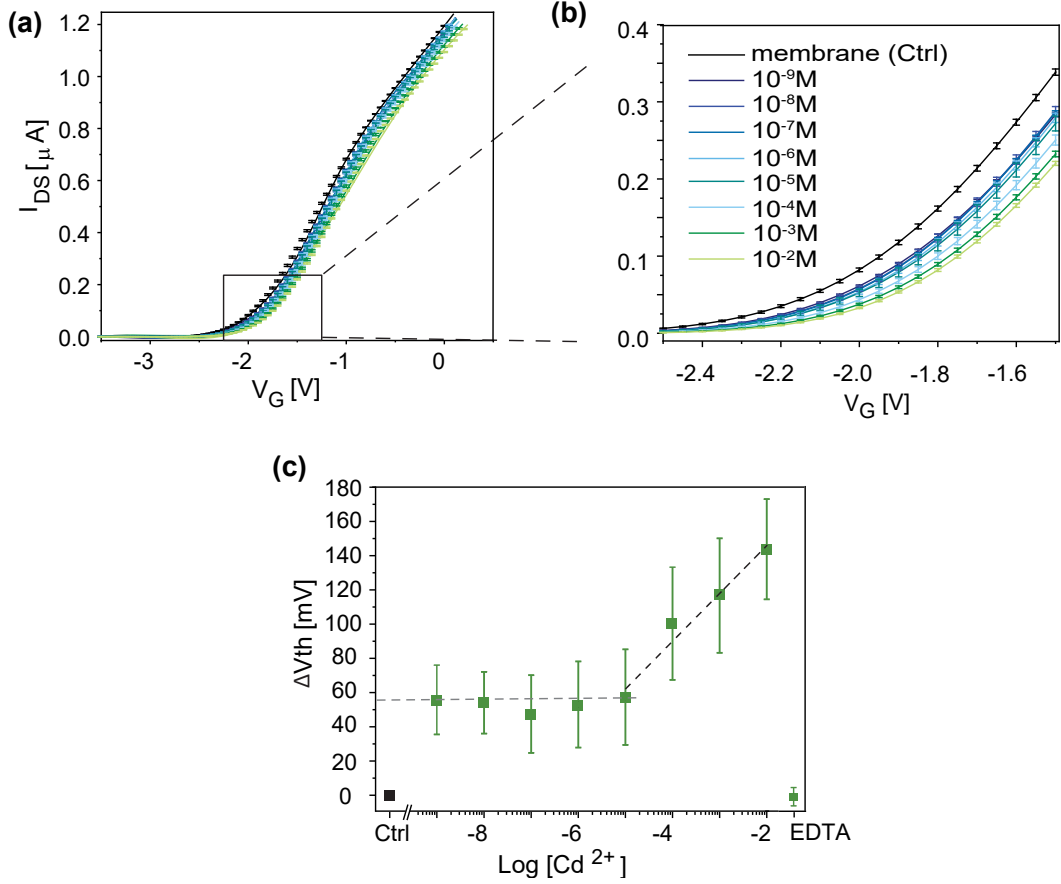


Figure 4.2: (a) and (b) Drain-source current (I_{DS}) plotted against the gate voltage (V_G) for HEMT functionalized with a DOPC/DOPE-pAA-Cys5 monolayer in the absence and the presence of 10^{-2} M – 10^{-9} M CdCl_2 in buffer 1 at $V_{DS} = 0.3$ V . (c) Threshold voltage V_{th} determined from the maximum conductance plotted against $\log[\text{Cd}^{2+}]$.

In Figure 4.2c, the threshold voltage ΔV_{th} is plotted against the log of the Cd^{2+} concentration. Each dataset comprises three independent measurements, including the mean and its corresponding standard deviation. The detailed values of V_{th} and G_{max} are summarized in Table 2. The addition of 10^{-9} M CdCl_2 to buffer 1 resulted in a significant change in the threshold voltage, $\Delta V_{th} = 55.8 \pm 20.2$ mV. This concentration agrees with the dissociation constant determined by isothermal titration calorimetry (ITC) by M. Nakahata et al., which was in the order of $K_D \sim 10^{-9}$ M [19]. The change in the V_{th} can be seen as a result of the binding of the Cd^{2+} ions to the pAA-Cys5 polymer. By increasing the concentration of Cd^{2+} from 10^{-9} to 10^{-5} , no significant change in the threshold voltage can be seen. From the concentration of 10^{-5} up to 10^{-2} , a steep linear

4.1 Detection of Heavy Metal Ions in Aqueous Environment Using GAN/AlGaN High Electron Mobility Transistors Functionalized with Plant-Inspired Polymers

increase of the threshold voltage can be observed. With this, a clear dependency between the concentration of Cd^{2+} to V_{th} can be demonstrated. Here, the slope of the linear range was determined to be 28.0 ± 3.4 mV for a 10-fold difference in Cd^{2+} ion concentration. This result is in accordance with the Nernstian behavior $z = 2$, where the system follows a theoretical model for a two-electron transfer process, reflecting a distinct interaction with Cd^{2+} ions. In the final step, the system was rinsed with buffer 1, which contained 10 mM EDTA. This step resulted in the decrease of $\Delta V_{\text{th}} = -1.3 \pm 5.9$ mV. This last experiment clearly demonstrates that the binding of Cd^{2+} is a reversible process. These results are consistent with those of M. Nakahata et al., who demonstrated that a water treatment system using the same pAA-Cys5 polymers could recover after EDTA treatment [19].

Table 2: List of ΔV_{th} and ΔG_{max} for Cd^{2+} and Ca^{2+} ions in buffer 1.

buffer 1	Cd^{2+} in buffer 1		Ca^{2+} in buffer 1	
	ΔV_{th} [mV]	ΔG_{max} [μS]	ΔV_{th} [mV]	ΔG_{max} [μS]
0	0	8.2 ± 0.4	0	13.5 ± 0.4
$[\text{Cd}^{2+}] = 10^{-9}$ M	55.8 ± 20.2	8.2 ± 0.8	5.7 ± 2.9	13.4 ± 0.6
$[\text{Cd}^{2+}] = 10^{-8}$ M	54.0 ± 18.0	8.2 ± 0.7	6.3 ± 2.9	13.2 ± 0.7
$[\text{Cd}^{2+}] = 10^{-7}$ M	47.5 ± 22.8	8.1 ± 0.6	6.3 ± 2.6	13.2 ± 0.7
$[\text{Cd}^{2+}] = 10^{-6}$ M	53.0 ± 25.2	8.0 ± 0.6	6.5 ± 2.5	13.2 ± 0.5
$[\text{Cd}^{2+}] = 10^{-5}$ M	57.3 ± 28.0	8.0 ± 0.6	5.9 ± 2.4	13.2 ± 0.4
$[\text{Cd}^{2+}] = 10^{-4}$ M	100.3 ± 33.0	8.0 ± 0.8	8.0 ± 2.0	13.3 ± 0.4
$[\text{Cd}^{2+}] = 10^{-3}$ M	116.7 ± 33.5	8.0 ± 0.8	15.9 ± 3.3	13.3 ± 0.4
$[\text{Cd}^{2+}] = 10^{-2}$ M	143.8 ± 29.3	8.0 ± 0.9	25.7 ± 3.2	13.2 ± 0.4
EDTA	-1.3 ± 5.9	8.2 ± 0.6	2.1 ± 1.8	13.8 ± 0.2
buffer 1	3.7 ± 30.3	8.2 ± 2.0	–	–

The experiment was repeated to investigate the selectivity of pAA-Cys5 polymer to different divalent cations. Here, Cd^{2+} ions were replaced with Ca^{2+} ions in buffer 1. With this, the ion-specific response of the pAA-Cys5 polymer in a controlled environment can be investigated.

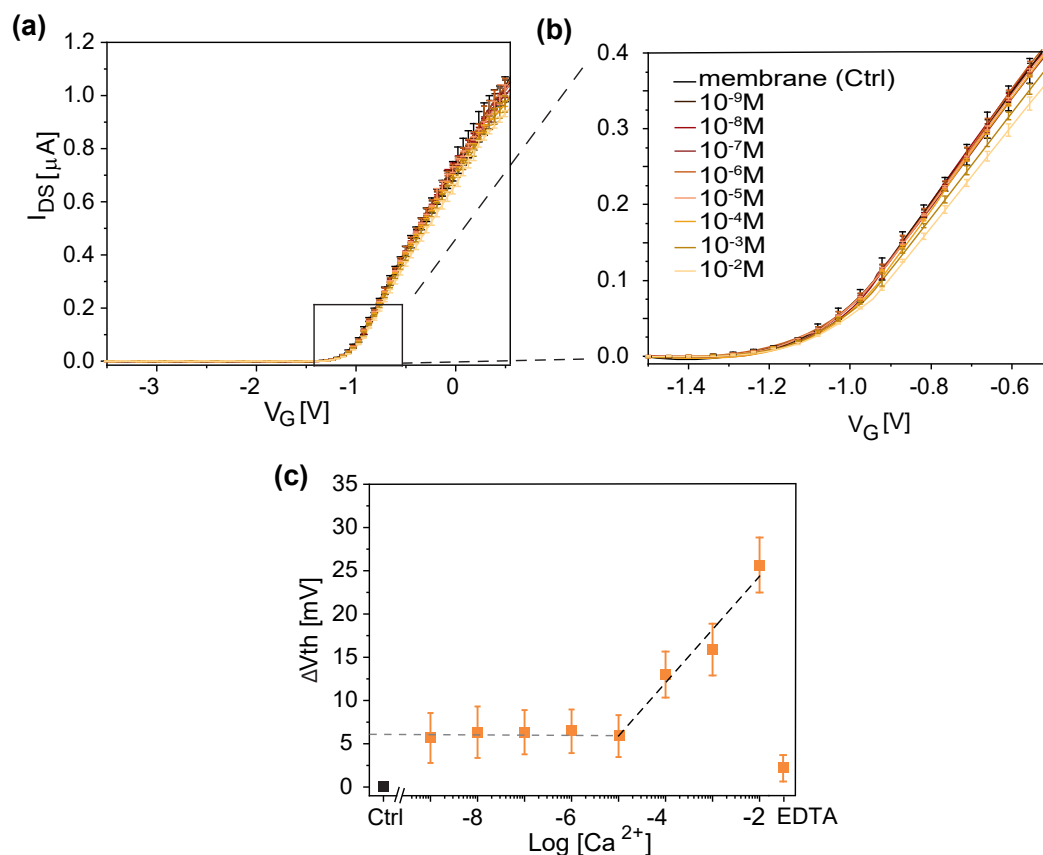


Figure 4.3: (a) I_{DS} against V_G for HEMT functionalized with a DOPC/DOPE-pAA-Cys5 monolayer, measured in buffer 1 in the absence and the presence of 10^{-9} M – 10^{-2} M CaCl_2 at $V_{DS} = + 0.3$ V and (b) Threshold voltage V_{th} plotted against $\log[\text{Ca}^{2+}]$.

Figure 4.3a, b show the transfer curves (I_{DS} vs. V_G) of the DOPC/DOPE-pAA-Cys5 monolayer in buffer 1 with the concentration series of 10^{-2} to 10^{-9} M for CaCl_2 . Under these conditions, a similar response was observed, similar to that previously observed with Cd^{2+} . The I-V curves shift in a more positive direction by variation/increase of the concentration of Ca^{2+} . However, this shift is much smaller and less pronounced than that observed with buffer 1 containing Cd^{2+} . As shown in Figure 4.3b, the shift becomes more pronounced as the concentration increases from 10^{-5} to 10^{-2} . The shift in the V_{th} suggests an increase while the G_{max} remains constant $\approx 13.5 \mu\text{S}$ (detailed summary of values shown in 2). Further in Figure 4.3c ΔV_{th} is plotted against $\text{Log}[\text{Ca}^{2+}]$. After the membrane deposition (Ctrl), the addition of 10^{-9} to buffer 1 results in an increase of $\Delta V_{th} = 5.7 \pm 2.9$ mV, which was almost ten-fold smaller than the response observed with the same buffer

containing 10^{-9} CdCl₂. From 10^{-9} to 10^{-5} , ΔV_{th} remains almost constant, and by changing the buffer to a higher concentration from 10^{-5} onwards, the linear increase of ΔV_{th} is exhibited. By fitting the linear range of the data, a slope of 6.2 ± 0.8 mV is identified. This increase is four times smaller than that of Cd²⁺ in buffer 1.

These data indicate that the pAA-Cys5 monolayer on HEMT detects Cd²⁺ ions more sensitively than Ca²⁺ ions. The observed different selectivity/sensitivity in response to Cd²⁺ and Ca²⁺ ions can be explained by their dissociation constants (K_D), reflecting differences in their binding affinities to the polymer system. In particular, the K_D of pAA-Cys5 for Ca²⁺ ions is $K_D \approx 10^{-5}$ M, four orders of magnitude larger than that of Cd²⁺ ions. This explains the stronger response in the case of Cd²⁺ since more binding sites on the pAA-Cys5 polymer are occupied [19].

4.1.3 Sensitivity and Selectivity of Sensor Response in the Presence and Absence of Supporting salt

In this study, the functionalized HEMT substrate has so far been investigated under physiological conditions in buffer 1 with 0 to 10^{-2} M CdCl₂ or CaCl₂. Considering the Debye Hückel theory, the system's response would decrease at higher ionic strength. This phenomenon is attributed to the charge screening, which is limited in higher concentrated ion solutions and thus reduces the sensor's sensitivity to the ion in solution [106] [107].

To investigate the Debye screening effect, the functionalized DOPC/DOPE-pAA-Cys5 monolayer was measured in the absence of supporting salt (100 mM NaCl). To maintain the pH at 7.4, only 10 mM Tris was used in buffer 2 (see detailed values, Table 3).

Figure 4.4a, b represent ΔV_{th} against Log[Cd²⁺] (green symbols) and Log[Ca²⁺] (orange symbols). A linear increase from 10^{-5} to 10^{-2} M was also observed in this experiment. However, the sensor response was much weaker; the value obtained from the slope for Cd²⁺ in buffer 2 was 6.4 ± 0.7 mV, while Cd²⁺ in buffer 1 was 28.0 ± 3.4 mV. This shows a four times smaller response. The same was observed for the Ca²⁺ data, where the response was also reduced (3.9 ± 0.1 mV) compared to buffer 1 (6.2 ± 0.8 mV).

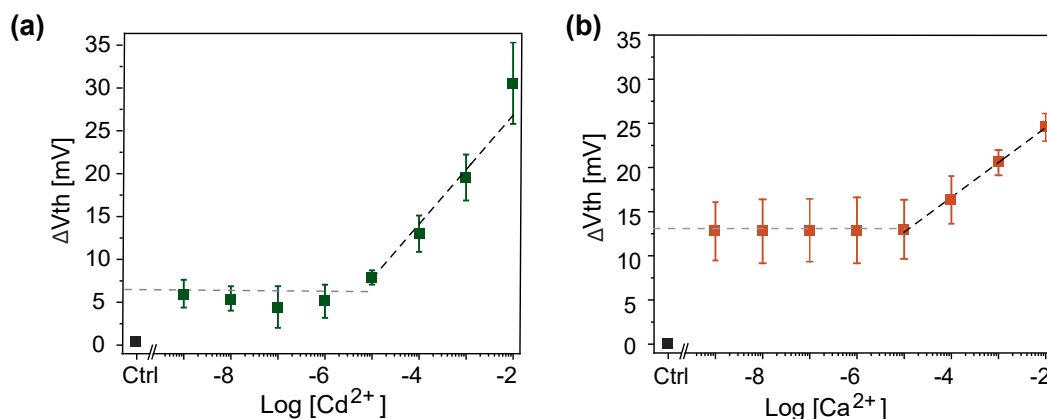


Figure 4.4: $V_{th} - \log[M^{2+}]$ plots of the HEMT functionalized with DOPC/DOPE-pAA-Cys5 monolayer, measured in buffer 2 containing (a) Cd²⁺ and (b) Ca²⁺

Table 3: List of ΔV_{th} and ΔG_{max} for Cd²⁺ and Ca²⁺ ions in buffer 2.

buffer 1	Cd ²⁺ in buffer 2		Ca ²⁺ in buffer 2	
	ΔV_{th} [mV]	ΔG_{max} [μ S]	ΔV_{th} [mV]	ΔG_{max} [μ S]
0	6.0 \pm 1.6	6.7 \pm 0.5	12.8 \pm 3.3	3.2 \pm 1.1
[Cd ²⁺] = 10 ⁻⁹ M	6.0 \pm 1.6	6.7 \pm 0.4	12.8 \pm 3.3	3.2 \pm 1.1
[Cd ²⁺] = 10 ⁻⁸ M	5.4 \pm 1.4	6.7 \pm 0.6	12.8 \pm 3.6	3.3 \pm 0.7
[Cd ²⁺] = 10 ⁻⁷ M	4.5 \pm 2.4	6.7 \pm 1.0	12.9 \pm 3.6	3.3 \pm 1.1
[Cd ²⁺] = 10 ⁻⁶ M	5.1 \pm 1.9	6.7 \pm 0.8	13.3 \pm 3.3	3.3 \pm 0.8
[Cd ²⁺] = 10 ⁻⁵ M	7.9 \pm 0.8	6.6 \pm 0.6	13.3 \pm 3.3	3.3 \pm 0.8
[Cd ²⁺] = 10 ⁻⁴ M	13.0 \pm 2.1	6.6 \pm 0.8	16.3 \pm 2.7	3.2 \pm 1.3
[Cd ²⁺] = 10 ⁻³ M	19.6 \pm 2.7	6.9 \pm 0.9	20.9 \pm 3.3	3.3 \pm 1.4
[Cd ²⁺] = 10 ⁻² M	30.6 \pm 4.7	6.9 \pm 0.9	24.6 \pm 1.6	3.3 \pm 1.2
EDTA	1.0 \pm 2.0	6.7 \pm 1.8	6.2 \pm 1.4	3.3 \pm 1.2
buffer 1	–	–	2.7 \pm 0.3	3.3 \pm 1.2

These results indicate that the response is not shielded but enhanced in the presence of a higher supporting salt (buffer 1), suggesting a distinctly different behavior of the pAA-Cys5 polymer in buffers 1 and 2. These results cannot, therefore, be explained by the Debye Hückel theory. Several factors need to be considered to explain these results. In general, the higher sensitivity of Cd²⁺ compared to Ca²⁺ on the HEMT functionalized surface can be attributed to the high affinity of Cd²⁺, ($K_D = 10^{-9}$) [19] [108].

4.1 Detection of Heavy Metal Ions in Aqueous Environment Using GAN/AlGaN High Electron Mobility Transistors Functionalized with Plant-Inspired Polymers

Another factor is the conformational change of the pAA-Cys5 chains in contact with divalent cations in electrolyte solutions. This conformational change was previously reported by Yamamoto et al.[21], who studied the same polymer used in this research in buffer 1 by atomic force microscopy with frequency modulation detection (AFM-FM). The 2D height map of the monolayer showed a homogeneous distribution and low roughness. In the 3D frequency map, the addition of 1 mM Cd^{2+} ions resulted in a heterogeneous distribution, indicating a collapse of the polymer chains due to Cd^{2+} trapping, whereas the addition of Ca^{2+} ions resulted in a uniform, less compacted layer.

Following the analysis of the pAA-Cys5 polymer in buffer 1 (with 100 mM NaCl), the second finding, the weaker response in buffer 2 (no NaCl), is analyzed. The weaker response in buffer 2 can be attributed to both conformational changes and electrostatic repulsions between the polymer chains. Previous work by Rehfeldt et al.[109] demonstrated the deposition of a monolayer with attached poly[2-(dimethylamino)ethyl methacrylate-block-methyl methacrylate] (PDMAEMA-PMMA) diblock copolymer, consisting of a weak polyelectrolyte block and a hydrophobic PMMA block, at the air/water interface. It was found that by changing the pH of the monolayer (charging it), the polymer conformation changes. In the neutral state at pH 8.5 it adsorbs to the air/water interface, while in the charged state at pH 5.5 it stretches into the subphase, resulting in a decrease in surface pressure. Taking into account the electrostatic repulsion between the polymer chains, the average distance between the pAA-Cys5 chains is 5.5 nm, and the electrostatic repulsion between the neighboring polymer chains hinders chain compaction and binding of Cd^{2+} , resulting in stretched polymer chains.

4.2 Specific localization of ions in Plant-Inspired polymers at the air/water interface

In this section, the influence of M^{2+} ions on the structure and electrostatics of DOPC/PE-pAA-Cys5 monolayer is investigated at the air/water interface using both X-ray reflectivity (XRR) and grazing incidence X-ray fluorescence (GIXF). At first, the pressure-area isotherms of the monolayer were recorded in different subphases. Next, XRR was used to analyze structural changes, while GIXF provided information about the ion concentration profiles perpendicular to the monolayer surface. The concentration profiles were determined from the signals recorded at incidence angles below the critical angle (surface-dominated signal) and above the critical angle (bulk-dominated signal).

The experimental data were fitted using Eq.40, which corresponds to [28]:

$$I_{\text{relative}} = \frac{I_{\text{normalized (pAA-Cys5 monolayer)}}}{I_{\text{normalized (buffer)}}} \quad (52)$$

The intensity of the illumination was determined based on the values obtained from the XRR fittings.

4.2.1 Pressure-Area Isotherms of DOPE-pAA-Cys5 monolayer

Prior to the XRR and GIXF measurement, the monolayer behavior was studied by surface pressure-area experiments in the presence of 1 mM Ca^{2+} and 1 mM Cd^{2+} ions as well as the combination of both ions in the subphase, using a Langmuir trough.

Figure 4.5 shows the surface pressure-area isotherms of the pAA-Cys5 monolayer system measured on different subphases. As subphases, 100 mM NaCl and 10 mM Tris were used. By compression of the monolayer, observed at a molecular area of $\sim 250 \text{ \AA}^2$, the onset of the pressure increased. Under all these different conditions, a surface area per molecule of $\sim 90 \text{ \AA}^2$ was reached. The subphase containing 1 mM Cd^{2+} indicated a slightly steeper trend, indicating an increased molecular interaction and, thus, a more compact monolayer. This can be explained by the unique characteristics of the pAA-Cys5 polymer. Here, Cd^{2+} ions bind to and compensate for the negative $-\text{COOH}$ charges in the polymer, leading to its compaction [9].

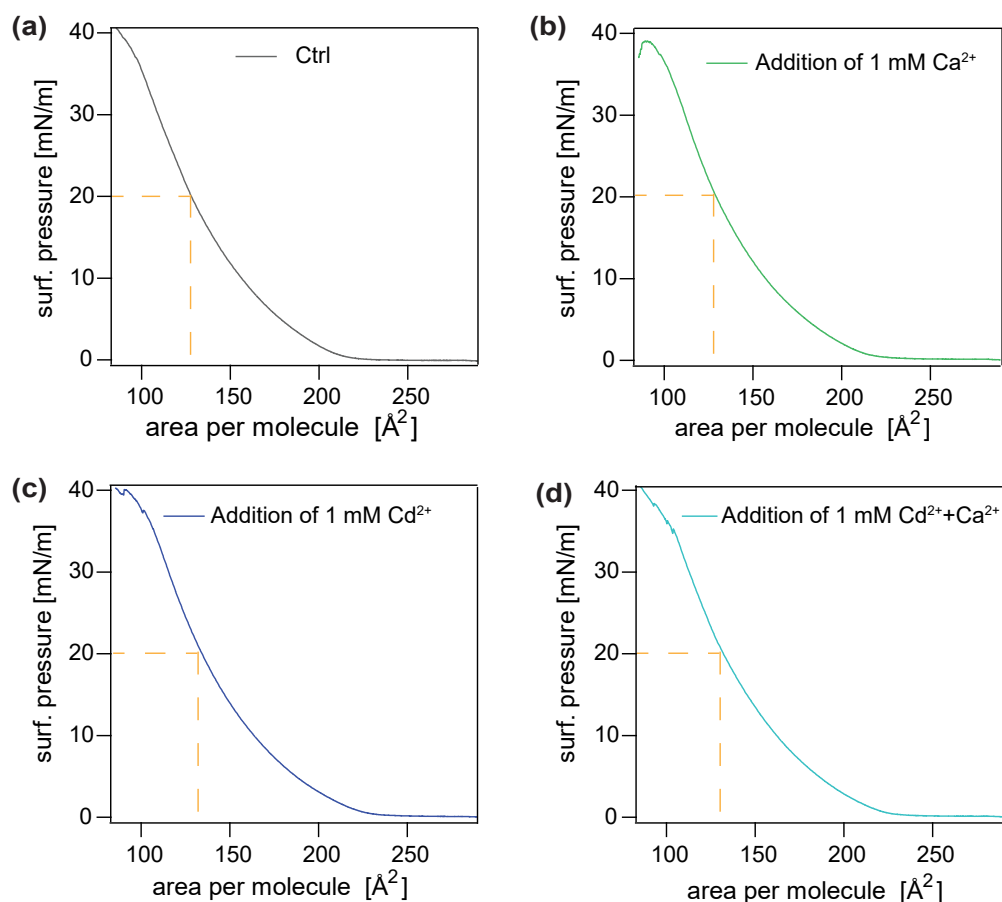


Figure 4.5: Pressure-area isotherms of DOPC/PE-pAA-Cys5 monolayer in (a) 100 mM NaCl + 10 mM Tris (Ctrl), (b) 100 mM NaCl + 10 mM Tris + 1 mM CaCl₂, (c) 100 mM NaCl + 10 mM Tris + 1 mM CdCl₂, (d) 100 mM NaCl+10 mM Tris + 1 mM CdCl₂ + 1 mM CaCl₂ subphase at 20 ° C and pH 7.4

The monolayer systems were compressed up to $\pi = 20$ mN/m, indicated by the dashed yellow line in Figure 4.5. At this surface pressure, the mean molecular area for the DOPC/PE-pAA-Cys5 monolayer was determined to be 128 Å². When the subphase was changed by the addition of 1 mM CaCl₂, the molecular area remained the same at 129 Å². Similarly, the addition of 1 mM CdCl₂ increased the molecular area to 134 Å². However, when a mixture of 1 mM CaCl₂ and 1 mM CdCl₂ was introduced, the molecular area decreased to 132 Å². These results were then used to calculate the ion concentration within the monolayer in the GIXF analysis.

4.2.2 Influence of M^{2+} ions on pAA-Cys5 monolayer (XRR and GIXF)

The DOPE-pAA-Cys5 monolayer was compressed up to $\pi = 20$ mN/m. Figure 4.6 represents reflectivity Rq_z^4 plotted against the momentum transfer q_z . XRR experimental curves (open circles) and best-fit results are indicated by a black line with χ^2 being 0.003 and Figure 4.6b representing the corresponding electron density profile (SLD). The DOPE-pAA-Cys5 polymer brush monolayer with no additional ions added, control (Ctrl) is modeled using a slab model. For this system, three slabs were defined: an alkyl chain, outer headgroup, and pAA-Cys5 polymer brush.

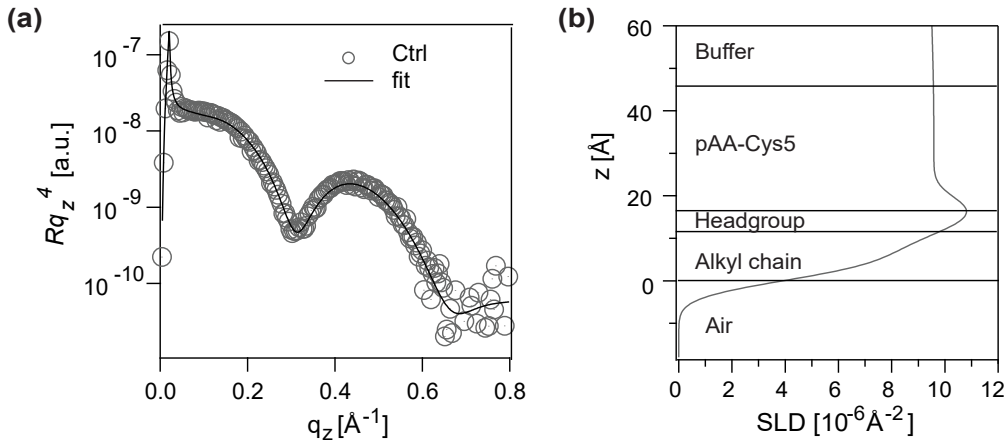


Figure 4.6: (a) XRR data with best fit (black line) for DOPE-pAA-Cys5 monolayer (Ctrl) (b) Reconstructed electron density profile.

By analyzing the XRR data, the thickness d , scattering length density (SLD), and roughness σ were determined and are listed in Table 4. The average distance $\langle d \rangle$ between the DOPE-pAA-Cys5 molecules was determined as follows

$$\langle d \rangle = (A/\chi_{lipo})^{0.5}. \quad (53)$$

Using a molar fraction of 2 mol% for DOPE-pAA-Cys5 and taking into account the area per lipid of $A \sim 60 \text{\AA}^2$, the average grafting distance was determined to be 5.5 nm [21] [19]. The total thickness of the monolayer at the air/water interface is $d = 19.2 \text{\AA}$. This result is consistent with the previously reported thickness for monolayer systems (OPPC,

DOPC/DOPS) by A.Korytowski et al. with 19.6 \AA and A.Makky et al. with 19.1 \AA [110] [111]. The SLD values obtained for the alkyl chain and head group of $(7.5 \pm 0.8) \times 10^{-6} \text{ \AA}^{-2}$ and $(11.7 \pm 0.1) \times 10^{-6} \text{ \AA}^{-2}$ are slightly smaller but remain within the same order as in the reported literature. The pAA-Cys5 polymer brush indicates a thickness of $28.2 \pm 12.0 \text{ \AA}$ and an SLD value of $(9.6 \pm 0.1) \times 10^{-6} \text{ \AA}^{-2}$. The SLD of the polymer slab is close to that of the buffer, indicating a fully hydrated layer. This results in a low contrast between the polymer-buffer interface.

The addition of 1 mM CdCl_2 leads to a pronounced change in the thickness of the pAA-Cys5 layer (Figure 4.7a). This is evident by the shift of the first minimum at $0.31 q_z$ towards a higher q value.

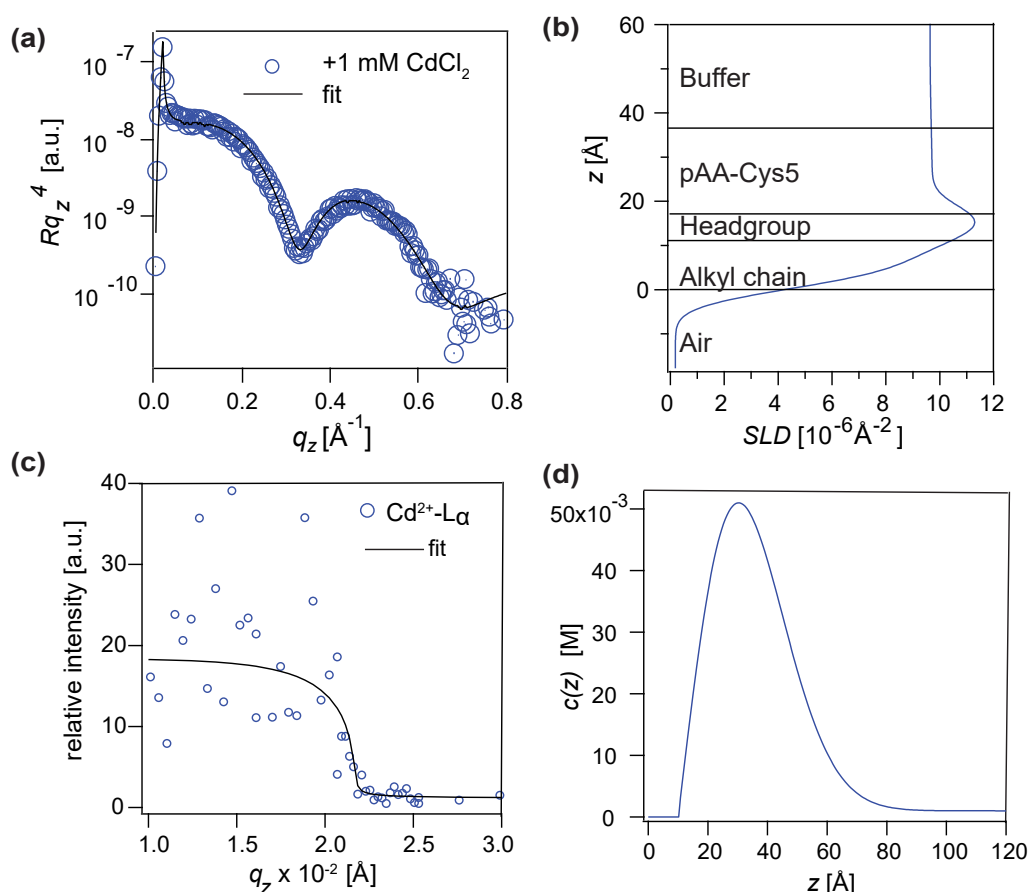


Figure 4.7: (a)+(b) XRR data (open circles) with reconstructed electron density profiles for DOPC/PE-pAA-Cys5 monolayer in the presence of 1 mM CdCl_2 , (c)+(d) Fluorescence intensity as a function of q_z for $\text{Cd} L_\alpha$ signal with corresponding ion concentration profile.

The thickness decreases to $d = 20.7 \pm 12.1 \text{ \AA}$, which is a decrease of 7.5 \AA compared to the control system. The SLD slightly increased to $(9.7 \pm 0.1) \times 10^{-6} \text{ \AA}^{-2}$ compared to the control. The decrease in thickness in the layers, due to the addition of Cd^{2+} ions can be explained by a conformational change of the pAA-Cys5 polymer. As previously mentioned (see section 4.1.2), the pAA-Cys5 polymer exhibits a high affinity towards selected ions in solution. The conformational change in the polymer is attributed to the complex formation of the Cd^{2+} ion with the CH_2S^- and COO^- groups, resulting in the compaction of the polymer [19]. Further, the thickness of the monolayer decreases to 18.2 \AA , whereby the SLD of the alkyl chain and headgroup, $(8.5 \pm 0.3) \times 10^{-6} \text{ \AA}^{-2}$ and $(11.9 \pm 0.1) \times 10^{-6} \text{ \AA}^{-2}$, slightly increases (see Table 4). This indicates a reduction of water in the layer.

Figure 4.7b represents the normalized x-ray fluorescence signal from DOPC/PE-pAA-Cys5 monolayer with 1 mM Cd^{2+} loaded subphase as a function of q_z . The normalized signal is obtained by normalizing the sample signal to the corresponding reference blank buffer. The fluorescence signal is collected above ($q_c = 0.022 \text{ \AA}^{-1}$) and below the critical angle. The best fit (solid line) result was calculated by Eq.41. The corresponding ion concentration profile of Cd^{2+} ions was calculated by Eq.42. For the DOPC/PE-pAA-Cys5 monolayer the reconstructed ion concentration profile of Cd^{2+} has its maximum concentration at $c_{\text{max}(\text{Cd}^{2+})} = 0.05 \text{ M}$, at the peak position $z_{\text{max}(\text{Cd}^{2+})} = 30.1 \text{ \AA}$ from air/chain interface. The maximum concentration obtained from the surface is 50 times higher than in the bulk (1 mM CdCl_2). Further, this peak position corresponds to the center of the polymer brush. For pAA-Cys5 monolayer in the presence of Cd^{2+} (Figure 4.5), the calculated lateral density of Cd^{2+} ions corresponds to $c_{\text{L}(\text{Cd}^{2+})} = 1.5 \times 10^{13} \text{ ions/cm}^2$. The lateral density was determined by integrating the excess ion concentration along the z-axis. From the lateral density, the number N of Cd^{2+} binding to one pAA-Cys5 brush was determined as $N = 10$ for $A = 134 \text{ \AA}^2$ at 20 mN/m . Assuming that one cadmium ion is bound to one cysteine and that the DOPE-pAA-Cys5 polymer contains 5 mol\% of cysteine, this would give a calculated total length of 200 monomers. Based on these assumptions, the molecular weight can be estimated by:

4.2 Specific localization of ions in Plant-Inspired polymers at the air/water interface

$$[10x(M_{\text{acrylic acid}} + M_{\text{cysteine}}) + 190xM_{\text{acrylic acid}} + M_{\text{DOPE}}] = 16.3 \text{ kDa} \quad (54)$$

This is in good agreement with the molecular weight determined by Prof. M. Nakahata for DOPE-pAA-Cys5 by GPC (15 kDa).

In the next experiment, the divalent cations were changed to 1 mM Ca^{2+} . In comparison to the control, neither the thickness of the monolayer (18.6 Å) nor the brush thickness (27.9 ± 9.4 Å) nor the SLD ($(9.6 \pm 0.1) \times 10^{-6} \text{ \AA}^{-2}$) changed significantly (see Table 4).

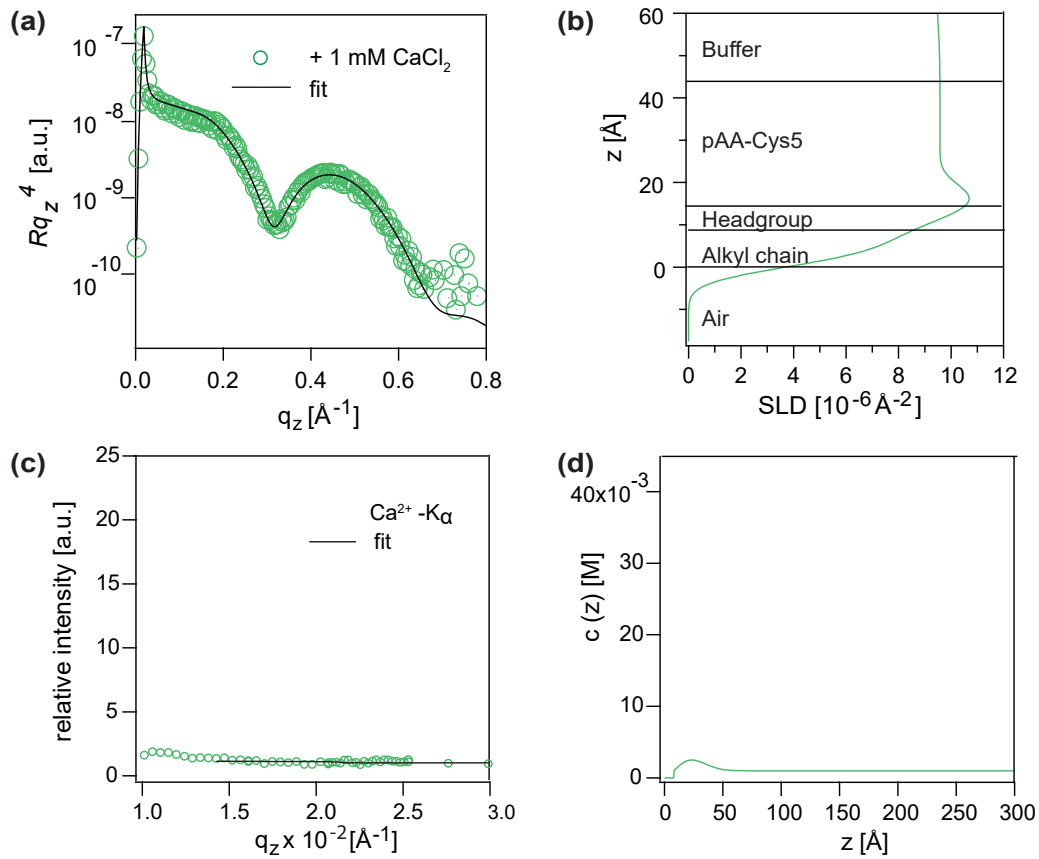


Figure 4.8: (a)+(b) XRR data with reconstructed electron density profiles for DOPC/PE-pAA-Cys5 monolayer in the presence of 1 mM CaCl_2 , (c) Fluorescence intensity as a function of q_z for Ca^{2+} K_α signal. The data could not be fitted, bulk intensity is indicated by dashed line

Due to the weak fluorescence intensity signal of Ca^{2+} ions, no fit could be generated for these data. There was no pronounced enhancement of the signal with Ca^{2+} ions (dashed

line corresponding to the bulk concentration of 1 mM Ca^{2+}) Figure 4.8b.

The presence of Ca^{2+} and Cd^{2+} ion as a mixture in the subphase results in a minor increase in thickness, $d = 24.1 \pm 7.9 \text{ \AA}$ compared to the sample only containing Cd^{2+} .

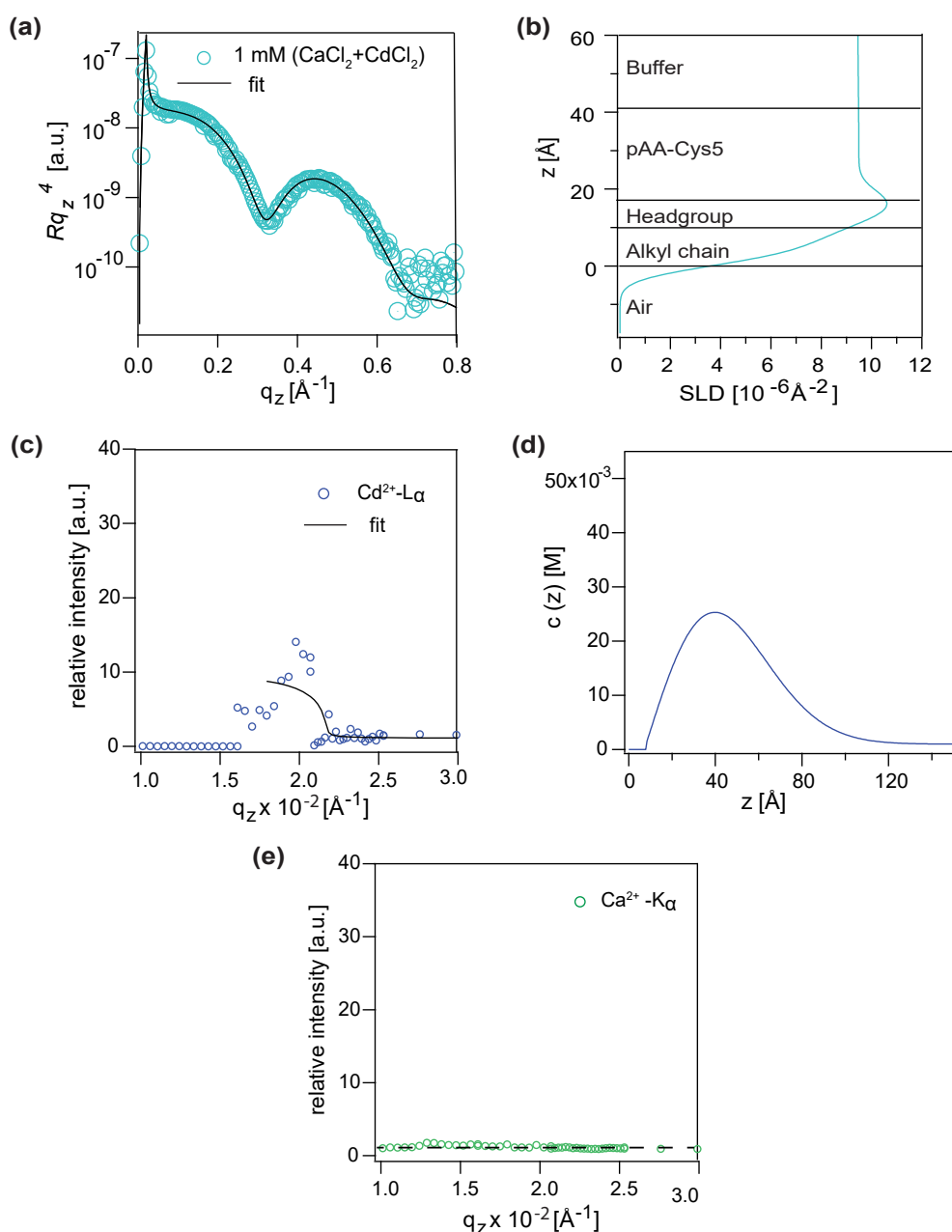


Figure 4.9: (a)+(b) XRR data with reconstructed electron density profiles for DOPC/PE-pAA-Cys5 monolayer in the presence of 1 mM $(\text{CaCl}_2 + \text{CdCl}_2)$, (c)+(d) Fluorescence intensity as a function of q_z for Cd^{2+} L_α signal with corresponding ion concentration profile and (e) Fluorescence intensity as a function of q_z for Ca^{2+} K_α signal

The obtained thickness is smaller than the control, $28.2 \pm 12.0 \text{ \AA}$ and Ca^{2+} condition, $27.9 \pm 9.4 \text{ \AA}$. Further, the SLD remained the same, $(9.6 \pm 0.1) \times 10^{-6} \text{ \AA}^{-2}$. Here, the ion concentration of Cd^{2+} in the monolayer has its maximum at a concentration of 0.03 M at $z_{\text{max}(\text{Cd}^{2+})} = 39.7 \text{ \AA}$ from air/chain interface. When comparing these results with the previous condition (subphase containing only 1 mM Cd^{2+}), a decrease by a factor of 1.6 is observed. The calculated lateral density of Cd^{2+} ions was determined to be $c_{\text{L}(\text{Cd}^{2+})} = 0.76 \times 10^{13} \text{ ions/cm}^2$ which corresponds to $N = 5$ for $A = 132 \text{ \AA}^2$ at 20 mN/m . In contrast to the previous sample condition, where only Cd^{2+} was added to the subphase, only half the amount of Cd^{2+} ions are bound to the polymer brush. This can be explained by the presence of Ca^{2+} , which accumulates weakly and occupies sites within the polymer brush. This limits the specific binding of Cd^{2+} ions, resulting in low concentration. Here, also no Ca^{2+} ion enrichment below the critical angle could be observed (Figure 4.9e).

The overall SLD and roughness of the pAA-Cys5 polymer brush layer do not change significantly in the presence of divalent cations. Only the sample containing Cd^{2+} ions in the subphase shows slightly higher compaction. When examining the thickness changes (compaction and swelling) in the systems with M^{2+} , these changes are primarily observed as height variations, while the overall SLD profile and interfacial roughness remain unchanged. These findings can also be linked to the high polydispersity index (PDI) of 1.7 (see section 3.1.10). Here, stronger interactions occur due to the increased ion exposure of longer chains, whereas the broad PDI produces a natural density gradient, implying a range of chain lengths. As a result, the intrinsic roughness becomes smoother and less susceptible to ionic interactions. This assumption is supported by the findings of Hildebrandt et al., who studied the intrinsic roughness within spin-coated polymer films and polymer brushes as well as multilayers of both systems using AFM, ellipsometry, XRR, and Grazing Incidence Small-Angle X-ray Scattering (GISAXS). They analyzed the interfacial properties of the systems. They found that spin-coated polymers lose their roughness properties in processes such as solvent vapor annealing, which is more prone to external influences. In contrast, the roughness of polymer brush systems can be seen as an intrinsic property of the brush itself [112].

4 ION-SPECIFIC RECOGNITION ON THE MEMBRANE SURFACE

Table 4: Thickness d , scattering length density (SLD) and roughness (σ)

	Thickness[Å]	SLD [10^{-6}Å^{-2}]	Roughness [Å]
DOPC/PE-pAA-Cys5 (Ctrl)			
Alkyl chain	11.4 ± 0.3	7.5 ± 0.8	3.4 ± 0.2
Headgroup	7.8 ± 0.4	11.7 ± 0.1	4.5 ± 0.8
pAA-Cys5	28.2 ± 12.0	9.6 ± 0.1	3.1 ± 0.1
Buffer	–	9.5	9.3 ± 1.4
Addition of 1 mM Cd²⁺			
Alkyl chain	10.3 ± 0.1	8.5 ± 0.3	3.5 ± 0.1
Headgroup	7.9 ± 0.3	11.9 ± 0.1	3.6 ± 0.3
pAA-Cys5	20.7 ± 12.1	9.7 ± 0.1	3.1 ± 0.1
Buffer	–	9.5	9.2 ± 1.4
Addition of 1 mM Ca²⁺			
Alkyl chain	11.2 ± 0.2	7.5 ± 0.5	3.2 ± 0.1
Headgroup	7.4 ± 0.3	11.8 ± 0.2	5.0 ± 0.5
pAA-Cys5	27.9 ± 9.4	9.6 ± 0.1	3.1 ± 0.1
Buffer	–	9.5	8.9 ± 2.2
Addition of 1 mM Cd²⁺ + 1 mM Ca²⁺			
Alkyl chain	10.7 ± 0.3	7.2 ± 0.5	3.3 ± 0.1
Headgroup	7.8 ± 0.5	11.8 ± 0.1	4.7 ± 0.6
pAA-Cys5	24.1 ± 7.9	9.6 ± 0.1	3.1 ± 0.1
Buffer	–	9.5	8.7 ± 1.5

5 Structural Characterization of Native Biomembranes

5.1 Structural and Spectroscopic characterization of supported Sarcoplasmic Reticulum (SR) Membranes on solid substrates

In this section, SR membranes (extracted from the rabbit muscle) are characterized on native oxide-coated Si substrates, where the structures in the direction perpendicular to the membrane plane are studied by high energy specular X-ray reflectivity (XRR) and confirmed by complementary specular neutron reflectivity (NR) experiments in D₂O. To further investigate the enzymatic degradation of the SR membrane and the associated molecular and spectroscopic changes, attenuated total reflection Fourier transform infrared (ATR-FTIR) spectroscopy, X-ray reflectometry (XRR) and neutron reflectometry (NR) were employed. Enzymatic degradation involved treating the membrane with a buffer containing chymotrypsin for 15 h, a serine endoproteinase that explicitly cleaves peptide bonds at the C-terminus of Tyr, Phe, Trp and Leu [18]. This part of the experiment was performed in collaboration with Christian Busch, group of Prof. Dr. Reiner Dahint (PCI, Heidelberg University). In addition, the obtained spectral ellipsometry data were measured by Andreas Stöcklin.

5.1.1 Immunofluorescence staining and SDS-PAGE of SR membrane

The protein content and homogeneity of the deposited membrane were investigated. The protein composition of the purified SR membranes was determined by Sodium Dodecyl Sulfate Polyacrylamide Gel Electrophoresis (SDS-PAGE) [100]. In Figure 5.1a, the most prominent band was quantitatively characterized by the strong blue color of Coomassie blue staining. Ca²⁺-ATPase, with a molecular weight of 105 kDa, was identified as the most prominent band. The lipid concentration was determined by Fiske and Subbarow colorimetric assay [113], with a concentration of 13 mg/mL, while the protein concentration determined by Bradford assay [98] was 12 mg/ml. These findings agree with the composition of plasma membranes consisting of roughly equal-weight lipids and proteins. This results in a molar ratio of lipids to proteins of approximately 50:1 to 100:1 [114].

Assuming an average molecular weight of lipids of 800 Da and that 60% of total membrane proteins are Ca^{2+} -ATPase, the calculated molar ratio of lipids to Ca^{2+} -ATPase is 235:1. The SR membrane was then deposited on a glass cover substrate and imaged by fluorescence microscopy (see Figure 5.1b).

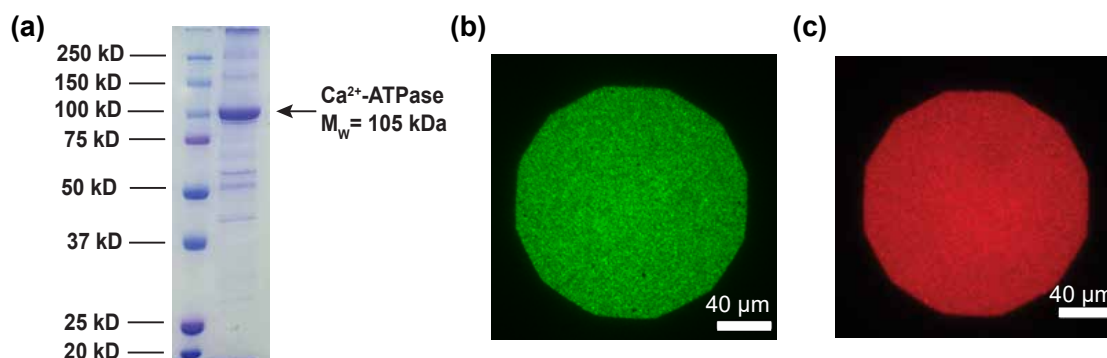


Figure 5.1: (a) SDS-PAGE of SR membranes stained with Coomassie blue shows the following: lane 1 displays the molecular weight standard and lane 2 contains SR membranes in free suspensions. The band of Ca^{2+} -ATPase ($M_w = 105$ kDa) is marked by an arrow. (b) Immunofluorescence microscopy image of SR membranes on a glass substrate, labeled with anti- Ca^{2+} -ATPase. (c) Fluorescence microscopy image of supported lipid-labeled SR membrane on a glass substrate, doped with 0.2 mol% TexasRed DHPE.

By immunofluorescence staining, the C-terminal domain of the Ca^{2+} -ATPase was first labeled with a monoclonal antibody recognizing SERCA2-ATPase, followed by a secondary polyclonal Alexa Fluor 488 goat anti-mouse IgG. The immunofluorescence signal reveals a very uniform coated surface. This is consistent with previous findings [7] [115] [8]. Furthermore, the lipid membrane was labeled by incorporating 0.2 mol % TexasRed DHPE. No significant defects or aggregation of the membrane components were observed. These findings confirm that the SR membranes are uniformly distributed on the planar substrate, with Ca^{2+} -ATPase evenly dispersed across the surface.

5.1.2 Structural Analysis of Supported SR Membranes Using XRR and NR

Before the structural characterization of the SR membrane by XRR and NR, the SR membrane was deposited on a silicon wafer, and the spectral data were measured using an M44 ellipsometer (J.A. Woollam Co., Inc., USA). The obtained data were then fitted using

5.1 Structural and Spectroscopic characterization of supported Sarcoplasmic Reticulum (SR) Membranes on solid substrates

the following Cauchy model [116] [117]:

$$n(\lambda) = A + \frac{B}{\lambda^2} \quad (55)$$

Where $n(\lambda)$ is the refractive index, λ the wavelength in μm , and A, B are the fitting parameters, known as Cauchy parameters. The best-fit values obtained are $A = 1.70 \pm 0.08$ RIU and $B = 0.05 \pm 0.02 \mu\text{m}^2$. These values are in good agreement with those reported for dry lipid films, where $A = 1.64 \pm 0.14$ RIU [118], and the thickness $d_{\text{elli}} = 49 \pm 6 \text{ \AA}$. This measurement showed the formation of a single SR membrane within 1 h, whereby more prolonged incubation led to multilayer/ aggregate formation.

For the analysis of the XRR data obtained from the high-energy X-ray reflectivity measurement at high energy (17.48 eV), a 3-slab model (MOTOFIT) was used to resolve the fine structure of the SR membrane at the solid/liquid interface. Figure 5.2a represents the XRR curve (symbols) and the best-fit results according to χ^2 minimization (black solid line) of the SR membrane after incubation for 1 h and measured in buffer, respectively. Here, slabs 1 and 3 represent the inner and outer hydrophilic head groups and the membrane domains of proteins, while slab 2 is the hydrophobic core with the transmembrane proteins. With this analysis, the thickness d , roughness (σ), and the scattering length density (SLD) is determined (obtained parameters are summarized in Table 5). The scattering length density reconstructed from the best fit of the experimental data is shown in Figure 5.2b.

The fit of the data resulted in an overall thickness of 44 \AA thick SR membrane, with a small roughness value of $3\text{-}5 \text{ \AA}$ at all interfaces, indicating a smooth membrane layer formation on the silicon substrate.

Further, it was found that the SLD value of the hydrophobic chain layer, $(9.2 \pm 0.09) \times 10^{-6} \text{ \AA}^{-2}$ is larger compared to a pure phospholipid membrane with no proteins, $(7.0 \pm 0.2) \times 10^{-6} \text{ \AA}^{-2}$ [9]. This can be explained by the penetration of water molecules into the hydrophobic layer of the chain. This leads to a disorientation of the hydrophobic chain of protein transmembrane helices. Considering the thickness variation of the hydrophobic core with that of a pure lipid membrane, it can be seen that the errors

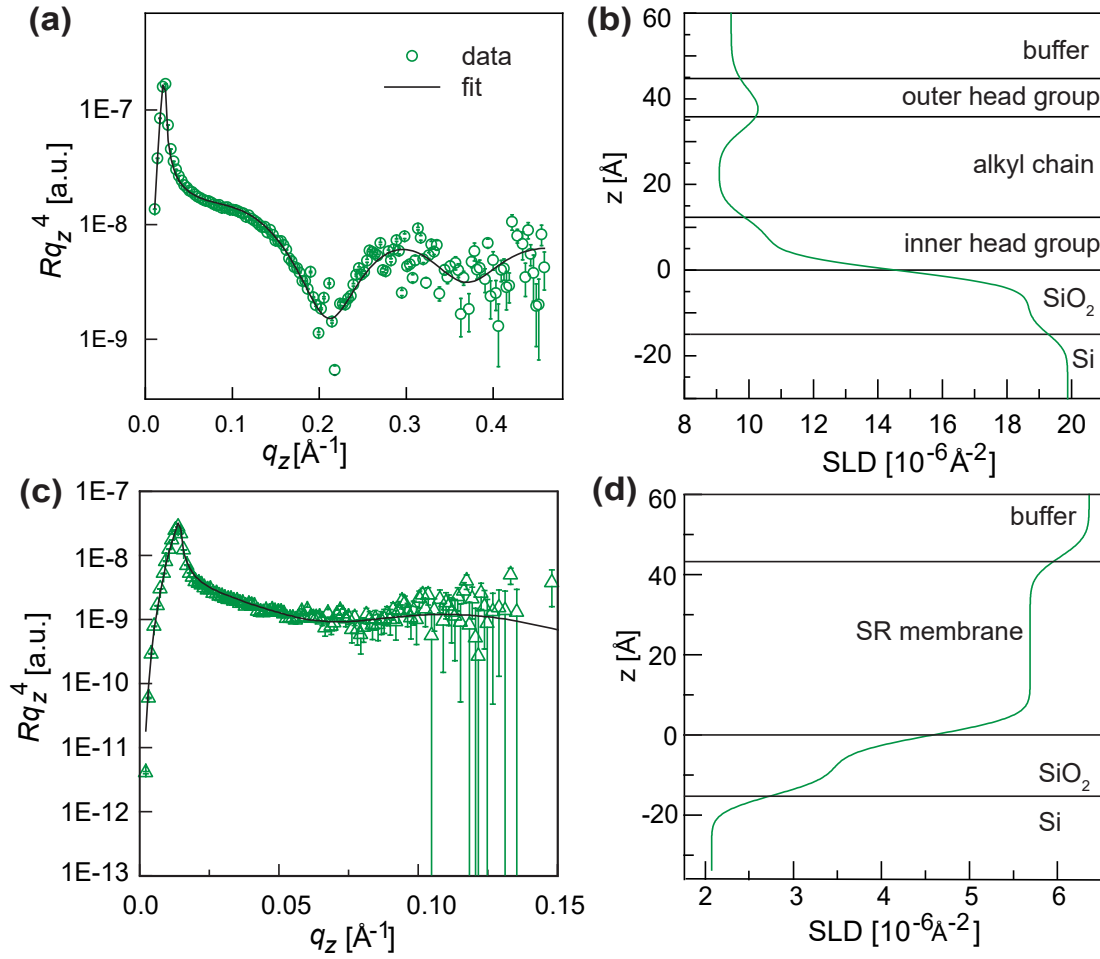


Figure 5.2: X-ray reflectivity data (symbol) and best-fit results (black solid line) of (a) Sarcoplasmic reticulum on a silicon substrate and (b) SLD profile along the z -axis, (c) and (d) Neutron reflectivity data (symbol) and best-fit results (black solid line), SLD profile.

are minor $\Delta d = 1.4 \text{ \AA}$ and can be neglected [9]. Compared to a pure phospholipid membrane, the hydrophilic layers 1 and 3, which are a combination of lipid head groups and extramembrane protein domains, showed a greater thickness and a lower SLD. This can be explained by the less densely packed extramembrane protein domains contained in the system that distinguish the layers.

To confirm the findings discussed above, further neutron reflectivity measurements were performed on a silicon block ($80 \times 50 \text{ mm}^2$) coated with an SR membrane in Grenoble, France. The SR membrane layer is highlighted by the increased contrast obtained by the use of isotopes in D_2O compared to the hydrogenated system. The SR membrane

5.1 Structural and Spectroscopic characterization of supported Sarcoplasmic Reticulum (SR) Membranes on solid substrates

Table 5: Thickness, SLD, and roughness of a supported SR membrane determined by XRR measurement

XRR/NR	thickness [Å]	SLD [10^{-6}Å^{-2}]	roughness [Å]
Slab 1	12.3 ± 0.4	10.6 ± 0.07	4.0 ± 0.4
Slab 2	23.5 ± 0.2	9.2 ± 0.09	3.2 ± 0.1
Slab 3	8.9 ± 1.1	11.3 ± 0.07	4.9 ± 0.07
SiO ₂	15	18.7	3.1 ± 0.1
Si	–	19.8	3.1 ± 0.1
Slab A	44.9 ± 0.1	5.7 ± 0.0	3.6 ± 0.3

was treated as one slab (slab A, Table 5) due to the small q_z range where the statistic count was limited to $q_z = 0.13 \text{Å}^{-1}$ [15]. From the best fit according to the χ^2 of 0.01 a thickness of $44.9 \pm 0.1 \text{Å}$ was obtained. This obtained thickness is in good agreement with the XRR results obtained. The low roughness of the SR membrane ($\sigma = 3.9 \text{Å}$) further confirms the membrane's quality. When comparing the sizes of the substrates used for the two different measurements, the NR Si block ($80 \times 50 \text{mm}^2$) and the small Si substrate for XRR ($24.5 \times 13 \text{mm}^2$), it is evident that neither the size of the substrate nor the beam footprint impacts the quality obtained in the measurements. Analyzing the native protein-rich membrane with XRR poses challenges in evaluating the SLD values, particularly due to uncertainty about the amount of water present in Ca²⁺-ATPase and other proteins.

5.1.3 Characterization of supported SR membranes after enzymatic degradation using XRR and NR

The following experiment was carried out to investigate the proteolytic digestion effect on the SR membrane. For this purpose, 0.005 U/mL of chymotrypsin was added to the SR membrane and incubated for 15 h. Figure 5.3a shows the best fit (solid black line) according to the χ^2 minimization of the supported SR membrane after 15 h of chymotrypsin digestion. In this experiment, the same 3 slabs have been defined (slab B NR, Table 6). By comparing the data of the SR membrane before treatment, it can be seen that digestion alters the characteristics of the XRR curve.

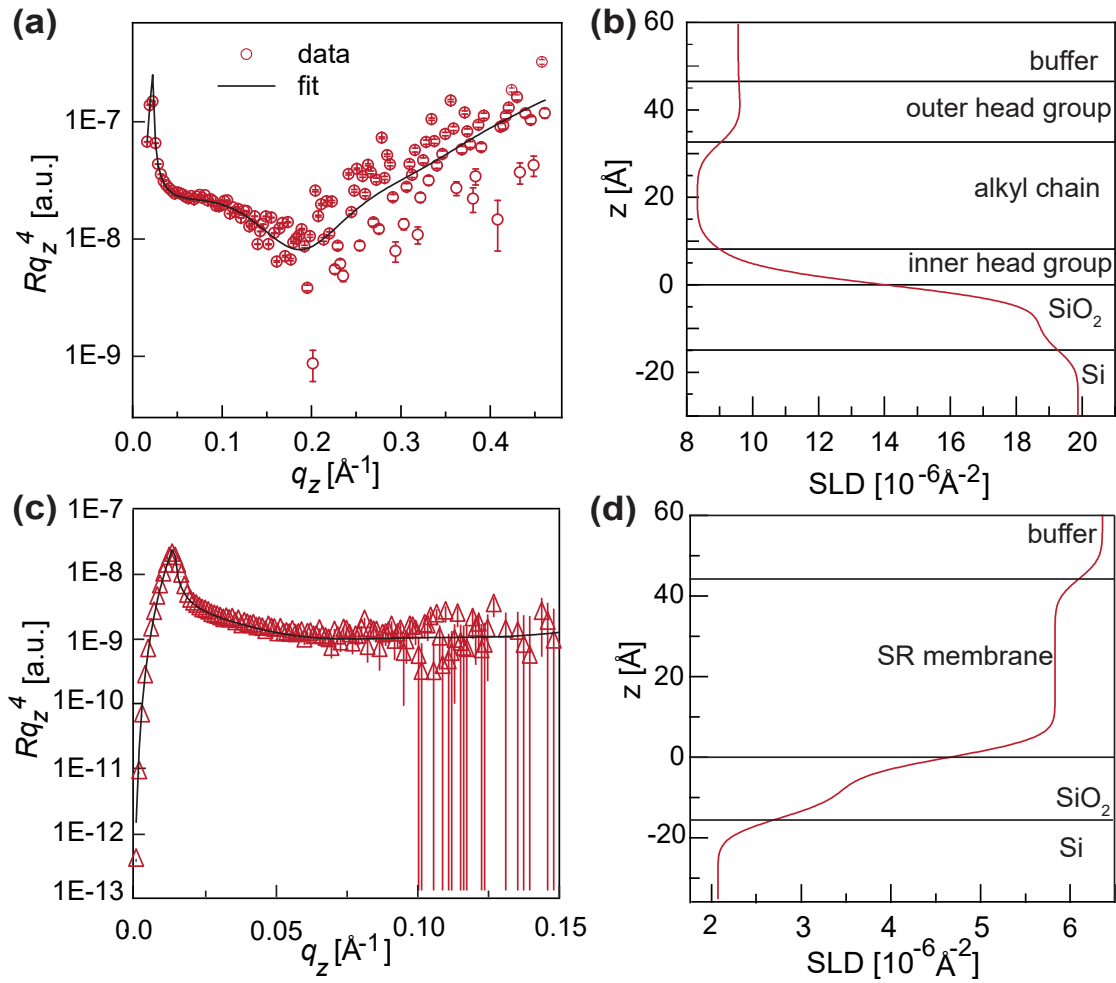


Figure 5.3: X-ray reflectivity data (symbol) and best-fit results (black solid line) of (a) Sarcoplasmic reticulum on a silicon substrate and (b) SLD profile along the z -axis, (c) and (d) neutron reflectivity data (symbol) and best-fit results (black solid line), SLD profile.

The pronounced maximum at 0.3 , $q_z = 0.13 \text{ \AA}^{-1}$ is flattened. This indicates a change in the structural composition of the SR membrane. The thickness of the hydrophilic layers, including the lipid head groups and the protein's extra-membrane domain, showed a reduction of approximately $\Delta d \approx 3 \text{ \AA}$. The decrease can be due to the degradation of a small part of the extra membrane protein domains. The slight thickness increase in the membrane was too small compared to the size of the extracellular domains of Ca^{2+} -ATPase [119]. Moreover, a slight increase in the thickness of the hydrophobic layer and a decrease

5.1 Structural and Spectroscopic characterization of supported Sarcoplasmic Reticulum (SR) Membranes on solid substrates

in the SLD may be related to the compaction of the extra-membrane domain as a result of the degradation process. In general, the roughness of all layers increased slightly over time. The same experiment was repeated for neutron reflectivity measurements. After the digestion process, no difference in the structure of the SR membrane was observed. The roughness, SLD, and thickness remained the same. This can be explained by the fact that the range q_z ($\leq 0.13 \text{ \AA}^{-1}$) is narrower than X-ray reflectivity measurements.

Table 6: Thickness, SLD, and roughness of a supported SR membrane after enzymatic digestion as determined by XRR/NR measurement

XRR/NR	thickness [Å]	SLD [10^{-6} \AA^{-2}]	roughness [Å]
Slab 1	9.5 ± 1.8	10.2 ± 0.3	4.7 ± 1.1
Slab 2	25.1 ± 1.3	8.1 ± 0.2	4.4 ± 0.9
Slab 3	8.2 ± 0.9	10.0 ± 0.4	5.2 ± 0.9
SiO ₂	15	18.7	3.1 ± 0.1
Si	–	19.8	3.7 ± 0.1
Slab B	44.2 ± 1.3	5.8 ± 0.0	3.5 ± 0.3

5.1.4 In situ Monitoring of Proteolytic Digestion by ATR-FTIR

In this experiment, ATR-FTIR is used to analyze the enzymatic degradation of the SR membrane by chymotrypsin, with measurements performed using a Nicolet iG50 Fourier-transform IR spectrometer (Thermo Fisher Scientific, Dreieich, Germany). The spectra were taken over a range of $\nu = 1200\text{-}4000 \text{ cm}^{-1}$ with a resolution of $\Delta \nu = \pm 0.24 \text{ cm}^{-1}$. Figure 5.4a represents the FTIR spectrum of the supported SR membrane, the absorbance plotted against the wavenumber ν . The SR membrane can be characterized by two distinct sets of peaks (spectra at time point 0). The first set consists of the symmetric and asymmetric CH₂ stretching bands at $\nu \approx 2850$ and 2920 cm^{-1} , which are found in both proteins and lipids. The second set of peaks that arises from proteins is the Amide I and II found at $\nu \approx 1650 \text{ cm}^{-1}$ and $\nu \approx 1600\text{-}1500 \text{ cm}^{-1}$ [120] [121] [122]. Further, the strong amide I peak implies the contribution of the α -helices ($\nu \approx 1650 \text{ cm}^{-1}$). This observation aligns well with the structural design of the Ca²⁺-ATPase containing 10 α -helices [119] [123]. The SR membrane was incubated with a chymotrypsin solution (0.005 U/mL) and monitored over 15 h (see Figure 5.4a).

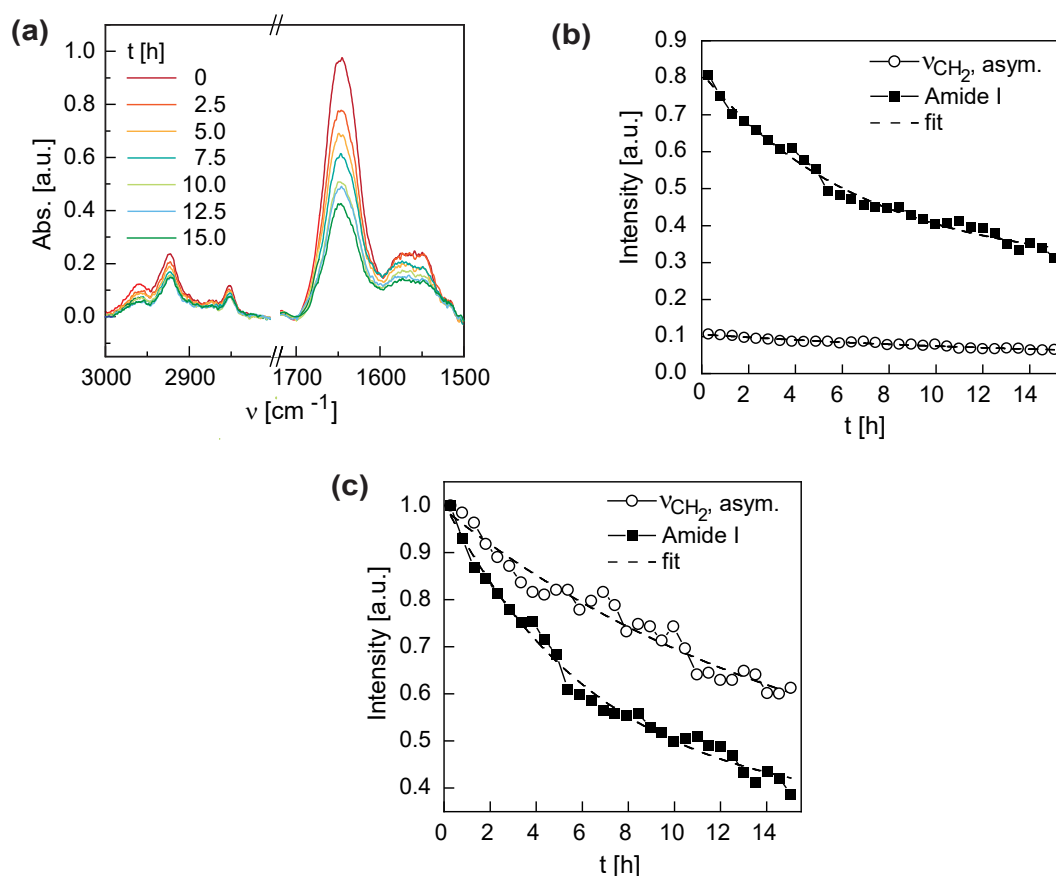


Figure 5.4: (a) ATR-FTIR spectra of a supported SR membrane treated chymotrypsin over 15 h (color code indicates change over time) (b) Intensity vs. time for the protein peak (amide I band, $\nu \approx 1650 \text{ cm}^{-1}$) and lipids (asymmetric CH_2 stretching band, $\nu \approx 2920 \text{ cm}^{-1}$). A binning factor of 10 has been applied to the data. (c) Variation of relative peak intensities over time, as shown in panel (b).

Incubation with chymotrypsin resulted in a continuous decrease in the intensity of the amide I and amide II bands ($\nu \approx 1650 - 1500 \text{ cm}^{-1}$). The decrease in amide I indicates that the proteins in the SR membrane have undergone proteolytic digestion. The data analysis of the amide II peak was more difficult due to the small peak height and overall low intensity. In addition, a prominent peak at about 1450 cm^{-1} made baseline correction and, thus, accurate peak intensity determination difficult. In Figure 5.4b, the peak intensity of the amide I band ($\nu \approx 1650 \text{ cm}^{-1}$) and the asymmetric CH_2 stretching band ($\nu \approx 2920 \text{ cm}^{-1}$) are plotted against time. The amide I peak (solid squares) decreases sharply with time, whereas the asymmetric CH_2 band (open circles) shows only a slight decrease. Even after 15 h the

5.1 Structural and Spectroscopic characterization of supported Sarcoplasmic Reticulum (SR) Membranes on solid substrates

amide I peak does not reach a steady state. This behavior agrees with previous reports, indicating that proteolytic digestion by chymotrypsin is thermodynamically advantageous but proceeds at a slow rate [124] [125]. Figure 5.4c shows the relative intensity decrease over time for both peak positions. In this Figure, the difference in the peak intensity in the amide I and CH₂ bands becomes more clearly visible. The amide I peak shows a steeper decrease than the CH₂ band. Here, CH₂ bands are derived from lipids and proteins, whereas the amide I bands are derived from proteins only. With this understanding, it can be said that chymotrypsin predominantly digests proteins. An exponential fit of the data shows that the decay time of amide I is 2.4 times shorter than that of the asymmetric CH₂ band. Considering 35% of the initial values of the final band intensities suggests incomplete digestion of membrane proteins relative to the amount of enzyme used [18].

5.2 Fine-structure characterization of polymer-supported healthy and infected ghost cell membrane by Neutron Reflectivity

In this section, neutron reflectivity (NR) is utilized to study the fine structure of healthy erythrocyte ghost membranes and *Plasmodium falciparum*-infected erythrocyte ghost membranes deposited on cellulose (TMSC) cushion [3] (Figure 1.6).

5.2.1 Preanalysis of polymer support and erythrocyte ghost membrane

Prior to the structural analysis of the polymer-supported erythrocyte ghost membrane/infected erythrocyte ghost membrane by neutron reflectivity, a preliminary analysis of the sample quality was carried out. As a first step, the quality of the spin-coated trimethyl-substituted cellulose (TMSC) and the HCl vapor-regenerated cellulose (see 3.1.5) was evaluated using contact angle measurements, ellipsometry, and atomic force microscopy (AFM).

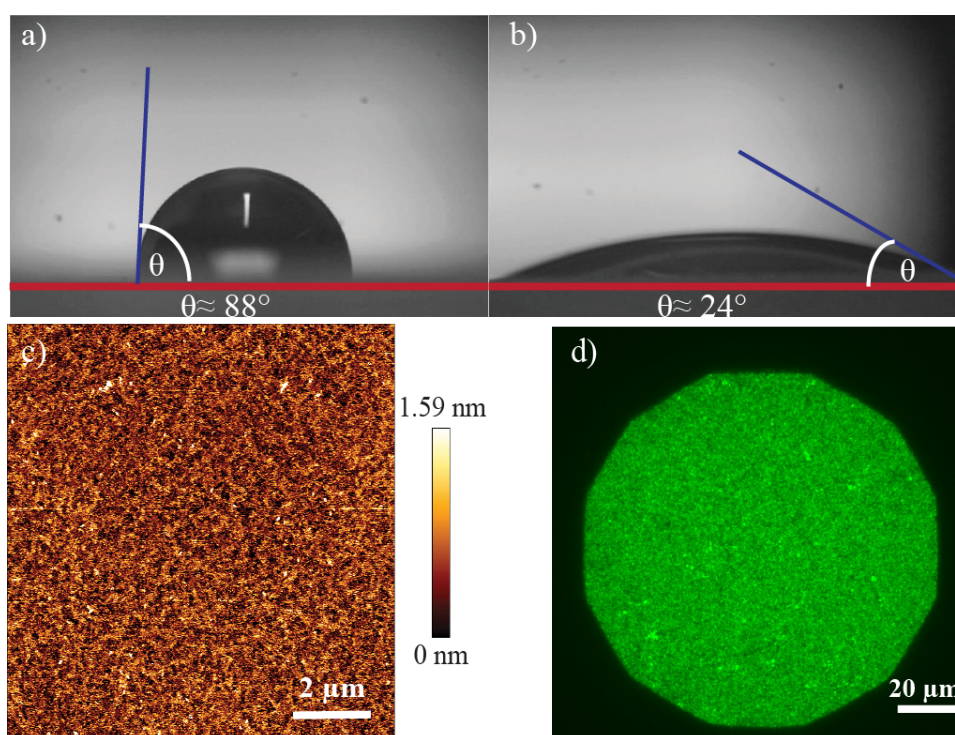


Figure 5.5: Contact angle measurement on TMSC (a) before and (b) after regeneration with HCl. (c) Tapping-AFM image of cellulose after regeneration on air, scan size: 10x10 μm (d) Band 3 immunofluorescence image of healthy erythrocyte ghost membrane on optimized cellulose.

5.2 Fine-structure characterization of polymer-supported healthy and infected ghost cell membrane by Neutron Reflectivity

The contact angle was measured after the deposition of TMSC by spin coating on a clean silicon wafer (Figure 5.5a) and after exposure to hydrochloric acid (HCl) vapor (Figure 5.5b). Prior to regeneration, a water contact angle of 88° was determined. This contact angle decreases (indicating that the surface became hydrophilic) to 24° due to hydrolytic cleavage of the trimethyl side chain when TMSC was exposed to HCl vapor (see Figure 5.5) [126]. The film thickness was subsequently measured using ellipsometry. The refractive indices used were set to $n = 1.404$ (before regeneration, for TMSC) and $n = 1.505$ (after regeneration). The obtained thickness of the film in its dry state was $d = 151.0 \pm 2.5 \text{ \AA}$, which decreased to $d = 53.0 \pm 4.0 \text{ \AA}$ after regeneration. The surface topography of the cellulose-coated substrate in its dry state was analyzed using AFM with a scanning area of $10 \times 10 \text{ \mu m}$. The height deviation from the top to the bottom remained at $<2 \text{ nm}$. The root mean square (RMS) roughness of the cellulose film after hydration remained in the range of $3\text{-}4 \text{ \AA}$ (measured at different scan areas). This confirms the uniformly coated substrate. The low standard deviation of the thickness taken with the ellipsometer further supports this conclusion. These results confirm the uniformity of the regenerated cellulose film from both a thickness and topographic point of view.

Immunofluorescence measurements (Figure 5.5d) confirmed the homogenous formation of the erythrocyte ghost membrane on the polymer support. The homogenous membrane coating was evaluated after incubating for 1 h with the anti-band 3 antibody conjugated Alexa Fluor 488 (mouse monoclonal). A uniform fluorescence signal was obtained on the cellulose support originating from the cytoplasmic domain of Band 3, indicating a continuous coating of the erythrocyte ghost membrane. It is known that the cellulose support prevents direct contact between the membrane and the substrate, thus avoiding the denaturation of membrane proteins and creating a hydrophilic platform that allows homogenous rupture of the vesicle and coating of the surface [3].

5.2.2 Cellulose characterization in dry and hydrated state

Figure 5.6a, c show the NR curves (symbols) of the dry cellulose in ambient atmosphere, along with the best-fit results according to χ^2 minimization (black solid line). The healthy

and infected erythrocyte cell membranes were deposited on two independent spin-coated cellulose samples on silicon blocks, samples A and B, respectively (see section 5.2.3). The dry cellulose films/hydrated films were prepared under the same conditions. The NR fit of dry cellulose resulted in a thickness of $177.8 \pm 0.9 \text{ \AA}$ and roughness of $3.8 \pm 0.5 \text{ \AA}$ for sample A and a thickness of $180.3 \pm 0.3 \text{ \AA}$ and roughness of $8.1 \pm 0.1 \text{ \AA}$ for sample B. It can be seen that the roughness of the dry cellulose remains low even when spin-coated on a larger silicon block.

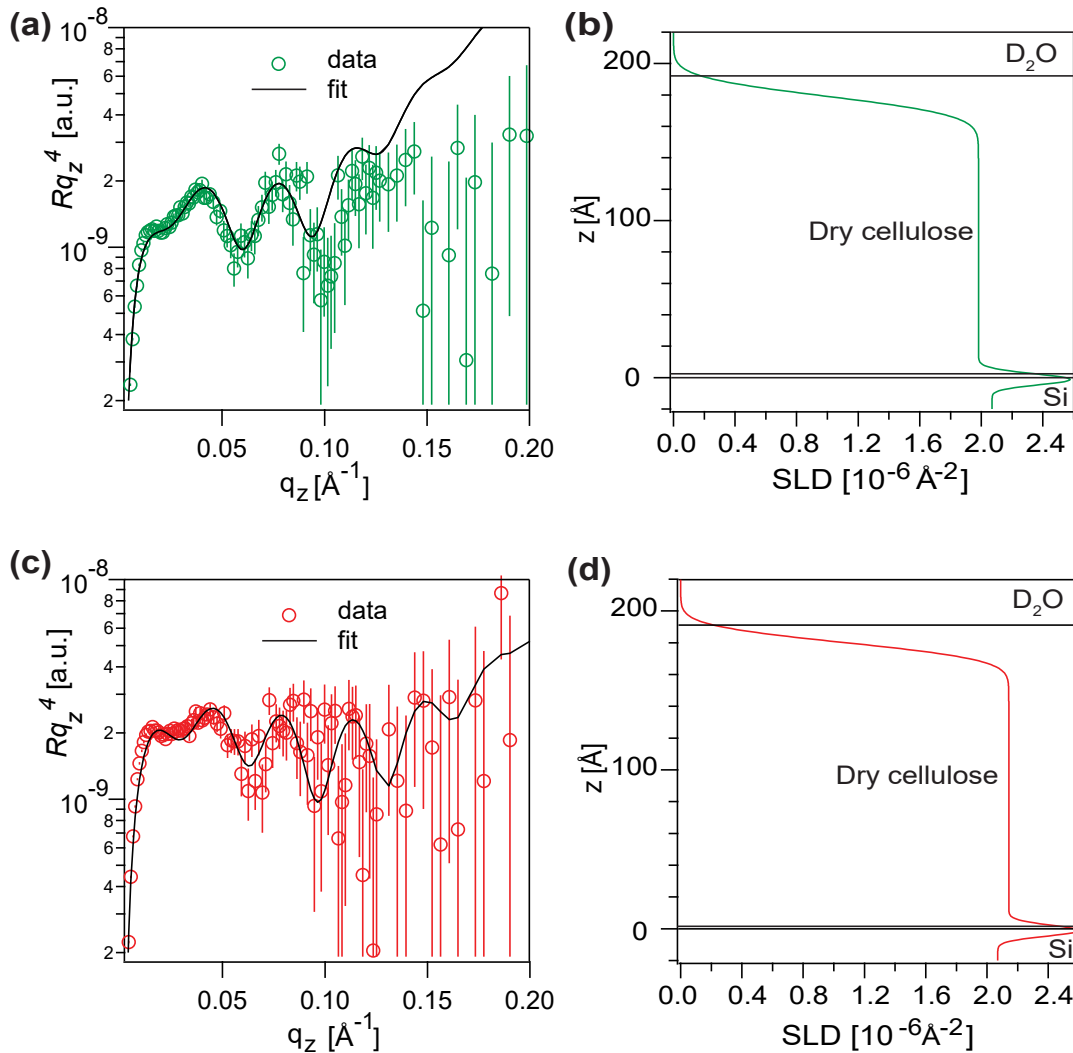


Figure 5.6: NR data of dry cellulose with corresponding SLD profile, (a)+(b) Sample A and (c)+(d) Sample B

5.2 Fine-structure characterization of polymer-supported healthy and infected ghost cell membrane by Neutron Reflectivity

Table 7: Thickness, SLD, and roughness of **dry cellulose** (Sample A, for healthy erythrocyte ghost system)

	Thickness [Å]	SLD [10^{-6}Å^{-2}]	Roughness [Å]
Air	–	–	–
Dry Cellulose	177.8 ± 0.9	2.0 ± 0.01	3.8 ± 0.5
SiO ₂	3.4 ± 0.2	3.5	4.0 ± 0.6
Si	–	2.1	9.7 ± 0.2

Table 8: Thickness, SLD, and roughness of **dry cellulose** (Sample B, for infected erythrocyte ghost system)

	Thickness [Å]	SLD [10^{-6}Å^{-2}]	Roughness [Å]
Air	–	–	–
Dry Cellulose	180.3 ± 0.3	2.1 ± 0.01	8.1 ± 0.1
SiO ₂	3.1 ± 0.1	3.5	3.8 ± 0.1
Si	–	2.1	3.2 ± 0.2

To study the hydration thickness of the cellulose layer, samples were hydrated for approximately 2 hours prior to measurement. Two slabs were defined to model the hydrated cellulose film. The cellulose film was considered to consist of a poorly hydrated layer and a fully hydrated layer. To enhance the contrast, H₂O was replaced with D₂O for the neutron reflectometry (NR) measurements. The transition from dry to hydrated cellulose state can be clearly observed by changes such as decreased fringes and flattening of the fitted data (see Figure 5.6 to Figure 5.7). The combined thickness of the hydrated cellulose layers was measured to be 260 Å for sample A and 264 Å for sample B, corresponding to a swelling factor of 1.4. This swelling behavior is relatively limited compared to previously reported data [15] [126]. This limitation may be due to an incomplete regeneration of the trimethylsilyl cellulose (TMSC) when exposed to HCl. The SLD values differ slightly, with sample A showing a value of $5.2 \times 10^{-6} \text{Å}^{-2}$ and sample B, $5.4 \times 10^{-6} \text{Å}^{-2}$. This indicates a slightly more compacted cellulose layer in the infected sample. In terms of roughness, both samples exhibit high roughness in the hydrated cellulose/D₂O interface. This diffuse interface can be caused by uneven polymer swelling. This finding agrees with research done by Rossetti et al.(2015) [15], who attributed these characteristics to the uneven hydration and density transitions within swollen polymer supports.

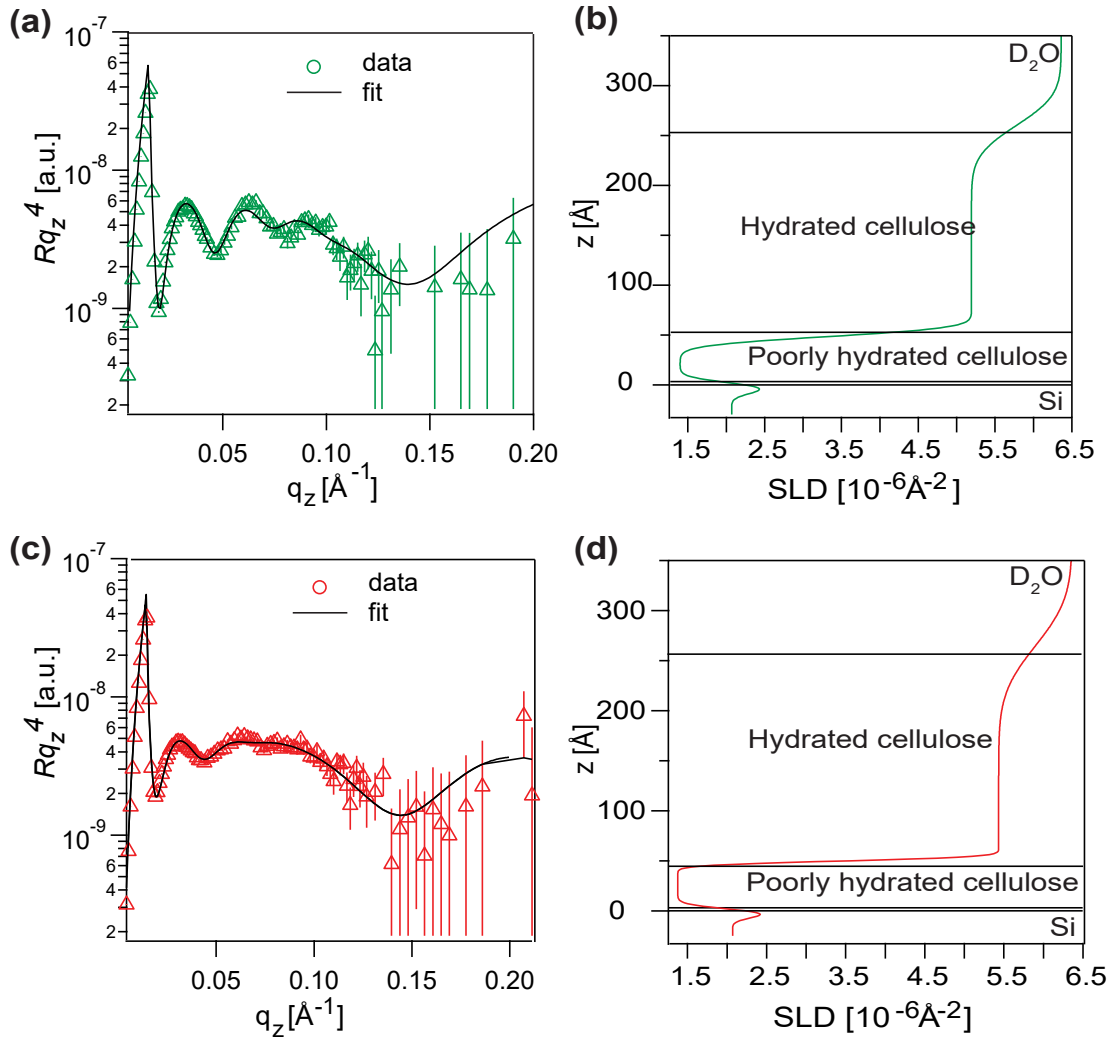


Figure 5.7: NR data of hydrated cellulose along with corresponding SLD profile, (a)+(b) Sample A and (c)+(d) Sample B

Table 9: Thickness, SLD, and roughness of **hydrated cellulose** (Sample A, for healthy erythrocyte ghost system)

	Thickness [Å]	SLD [10^{-6}Å^{-2}]	Roughness [Å]
D ₂ O	–	6.36	–
hydrated cellulose	212.3 ± 0.7	5.2 ± 0.01	23.5 ± 0.7
Poorly hydrated cellulose	47.5 ± 1.1	1.4 ± 0.03	7.3 ± 0.5
SiO ₂	5.6 ± 0.4	3.5	5.9 ± 0.7
Si	–	2.1	4.6 ± 0.7

5.2 Fine-structure characterization of polymer-supported healthy and infected ghost cell membrane by Neutron Reflectivity

Table 10: Thickness, SLD, and roughness of **hydrated cellulose** (Sample B, for infected erythrocyte ghost system)

	Thickness [Å]	SLD [10^{-6}Å^{-2}]	Roughness [Å]
D ₂ O	–	6.36	–
hydrated cellulose	214.9 ± 0.1	5.4 ± 0.01	37.2 ± 0.7
Poorly hydrated cellulose	48.8 ± 0.9	1.4 ± 0.01	3.4 ± 0.3
SiO ₂	4.03 ± 0.4	3.5	4.3 ± 0.5
Si	–	2.1	4.0 ± 0.6

5.2.3 Healthy and infected erythrocyte ghost membrane on cellulose

Both types of membranes (healthy, sample A and infected sample B, erythrocyte ghost membranes), Figure 5.8) were deposited onto a hydrated cellulose layer and incubated for a few more hours. The membrane layer was treated as an additional slab. It can be seen that after membrane formation, the thickness of the poorly hydrated layer increases while the SLD values remain unchanged (summarized in Table 11).

The thickness of the hydrated cellulose decreases slightly, while the SLD remains the same. This suggests that the cellulose layer is fully hydrated and has reached its maximum swelling limit. Consequently, the total thickness of the cellulose layer shows a slight increase to 271 Å and 275 Å. For both healthy and infected erythrocyte ghost membranes, the roughness of the hydrated layer decreases significantly after the membrane is deposited. This reduction in surface roughness indicates a defect healing process, as the additional deposited membrane fills defects in the cellulose surface [15]. Further analysis of the erythrocyte ghost membranes showed that the thickness of the healthy erythrocyte ghost membrane was 51 Å, while the malaria-infected erythrocyte ghost membrane had a slight increase in thickness, 53 Å. However, both SLD values remained the same at $5.8 \times 10^{-6}\text{Å}^{-2}$. This slight increase in thickness can be attributed to the *P. falciparum* infection. *P. falciparum* infection causes structural changes in the red blood cell membrane by transferring specific proteins into the membrane. These proteins include Plasmodium falciparum erythrocyte membrane protein 1 (PfEMP1) and knob-associated histidine-rich protein (KAHRP). These proteins contribute to the formation of knobs on the cell surface, which alters the normal biconcave shape of the erythrocyte, increases membrane rigidity,

and reduces its deformability [127] [128].

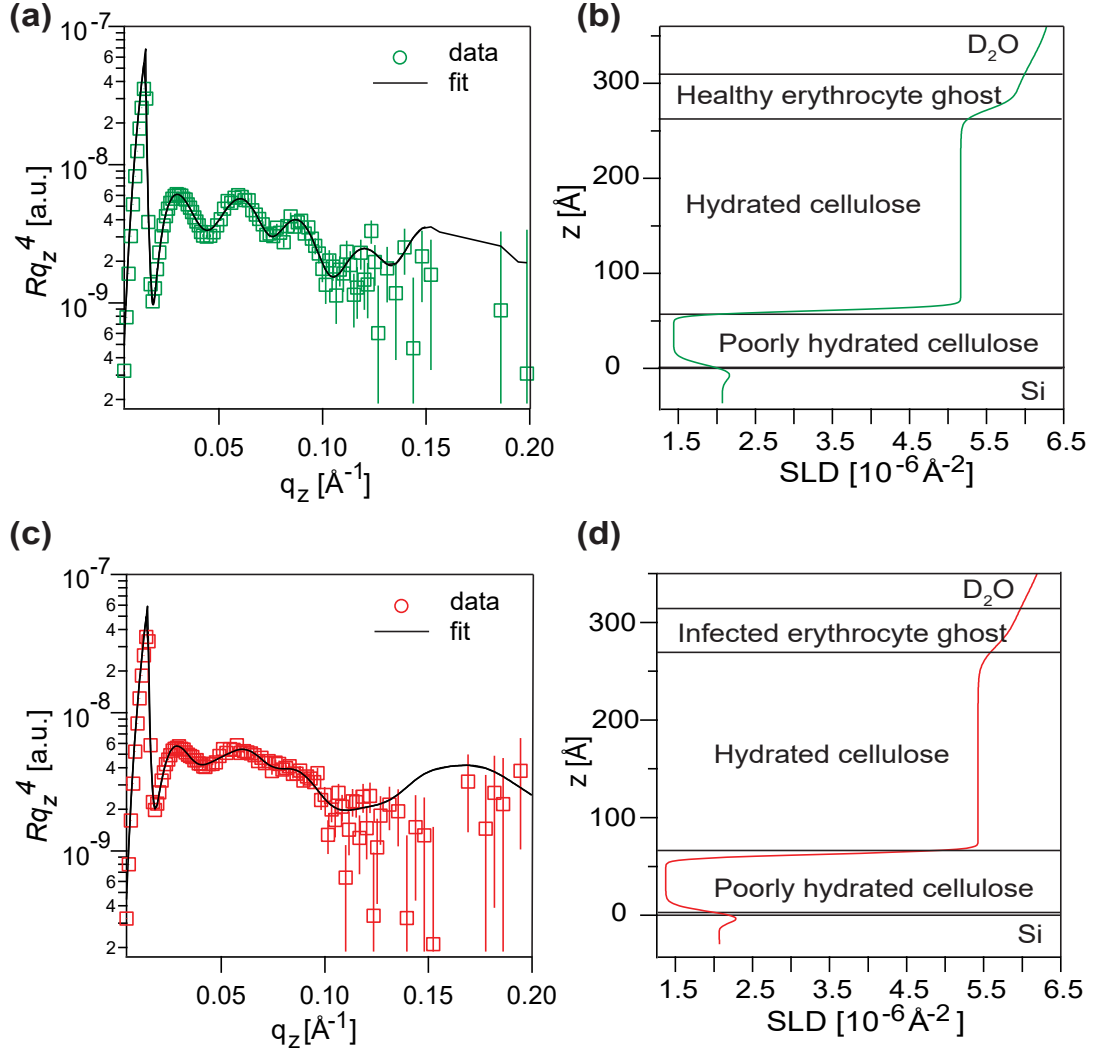


Figure 5.8: (a)+(b) NR data of healthy erythrocyte ghost along with corresponding SLD profile, and (c)+(d) infected erythrocyte ghost with the corresponding SLD profile

However, it should be noted that the large roughness obtained for the D₂O/membrane interface ~ 4 nm is close to the membrane thickness ~ 5 nm, which implies that the slight thickness differences between the healthy and infected erythrocyte ghost membranes are insignificant. Furthermore, local structural features like knobs could not be resolved because of neutron reflectometry's (NR) large beam footprint. Yet, the obtained structural parameters indicate that NR can examine the fine structure of native membranes deposited on polymer supports in both infected and healthy conditions.

5.2 Fine-structure characterization of polymer-supported healthy and infected ghost cell membrane by Neutron Reflectivity

Table 11: Thickness, SLD, and roughness of **healthy and infected erythrocyte ghost membranes**

	Thickness [Å]		SLD [10^{-6}Å^{-2}]		Roughness [Å]	
	Healthy	Infected	Healthy	Infected	Healthy	Infected
D ₂ O	–	–	6.36	6.36	–	–
Erythrocyte Ghost Membrane	50.8 ± 0.4	53.4 ± 0.5	5.8 ± 0.02	5.8 ± 0.01	36.1 ± 0.7	38.3 ± 0.6
Hydrated Cellulose	211.9 ± 0.4	211.9 ± 0.5	5.2 ± 0.01	5.4 ± 0.01	8.3 ± 0.4	14.1 ± 0.2
Poorly Hydrated Cellulose	59.6 ± 1.1	63.4 ± 0.7	1.4 ± 0.01	1.4 ± 0.01	7.2 ± 0.6	3.4 ± 0.3
SiO ₂	3.7 ± 0.5	5.4 ± 0.3	3.5	3.5	7.2 ± 0.6	7.4 ± 0.5
Si	–	–	2.1	2.1	6.7 ± 0.8	4.2 ± 1.0

6 Conclusion

In this thesis, the structure and function of artificial membrane models displaying bio-inspired polymers, as well as two types of native biomembranes, were quantitatively investigated by combining unique physical techniques.

In chapter 4, the specific capture of Cd^{2+} ions by plant-inspired polymer brushes anchored on supported lipid membranes were quantitatively studied by using GaN-based transistor devices and grazing incidence X-ray fluorescence (GIXF) measurements.

In section 4.1, the surface of high electron mobility transistor based on GaN/AlGaIn/GaN heterostructure was functionalized with a supported lipid monolayer displaying plant-inspired polymers (pAA-Cys5) that have a high affinity to Cd^{2+} . The change in surface charge density caused by the binding of Cd^{2+} to pAA-Cys5 modulates the carrier density in two-dimensional electron gas, which can be detected as the change in current-voltage (I-V) characteristics. As pAA-Cys5 is a negatively charged polymer, the experiments were performed in buffers with (buffer 1) and without (buffer 2) 100 mM NaCl (pH 7.4). Upon the addition of 10^{-9} M CdCl_2 in buffer 1, a distinct shift in the I-V curves was observed, with a threshold voltage shift of $\Delta V_{\text{th}} \approx + 55.8 \pm 20.2$ mV. Such a high sensitivity can be attributed to the high affinity of pAA-Cys5 to Cd^{2+} reported previously, $K_D \sim 10^{-9}$ M. From 10^{-5} M to 10^{-2} M, the change in threshold voltage linearly increased with increasing $\log [\text{Cd}^{2+}]$. Notably, the slope, $\Delta V_{\text{th}} \approx 28.0 \pm 3.4$ mV for a 10-fold increase in $[\text{Cd}^{2+}]$, was close to Nernstian behavior for $z = 2$. The selectivity of pAA-Cys5-functionalized device was examined by carrying out the same series of experiments with buffers containing CaCl_2 . Compared to the high sensitivity to Cd^{2+} ions, the pAA-Cys5-functionalized device showed a much lower sensitivity to the change in $[\text{Ca}^{2+}]$, 6.2 ± 0.8 mV for a 10-fold difference in $[\text{Ca}^{2+}]$, reflecting four orders of magnitude larger K_D value to Ca^{2+} . Remarkably, in salt-free buffer 2, the sensor response was poor for both Cd^{2+} and Ca^{2+} ions, which does not follow the prediction of Debye-Hückel theorem. This reduced sensitivity at low ionic strength can be attributed to electrostatic repulsions between pAA-Cys5 polymer chains, which does not allow the collapse of polymer chains. It should also be emphasized that

the treatment with EDTA regenerated the system to its original state, enabling repeated detection of Cd^{2+} and Ca^{2+} ions in aqueous environments.

In section 4.2, a lipid monolayer displaying pAA-Cys5 polymer was deposited at the air/water interface, and the amount and distribution of ions in the vicinity of pAA-Cys5 were precisely quantified by simultaneous X-ray reflectivity (XRR) and grazing incidence X-ray fluorescence (GIXF) measurements at ESRF. As the GIXF analysis of monomolecular films requires the electron density profile, the XRR data were analyzed first. The thickness of pAA-Cys5 brush was $28.2 \pm 12.0 \text{ \AA}$ in the absence of Cd^{2+} . In the presence of Cd^{2+} , the brush thickness decreased to $20.7 \pm 12.1 \text{ \AA}$. This is accompanied by a slight increase in SLD, suggesting the ion-induced chain compaction. The XRR data were used to calculate the illumination profile within the framework of Abelé's matrix formalism. This enables to fit the GIXF signal measured near the critical angle of total reflection. Assuming the area per molecule of pAA-Cys5, $A = 134 \text{ \AA}^2$ at 20 mN/m, the lateral density of Cd^{2+} ions was calculated to be $1.5 \times 10^{13} \text{ ions/cm}^2$, indicating that approx. 10 Cd^{2+} ions bind to one pAA-Cys5 chain. When the subphase contained 1 mM Ca^{2+} , no significant change in thickness, SLD, or fluorescence intensity could be observed. Intriguingly, when the buffer contains both Ca^{2+} and Cd^{2+} , the lateral density of Cd^{2+} in this case was $0.76 \times 10^{13} \text{ ions/cm}^2$, corresponding to $N = 5$ ions bound per pAA-Cys5 chain, suggesting that the binding of Cd^{2+} is screened by the presence of non-interacting Ca^{2+} .

In chapter 5, the structures of rabbit sarcoplasmic reticulum (SR) membranes and human erythrocyte ghosts were characterized using XRR and NR measurement at ILL. In addition, the SR membranes were further analyzed by ATR-FTIR spectroscopy. The immunofluorescence staining of Ca^{2+} -ATPase in SR and band 3 in erythrocyte ghosts showed no signs of defects.

In section 5.1, the SR membrane, purified from the rabbit muscle, was deposited on Si substrates. The molecular weight corresponding to the major protein band, 105 kDa, can be assigned to Ca^{2+} -ATPase. The preparative condition was optimized with aid of SE data, suggesting that $\approx 50 \text{ \AA}$ -thick layer was formed after incubating the SR membrane suspen-

6 CONCLUSION

sion for 1 h. The XRR data could be fitted with three-slab model. The best fit suggested an overall SR membrane thickness of $44.8 \pm 0.5 \text{ \AA}$ that possesses a conformal interfacial roughness ($\sigma = 3 - 5 \text{ \AA}$). NR was measured in D_2O to maximize the scattering length density contrast. The data were fitted with a one-slab model due to limited q_z range. Nevertheless, the total membrane thickness, $44.9 \pm 0.1 \text{ \AA}$, was comparable to the one obtained by XRR, suggesting that the quality of the sample is independent from the sample size (of note: $80 \times 50 \text{ mm}^2$ Si-blocks were used for NR, whereas $24.5 \times 13 \text{ mm}^2$ Si wafer for XRR). The proteolytic degradation of the SR membrane with chymotrypsin was monitored over 15 h by ATR-FTIR. The continuous decrease in the amide I ($\nu \approx 1650 \text{ cm}^{-1}$) and amide II ($\nu \approx 1600\text{-}1500 \text{ cm}^{-1}$) peaks indicated the digestion of proteins in the SR membrane. The comparison of XRR data before and after the protease treatment suggests the decrease in the thickness ($\Delta d \approx 3 \text{ \AA}$) and the SLD of the hydrophilic layers representing the lipid head groups and extracellular domains of proteins.

In section 5.2, healthy and malaria-infected erythrocyte ghost membranes were deposited on Si substrates coated with 15 nm-thick cellulose supports, and the structures in the direction perpendicular to the substrate were analyzed using NR measured in D_2O . After characterizing dry and hydrated cellulose layers, the membranes were deposited. Upon hydration, the cellulose layer thickness increased by a factor of ≈ 1.4 from $177.8 \pm 0.9 - 180.3 \pm 0.3 \text{ \AA}$ to 260 and 264 \AA . The global shape of the NR curves showed a clear change after the deposition of healthy and infected erythrocyte ghost membranes. The best fit result suggested that infected cell membrane has a slightly higher thickness and roughness values compared to those of healthy membranes. Although the local structural change, such as knob formation, could not be detected due to the averaging over a large beam footprint, these results suggested a potential of NR for characterizing cell membranes not only in a health state but also in a diseased state.

In conclusion, the obtained results demonstrated that the combination of unique experimental tools could unravel the structure and function of both artificial and native biomembranes beyond widely used simple lipid bilayer models.

7 Appendix

7.1 Ion sensing eGFP monolayer on HEMT

7.1.1 Introduction

High Electron Mobility Transistors (HEMTs) are electronic components utilized in biosensing applications because of their high electron mobility and sensitivity to surface changes. By functionalizing the surface of HEMT, the specific detection of biomolecular interactions at the solid-liquid interface can be investigated. Their effectiveness has been demonstrated in medical research using proteins or DNA to detect ions, small molecules, and pathogens.[129].

H.H. Lee et al. demonstrated the detection of C-reactive protein (CRP), an inflammatory biomarker, on HEMT through the self-assembled monolayer (SAM) functionalization of the Ni/Au gate surface. The detection was based on the antigen-antibody interaction, which affected the gate surface potential. By varying the concentration of CPR from 10 to 1000 ng/mL, they demonstrated the potential of HEMTs for the sensitive detection of biomarkers in clinical diagnostics[130]. As part of protein binding studies on GaN/HEMT, previous studies by S. Mehlhose investigated the Protein binding to lipid monolayer systems on HEMT substrates. He used Enhanced Green Fluorescent Protein (eGFP), bound to the monolayer via Ni-NTA complex, to monitor binding events using fluorescence and electrochemical signals. In this research, combining eGFP with functionalized surfaces allowed real-time observation of reversible protein binding at the solid-liquid interface, improving biosensing applications' sensitivity and specificity [96].

This study integrates Mehlhose's lipid monolayer-based biofunctionalization concept onto the HEMT substrates and extends the work to investigate ion screening effects. The binding of the protein to the membrane was confirmed, and the salt concentration was varied from 10 mM to 150 mM. The effect on the screening length is investigated by the variation of the ionic strength. This study aims to optimize HEMT-based biosensor platforms to detect molecular interactions with improved sensitivity and specificity.

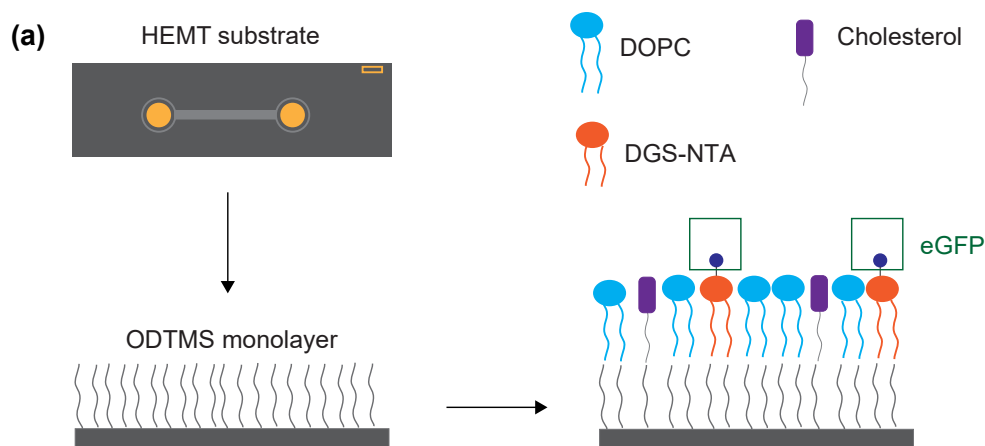


Figure 7.1: (a) HEMT functionalized surface with ODTMS and lipid composition (DOPC:Cholesterol:NTA)

7.1.2 Experimental

6-His-tagged proteins (eGFP): Expression and Purification

Expression

The His-tagged eGFP was inserted into the pQE-31 vector (Qiagen, Netherlands) using specific primers during the ligation process. The recombinant plasmid was then introduced into *Escherichia coli* cells, which were subsequently cultured overnight at 37°C on sterile LB agar plates containing ampicillin. From these, single cells were selected and incubated in 5 mL LB-amp medium overnight at 37°C; 190 rpm. In the next step, 50 mL of LB medium was added to the overnight cell suspension and incubated at 37°C for 1 hour. The optical density (OD) was then measured at a wavelength of 600 nm to estimate the concentration of cells in the liquid culture. The value of OD was 0.6, corresponding to the mid-logarithmic phase of exponential growth. To avoid the formation of inclusion bodies, the IPTG concentration was reduced to 0.1 mM. Cells were incubated at 18 °C for 14 h. Cells were centrifugated for 10 min at 5.000 g at 4°C, and the green pellet was stored at 4°C.

Purification

eGFP was purified using a HisGravi Trap kit (Cytiva, Berlin). In brief, the *Escherichia coli* pellet was resuspended in 2.5 mL binding buffer (20 mM NaH_2PO_4 , 20 mM Imidazol and 500 mM NaCl). For enzymatic/mechanical lysis: 0.2 mg/mL lysozyme, 20 $\mu\text{g/mL}$ DNase, 1 mM MgCl_2 , and 1 mM phenylmethylsulfonyl fluoride (PMSF) was added. After incubated for 30 minutes at room temperature, the solution was sonicated for 10 minutes (mechanical lysis) and centrifuged at 16.000 g (Eppendorf, Germany) for 10 minutes. Supernatant was applied to HisGrav Trap, and eGFP was eluted with ~ 3 mL Imidazol buffer (20 mM sodium phosphate, 0.5 M NaCl, 500 mM imidazole, pH 7.4). The purity of the protein was determined by SDS-Page [100], and the concentration was measured according to Bradford protocol[98].

Substrate coating and transistor settings

For this experiment, the HEMT substrate was coated with ODTMS prior to monolayer deposition (see 3.1.4). The DOPC:cholesterol:NTA, 63:35:2 monolayer was then deposited and incubated in the designed HEMT chamber for 3 h and afterward rinsed with a buffer containing 10 mM HEPES and 10 mM NaCl. Prior to protein deposition, the membrane was intensely saturated with Ni^{2+} buffer (10 mM HEPES, 10 mM NaCl, 2 mM NiCl_2) for 30 min. In the final step, 10 $\mu\text{g/mL}$ eGFP was added and incubated overnight. The I-V curves were measured after each change of the buffer conditions from 10 mM to 150 mM NaCl. The transfer curves were measured at a constant V_{DS} of 0.3 V.

7.1.3 Result and Discussion

In this section, the functionalized monolayer HEMT substrate is studied by varying the salt concentrations from 10 mM to 150 mM to investigate the influence of the screening length. Furthermore, two different monolayer compositions, with 2 mol% DGS-NTA and 0.5 mol%, are analyzed in relation to how the concentration of NTA impacts electrostatic interactions and the screening effect.

Before salt variation, the membrane coating and eGFP binding were confirmed by measuring the transfer curves after the membrane incubation, followed by the addition of eGFP overnight. Figure 7.2 shows the I-V curves, I_{DS} plotted against V_G , where the gray curve represents the membrane (Ctrl) and the green one the eGFP attachment. Previous work by S. Mehlhose has shown that the variation in the I-V curves is due to the changes in the charged molecules that finally affect the response of the transistor. Starting with the monolayer, which is saturated with Ni^{2+} , it forms an octahedral chelating complex with NTA. The incorporation of Ni^{2+} into the monolayer results in a change in the net molecular charge of $-1 e^-$. The His-tagged eGFP binds to the Ni^{2+} in the Ni-NTA complex by displacing the water molecules in the complex [96]. The net charge of eGFP is pH-dependent. As previously reported by M. Tanaka et al., the isoelectric point of eGFP is estimated to be 4.8-5.0.[131]. At a physiological pH of 7.5, eGFP carries a negative charge, while at pH levels below the isoelectric point, it carries a net positive charge. The addition of eGFP leads to charge neutralization.

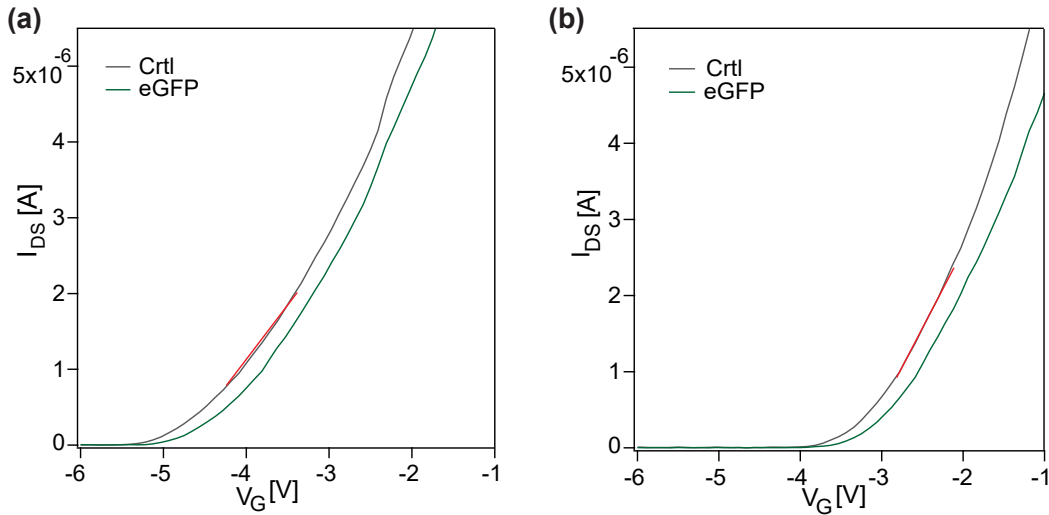


Figure 7.2: (a) Transfer curves (I_{DS} vs. V_G) of DOPC: cholesterol:NTA (2 mol%) monolayer (Ctrl) and 10 mM eGFP with 2 mol% NTA (b) with 0.5 mol% NTA

The threshold voltage (V_{th}) was identified from the I-V curves through linear regression within the ranges of $V_G = -2.88$ V to -2.22 V for the 2 mol% NTA membrane and from

$V_G = -3.53$ V to -2.59 V for the membrane with 0.5 mol% NTA. This is illustrated by the slope highlighted in red on the graph. On the NTA-incorporated membrane, the addition of eGFP resulted in a significant shift in the I-V curve. Before addition, the threshold voltage for 2 mol% NTA was -4.41 V, which shifted to -4.28 V after incorporation of eGFP. This represents a shift of $\Delta V_{th} = 0.13$ V.

eGFP changes the charge distribution (almost complete neutralization of the -1 charge of the complex) [96], thus affecting the surface potential. The drain-source current decreases, and a higher gate voltage is required to initiate conduction.

The changes in the Ni-NTA molar fraction within the monolayer affect the amount of available binding sites for protein attachment, thereby altering the surface potential. At a molar fraction of 2 mol% NTA, the effective density of binding sites for a single eGFP is estimated to be 30 nm^2 , corresponding to an average distance of $\langle d \rangle = 5.5$ nm to the neighboring NTA binding site. In contrast, when the molar fraction is decreased to 0.5 mol%, the density of binding sites drops to 120 nm^2 per eGFP, with an average distance of $\langle d \rangle = 11$ nm. For membranes with 0.5 mol% NTA lipids, a decrease in the threshold voltage response is observed due to less binding sites for eGFP. The threshold voltage before the addition was determined to be -3.28 V, while after binding at the complex, it resulted in $V_{th} = -3.17$ V, a ΔV_{th} of 0.11 V. For 0.5 mol% NTA, the same trend as for 2 mol% NTA membrane can be observed.

Next, the concentration of NaCl was gradually increased to investigate the influence of ionic strength on the system's behavior. Membranes containing 2 mol% and 0.5 mol% NTA lipids were measured under varying NaCl concentrations (10 mM, 25 mM, 50 mM, 100 mM, and 150 mM) with a flow rate of $0.5 \mu\text{L}/\text{min}$. The resulting behavior of I_{DS} as a function V_G is shown in Figures 7.3 (a) and (b), with the corresponding data summarized in table 12. The values of ΔV_{th} were calculated based on the following:

$$\Delta V_{th} = V_{th}(V_G = x) - V_{th}(V_G(150 \text{ mM})) \quad (56)$$

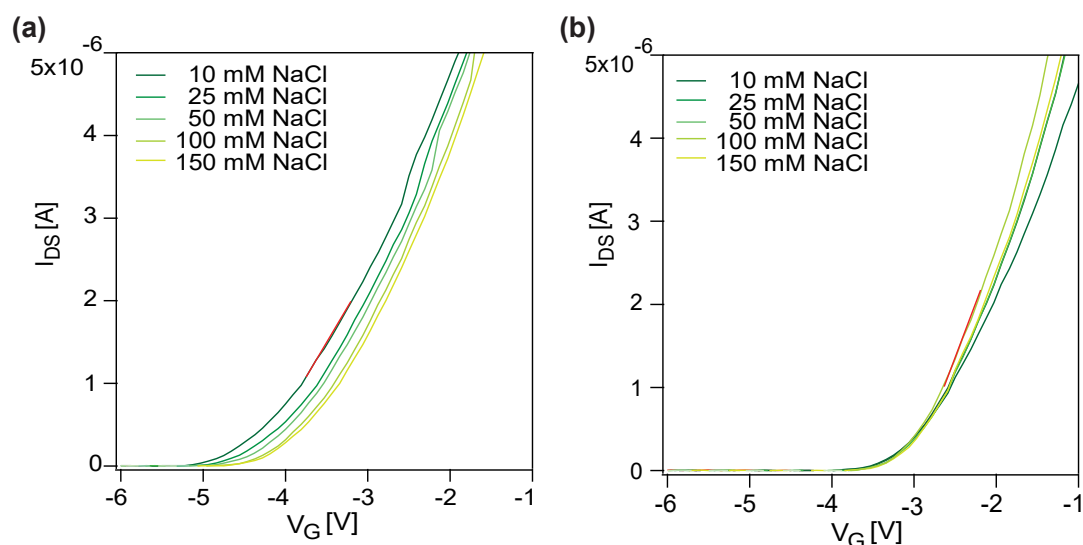


Figure 7.3: (a) Transfer curves (I_{DS} vs. V_G) of DOPC: cholesterol:NTA (2mol%) monolayer at different concentrations of NaCl. and (b) with 0.5 mol% NTA

Table 12: Summarized values for threshold voltage (V_{th}) and Debye Screening Wave Vector for the range of 10 mM - 150 mM NaCl with 2 mol% and 0.5 mol% NTA.

Conc. of NaCl [mM]	V_{th} of eGFP [V]		ΔV_{th} [V]		κ [m^{-1}]
	(2 mol% NTA)	(0.5mol% NTA)	(2 mol% NTA)	(0.5mol% NTA)	
10	-4.28	-3.17	0.36	0.07	4.7×10^8
25	-4.12	-3.14	0.20	0.04	6.2×10^8
50	-4.06	-3.13	0.14	0.03	8.1×10^8
100	-3.95	-3.11	0.04	0.01	1.1×10^9
150	-3.92	-3.10	0	0	1.3×10^9

Both membranes, figures 7.3(a) and (b) show a similar trend: as NaCl concentration increases, the I-V curves shift to more positive V_G , indicating the screening effect of NaCl ions. This decrease in electrostatic interactions at higher NaCl levels is consistent with the behavior of charged membranes when exposed to electrolytes[132]. As expected, the difference in binding site density leads to a weaker sensor response, while the trend remains the same.

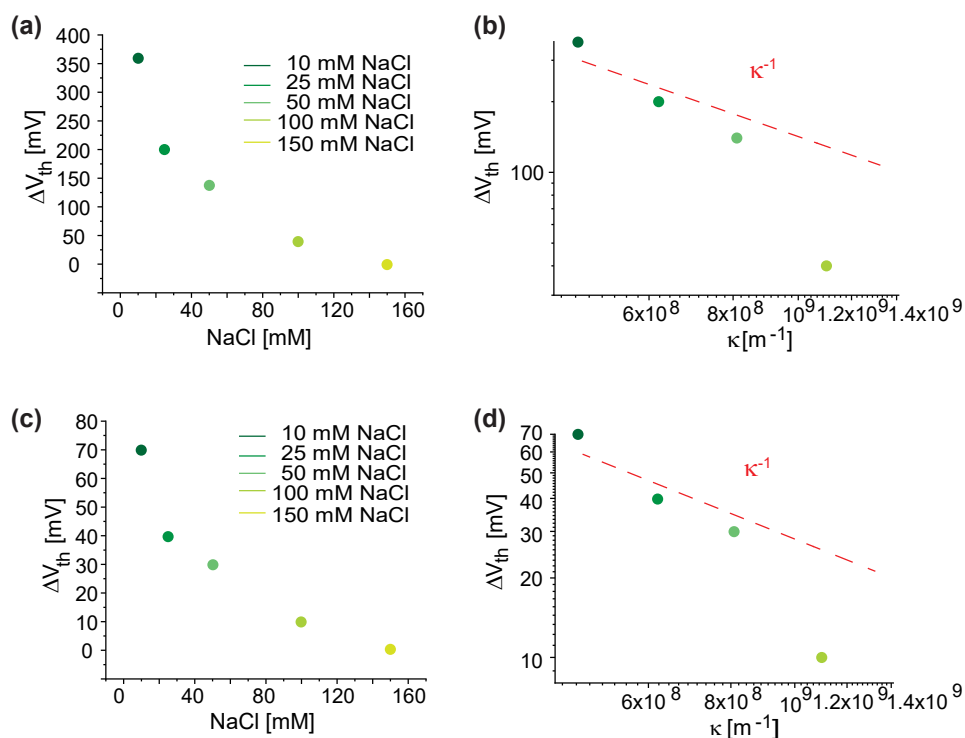


Figure 7.4: ΔV_{th} plotted against different NaCl concentrations (10 - 150 mM), with (a) 2 mol% NTA and (c) 0.5 mol% NTA incorporated into the membrane matrix. (b)+(d) ΔV_{th} plotted against the Debye screening vector for the different salt concentrations for (b) 2 mol% NTA and (d) 0.5 mol % NTA

To analyze the relationship between the shift in the threshold voltage ΔV_{th} and the Debye screening effect, the change in V_{th} (ΔV_{th}) derived from the equation 56 was plotted against the Debye screening wave vector κ^{-1} , with κ^{-1} values varying from 0.76 nm to 2.15 nm (see Figure 7.4). Figure 7.4 shows that ΔV_{th} decreases consistently as κ increases, which aligns well with the expected behavior of electrostatic screening in ionic environments. At lower salt concentrations, only a limited amount of eGFP-bound proteins can be detected. In contrast, at higher salt concentrations, the Debye length decreases, which reduces the electrostatic interactions between the surface charges and the surrounding environment. As a result, there is a smaller change in the threshold voltage. For example, for 2 mol% NTA a $\Delta V_{th} = 0.36$ mV is obtained. In contrast, for 0.5 mol% NTA $\Delta V_{th} = 0.07$ mV, as approximately five times smaller. As shown previously, this reduction can be attributed to the decreased binding density of eGFP. This exhibits a comparable trend of decreased

sensitivity at increased ionic strength.

This finding agrees with previously reported investigations by Lud et al. [106], where the authors focused on thin-film resistor-based sensors functionalized with peptides and proteins. They found that the variation of the salt concentration led to the modulation of the sensor response. The electrostatic interaction at the sensor surface and, consequently, the surface potential are impacted by altering the debye length. This study demonstrated that the response and sensitivity of the sensor were significantly impacted by different salt concentrations.

7.2 Structural and Spectroscopic characterization of supported Sarcoplasmic Reticulum (SR) Membranes on solid substrates (SI)

These figures represent an extension to section 5.1. A four slab model was applied to fit the XRR and NR data. Additionally, a water layer was inserted between the silicon oxide layer and the inner head group. With this, it can be proven that even with the addition of a water layer, the fitting quality is not affected. A water thickness of $6 \pm 1 \text{ \AA}$ was obtained. This water thickness agrees with the previous study, which was found under the supported lipid membrane [133] [18].

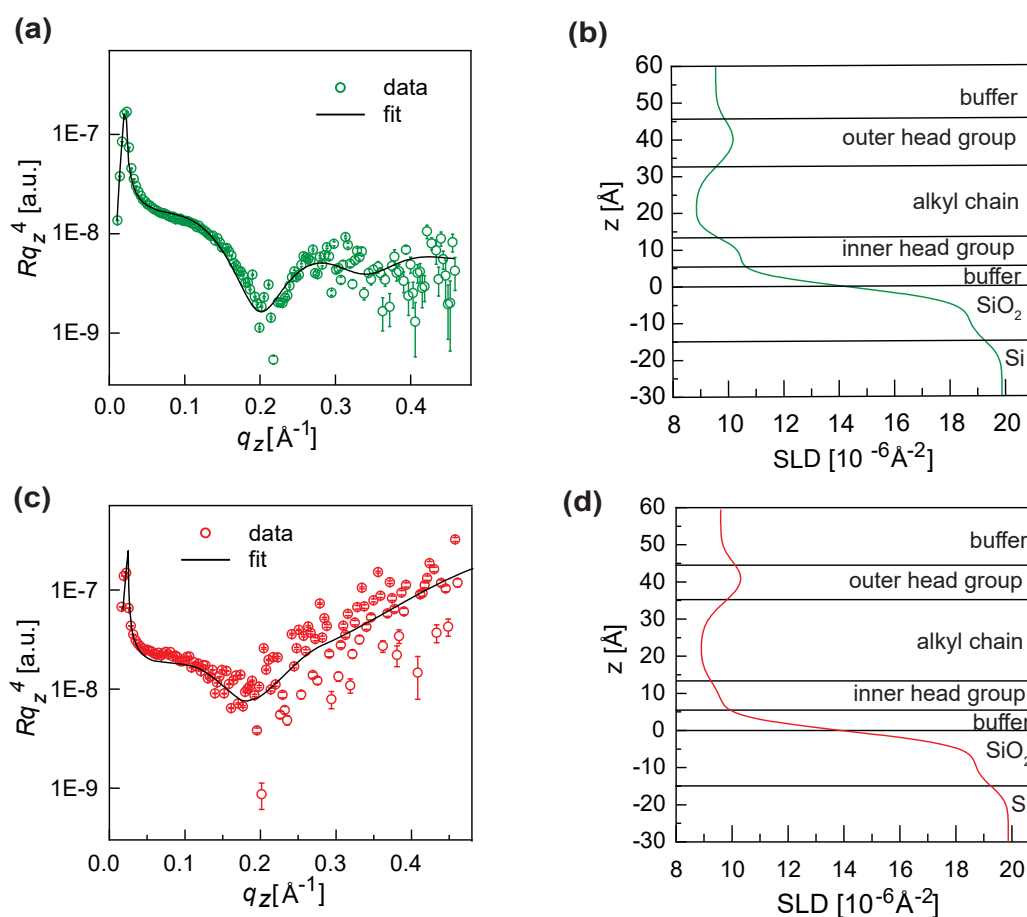


Figure 7.5: X-ray reflectivity data (symbol) and best-fit results (black solid line) of (a) + Sarcoplasmic reticulum on a silicon substrate and (b) SLD profile along the z-axis, (c)+(d) neutron reflectivity (symbol) and best-fit results (black solid line), SLD profile.

References

- [1] B. Alberts, A. Johnson, J. Lewis, P. Walter, M. Raff, and K. Roberts, *Molecular Biology of the Cell 4th Edition*. Routledge, 2002.
- [2] V. Percec and T. K. Bera, “Cell membrane as a model for the design of semifluorinated ion-selective nanostructured supramolecular systems,” *Tetrahedron*, vol. 58, no. 20, pp. 4031–4040, 2002, Fluorous Chemistry.
- [3] M. Tanaka and E. Sackmann, “Nature,” *Polymer-supported membrane as models of cell surface*, vol. 437, pp. 656–663, 2005.
- [4] E. Gorter and F. Grendel, “ON BIMOLECULAR LAYERS OF LIPOIDS ON THE CHROMOCYTES OF THE BLOOD,” *Journal of Experimental Medicine*, vol. 41, no. 4, pp. 439–443, 1925.
- [5] S. J. Singer and G. L. Nicolson, “The fluid mosaic model of the structure of cell membranes,” *Science*, vol. 175, pp. 720–731, 1972.
- [6] X. Cheng and J. C. Smith, “Biological membrane organization and cellular signaling,” *Chemical Reviews*, vol. 119, no. 9, pp. 5849–5880, 2019.
- [7] R. Lipowsky and E. Sackmann, *Structure and Dynamics of Membranes: I. From Cells to Vesicles / II. Generic and Specific Interactions*. Elsevier Science, 1995.
- [8] C. Safinya and J. Radler, *Handbook of Lipid Membranes: Molecular, Functional, and Materials Aspects*. CRC Press, 2021.
- [9] F. Weissenfeld, L. Wesenberg, M. Nakahata, M. Müller, and M. Tanaka, “Modulation of wetting of stimulus responsive polymer brushes by lipid vesicles: Experiments and simulations,” *Soft Matter*, vol. 19, pp. 2491–2504, 14 2023.
- [10] Z. Salamon, H. Macleod, and G. Tollin, “Surface plasmon resonance spectroscopy as a tool for investigating the biochemical and biophysical properties of membrane protein systems. i: Theoretical principles,” *Biochimica et Biophysica Acta (BBA) - Reviews on Biomembranes*, vol. 1331, no. 2, pp. 117–129, 1997.

REFERENCES

- [11] P. Parkkila, M. Elderdfi, A. Bunker, and T. Viitala, “Biophysical characterization of supported lipid bilayers using parallel dual-wavelength surface plasmon resonance and quartz crystal microbalance measurements,” *Langmuir*, vol. 34, no. 27, pp. 8081–8091, 2018.
- [12] L. Bar, M. E. Villanueva, S. Neupane, G. Cordoyiannis, and P. Losada-Pérez, “QCM-D Study of the Formation of Solid-Supported Artificial Lipid Membranes: State-of-the-Art, Recent Advances, and Perspectives,” *Physica Status Solidi Applied Research*, vol. 220, no. 22, p. 2200625, 2023.
- [13] C. Keller, K. Glasmästar, P. V. Zhdanov, and B. Kasemo, “Formation of supported membranes from vesicles,” *Phys. Rev. Lett.*, vol. 84, pp. 5443–5446, 2000.
- [14] F. Schwörer, M. Trapp, X. Xu, *et al.*, “Drastic swelling of lipid oligobilayers by polyelectrolytes: A potential molecular model for the internal structure of lubricating films in mammalian joints,” *Langmuir*, vol. 34, no. 4, pp. 1287–1299, 2018.
- [15] F. F. Rossetti, E. Schneck, G. Fragneto, O. V. Konovalov, and M. Tanaka, “Generic role of polymer supports in the fine adjustment of interfacial interactions between solid substrates and model cell membranes,” *Langmuir*, vol. 31, no. 15, pp. 4473–4480, 2015.
- [16] S. Johnson, T. Bayerl, D. McDermott, *et al.*, “Structure of an adsorbed dimyristoylphosphatidylcholine bilayer measured with specular reflection of neutrons,” *Biophysical Journal*, vol. 59, no. 2, pp. 289–294, 1991.
- [17] M.-L. Ainalem, N. Kristen, K. J. Edler, F. Höök, E. Sparr, and T. Nylander, “Dna binding to zwitterionic model membranes,” *Langmuir*, vol. 26, no. 7, pp. 4965–4976, 2010.
- [18] B. EbrahimiPour, A. Stöcklin, C. Busch, *et al.*, “Structural and spectroscopic characterization of supported sarcoplasmic reticulum membranes on solid substrates,” *Langmuir*, vol. 40, pp. 22168–22176, 2024.

REFERENCES

- [19] M.Nakahata, A.Sumuya, Y.Ikemoto, *et al.*, “Hyperconfined bio-inspired polymers in integrative flow-through systems for highly selective removal of heavy metal ions,” *Nat Commun*, p. 5824, 2024.
- [20] R.Dixit, Wasiullah, D.Malaviya, *et al.*, “Bioremediation of heavy metals from soil and aquatic environment: An overview of principles and criteria of fundamental processes,” *Sustainability*, vol. 7, pp. 2189–2212, 2015.
- [21] A. Yamamoto, T. Ikarashi, T. Fukuma, *et al.*, “Ion-specific nanoscale compaction of cysteine-modified poly(acrylic acid) brushes revealed by 3d scanning force microscopy with frequency modulation detection,” *Nanoscale Adv*, vol. 4, pp. 5027–5036, 23 2022.
- [22] G. Steinhoff, M. Hermann, W. J. Schaff, L. F. Eastman, M. Stutzmann, and M. Eickhoff, “Ph response of gan surfaces and its application for ph-sensitive field-effect transistors,” *Applied Physics Letters*, vol. 83, no. 1, pp. 177–179, Jul. 2003.
- [23] G. Steinhoff, O. Purruicker, M. Tanaka, M. Stutzmann, and M. Eickhoff, “Algal-n—a new material system for biosensors,” *Advanced Functional Materials*, vol. 13, no. 11, pp. 841–846, 2003.
- [24] B. Baur, G. Steinhoff, J. Hernando, *et al.*, “Chemical functionalization of gan and aln surfaces,” *Applied Physics Letters*, vol. 87, no. 26, p. 263 901, Dec. 2005.
- [25] N. Frenkel, J. Wallys, S. Lippert, *et al.*, “High precision, electrochemical detection of reversible binding of recombinant proteins on wide bandgap gan electrodes functionalized with biomembrane models,” *Advanced Functional Materials*, vol. 24, no. 31, pp. 4927–4934, 2014.
- [26] S. Mehlhose, N. Frenkel, H. Uji, *et al.*, “Flexible modulation of electronic band structures of wide band gap gan semiconductors using bioinspired, nonbiological helical peptides,” *Advanced Functional Materials*, vol. 28, no. 2, p. 1 704 034, 2018.

REFERENCES

- [27] E. Schneck, T. Schubert, O. V. Konovalov, *et al.*, “Quantitative determination of ion distributions in bacterial lipopolysaccharide membranes by grazing-incidence x-ray fluorescence,” *Proceedings of the National Academy of Sciences*, vol. 107, no. 20, pp. 9147–9151, 2010.
- [28] W. Abuillan, E. Schneck, A. Körner, *et al.*, “Physical interactions of fish protamine and antiseptic peptide drugs with bacterial membranes revealed by combination of specular x-ray reflectivity and grazing-incidence x-ray fluorescence,” *Phys. Rev. E*, vol. 88, no. 11, p. 012 705, 1 Jul. 2013.
- [29] J. Thoma, W. Abuillan, I. Furikado, *et al.*, “Specific localisation of ions in bacterial membranes unravels physical mechanism of effective bacteria killing by sanitiser,” *Scientific Reports*, vol. 10, 2020.
- [30] R. G. Oliveira, E. Schneck, B. E. Quinn, *et al.*, “Crucial roles of charged saccharide moieties in survival of gram negative bacteria against protamine revealed by combination of grazing incidence x-ray structural characterizations and monte carlo simulations,” *Phys. Rev. E*, vol. 81, p. 041 901, 4 Apr. 2010.
- [31] M. F. Schneider, K. Lim, G. G. Fuller, and M. Tanaka, “Rheology of glycocalix model at air/water interface,” *Phys. Chem. Chem. Phys.*, vol. 4, pp. 1949–1952, 10 2002.
- [32] M. Tanaka, A. P. Wong, F. Rehfeldt, M. Tutus, and S. Kaufmann, “Selective deposition of native cell membranes on biocompatible micropatterns,” *Journal of the American Chemical Society*, vol. 126, no. 10, pp. 3257–3260, 2004.
- [33] M. Tutus, S. Kaufmann, I. M. Weiss, and M. Tanaka, “Functional coating of porous silica microparticles with native biomembranes towards portable flow-through biochemical microreactors,” *Advanced Functional Materials*, vol. 22, no. 23, pp. 4873–4878, 2012.
- [34] J. D. Smith, J. A. Rowe, M. K. Higgins, and T. Lavstsen, “Malaria’s deadly grip: Cytoadhesion of *Plasmodium falciparum*-infected erythrocytes,” *Cellular Microbiology*, vol. 15, no. 12, pp. 1976–1983, 2013.

REFERENCES

- [35] M. Cyrklaff, C. P. Sanchez, N. Kilian, *et al.*, “Hemoglobins s and c interfere with actin remodeling in plasmodium falciparum-infected erythrocytes,” *Science*, vol. 334, no. 6060, pp. 1283–1286, 2011.
- [36] B. Fröhlich, A. K. Dasanna, C. Lansche, *et al.*, “Functionalized supported membranes for quantifying adhesion of p. falciparum-infected erythrocytes,” *Biophysical Journal*, vol. 120, no. 16, pp. 3315–3328, 2021.
- [37] B. Fröhlich, J. Jäger, C. Lansche, *et al.*, “Hemoglobin s and c affect biomechanical membrane properties of p. falciparum-infected erythrocytes,” *Communications Biology*, vol. 2, p. 311, 2019.
- [38] R. M. Fairhurst, D. I. Baruch, N. J. Brittain, *et al.*, “Abnormal display of pfemp-1 on erythrocytes carrying haemoglobin c may protect against malaria,” *Nature*, vol. 435, no. 7045, 1117—1121, Jun. 2005.
- [39] S. Qiang, “The hydrophobic effects: Our current understanding,” *Molecules*, vol. 27, no. 20, 2022.
- [40] C. Walker, “The hydrophobic effect: Formation of micelles and biological membranes,” *FEBS Letters*, vol. 124, no. 1, pp. 127–127, 1981.
- [41] J. N. Israelachvili, D. J. Mitchell, and B. W. Ninham, “Theory of self-assembly of lipid bilayers and vesicles.,” *Biochimica et biophysica acta*, vol. 470 2, pp. 185–201, 1977.
- [42] C. McAuliffe, “Solubility in water of paraffin, cycloparaffin, olefin, acetylene, cycloolefin, and aromatic hydrocarbons1,” *The Journal of Physical Chemistry*, vol. 70, no. 4, pp. 1267–1275, 1966.
- [43] D. van der Spoel, P. J. van Maaren, P. Larsson, and N. Timneanu, “Thermodynamics of hydrogen bonding in hydrophilic and hydrophobic media,” *The Journal of Physical Chemistry B*, vol. 110, no. 9, pp. 4393–4398, 2006.
- [44] E. Sackmann, “Chapter 1 - biological membranes architecture and function,” 1995.

REFERENCES

- [45] G. van Eck, L. Chiappisi, and S. de Beer, "Fundamentals and applications of polymer brushes in air," *ACS Applied Polymer Materials*, vol. 4, no. 5, pp. 3062–3087, 2022.
- [46] C. J. Reese and S. G. Boyes, "New methods in polymer brush synthesis: Non-vinyl-based semiflexible and rigid-rod polymer brushes," *Progress in Polymer Science*, vol. 114, p. 101 361, 2021.
- [47] W. Hu, *Polymer Physics: A Molecular Approach*. Springer Vienna, 2012.
- [48] W. Briels and J. J. Padding, "Theory of polymer dynamics," 2007.
- [49] R. Jones, *Soft Condensed Matter*. OUP Oxford, 2002.
- [50] M. Doi, S. Edwards, and S. Edwards, *The Theory of Polymer Dynamics*. Clarendon Press, 1988.
- [51] F. Tanaka, *Polymer Physics: Applications to Molecular Association and Thermoreversible Gelation*. Cambridge University Press, 2011.
- [52] W. Kuhn and F. Grün, "Beziehungen zwischen elastischen konstanten und dehnungsdoppelbrechung hochelastischer stoffe," *Kolloid-Zeitschrift*, vol. 101, pp. 248–271, 1942.
- [53] P. J. Flory, "Statistical Thermodynamics of Semi-Flexible Chain Molecules," *Proceedings of the Royal Society of London Series A*, vol. 234, no. 1196, pp. 60–73, Jan. 1956.
- [54] M. Fixman, "Radius of Gyration of Polymer Chains," *Journal of Chemical Physics*, vol. 36, no. 2, pp. 306–310, Jan. 1962.
- [55] M. Kim, S. K. Schmitt, J. W. Choi, J. D. Krutty, and P. Gopalan, "From self-assembled monolayers to coatings: Advances in the synthesis and nanobio applications of polymer brushes," *Polymers*, vol. 7, no. 7, pp. 1346–1378, 2015.
- [56] M. Tolan, "X-ray scattering from soft-matter thin films: Materials science and basic research," 1998.

REFERENCES

- [57] N.Backmann, N.Kappeler, T.Braun, *et al.*, “Sensing surface pegylation with micro-cantilevers,” *Beilstein journal of nanotechnology*, vol. 1, pp. 3–13, 2010.
- [58] M. P. Weir and A. J. Parnell, “Water soluble responsive polymer brushes,” *Polymers*, vol. 3, no. 4, pp. 2107–2132, 2011.
- [59] Y.Lan, J.Li, W.Wong-Ng, R.M.Derbeshi, J.Li, and A.Lisfi, “Free-standing self-assemblies of gallium nitride nanoparticles: A review,” *Micromachines*, vol. 7, no. 9, 2016.
- [60] A.Liu, Y.Lai, H.Chen, A.Chiu, and H.Kuo, “A brief overview of the rapid progress and proposed improvements in gallium nitride epitaxy and process for third-generation semiconductors with wide bandgap,” *Micromachines*, vol. 14, no. 4, 2023.
- [61] N.Fichtenbaum, M.Giandalia, S.Sharma, and J.Zhang, “Half-bridge gan power ics: Performance and application,” *IEEE Power Electronics Magazine*, vol. 4, no. 3, pp. 33–40, 2017.
- [62] O. Ambacher, J. Smart, J. R. Shealy, *et al.*, “Two-dimensional electron gases induced by spontaneous and piezoelectric polarization charges in n- and ga-face algan/gan heterostructures,” *Journal of Applied Physics*, vol. 85, no. 6, pp. 3222–3233, Mar. 1999.
- [63] T. Lei, M. Fanciulli, R. J. Molnar, T. D. Moustakas, R. J. Graham, and J. Scanlon, “Epitaxial growth of zinc blende and wurtzitic gallium nitride thin films on (001) silicon,” *Applied Physics Letters*, vol. 59, no. 8, pp. 944–946, Aug. 1991.
- [64] A. Allred, “Electronegativity values from thermochemical data,” *Journal of Inorganic and Nuclear Chemistry*, vol. 17, no. 3, pp. 215–221, 1961.
- [65] O. Ambacher, B. Foutz, J. Smart, *et al.*, “Two dimensional electron gases induced by spontaneous and piezoelectric polarization undoped and doped algan/gan heterostructures,” *Journal of Applied Physics*, vol. 87, pp. 334–344, Jan. 2000.

REFERENCES

- [66] I. P. Smorchkova, C. R. Elsass, J. P. Ibbetson, *et al.*, “Polarization-induced charge and electron mobility in algan/gan heterostructures grown by plasma-assisted molecular-beam epitaxy,” *Journal of Applied Physics*, vol. 86, no. 8, pp. 4520–4526, Oct. 1999.
- [67] S. Sze, *Semiconductor Devices: Physics and Technology*. Wiley, 1985.
- [68] F. Thuselt, *Physik der Halbleiterbauelemente: Einführendes Lehrbuch für Ingenieure und Physiker*. Springer Berlin Heidelberg, 2011.
- [69] S.M.Luber, K.Adlkofer, U. Rant, *et al.*, “Liquid phase sensors based on chemically functionalized gaas/algaas heterostructures,” *Physica E: Low-dimensional Systems and Nanostructures*, vol. 21, no. 2, pp. 1111–1115, 2004.
- [70] A. Biswas, A. Islam, R. Chaujar, and O. Jaksic, *Microelectronics, Circuits and Systems: Select Proceedings of Micro2021*. Springer Nature Singapore, 2023.
- [71] A. L. Linsebigler, G. Lu, and J. T. J. Yates, “Photocatalysis on tio₂ surfaces: Principles, mechanisms, and selected results,” *Chemical Reviews*, vol. 95, no. 3, pp. 735–758, 1995.
- [72] E. B. Treidel, “Gan based hemts for high voltage operation. design, technology and characterization,” Ph.D. dissertation, Technical University of Berlin, 2012.
- [73] V.Hemaja and D.Panda, “A comprehensive review on high electron mobility transistor (hemt) based biosensors: Recent advances and future prospects and its comparison with si-based biosensor,” *Silicon*, vol. 14, pp. 1–14, Apr. 2022.
- [74] D.Neamen, *Semiconductor Physics And Devices*. McGraw-Hill Education, 2003, ISBN: 9780072321074.
- [75] T. Russell, “X-ray and neutron reflectivity for the investigation of polymers,” *Materials Science Reports*, vol. 5, no. 4, pp. 171–271, 1990.
- [76] R. Thomas, “Neutron reflection from liquid interfaces,” *Annual Review of Physical Chemistry*, vol. 55, no. Volume 55, 2004, pp. 391–426, 2004.

REFERENCES

- [77] M. Born, E. Wolf, and A. Bhatia, *Principles of Optics: Electromagnetic Theory of Propagation, Interference and Diffraction of Light*. Cambridge University Press, 1999.
- [78] A. Gibaud and G. Vignaud, “Specular reflectivity from smooth and rough surfaces,” in *X-ray and Neutron Reflectivity: Principles and Applications*, J. Daillant and A. Gibaud, Eds. Berlin, Heidelberg: Springer Berlin Heidelberg, 2009, pp. 85–131.
- [79] L. G. Parratt, “Surface studies of solids by total reflection of x-rays,” *Physical Review*, vol. 95, pp. 359–369, 1954.
- [80] J. Als-Nielsen and D. McMorrow, *Elements of Modern X-ray Physics*. Wiley, 2011.
- [81] N. N. Novikova and e. Yurieva Eleonora A., “X-ray fluorescence methods for investigations of lipid/protein membrane models,” *Journal of Synchrotron Radiation*, vol. 12, no. 4, pp. 511–516, Jul. 2005.
- [82] P. T. Boggs, J. R. Donaldson, R. h. Byrd, and R. B. Schnabel, “Algorithm 676: Odrpack: Software for weighted orthogonal distance regression,” *ACM Trans. Math. Softw.*, vol. 15, no. 4, 348–364, Dec. 1989.
- [83] G. Binnig, C. F. Quate, and C. Gerber, “Atomic force microscope,” *Phys. Rev. Lett.*, vol. 56, pp. 930–933, 9 Mar. 1986.
- [84] Y. F. Dufrêne, “Atomic force microscopy, a powerful tool in microbiology,” *Journal of Bacteriology*, vol. 184, no. 19, pp. 5205–5213, 2002.
- [85] L. S. Dorobantu and M. R. Gray, “Application of atomic force microscopy in bacterial research,” *Scanning*, vol. 32, no. 2, pp. 74–96, 2010.
- [86] H. Fujiwara, *Spectroscopic Ellipsometry: Principles and Applications*. Wiley, 2007.
- [87] R. Azzam and N. Bashara, *Ellipsometry and Polarized Light*. North-Holland Publishing Company, 1977.

REFERENCES

- [88] C. Tropea, A.L. Yarin, and J.F. Foss, *Springer Handbook of Experimental Fluid Mechanics* (Springer Handbook of Experimental Fluid Mechanics). Springer, 2007, ISBN: 9783540251415.
- [89] K.L. Mittal, *Contact Angle, Wettability and Adhesion, Volume 6*. CRC Press, 2009.
- [90] R. Tadmor, "Line energy and the relation between advancing, receding, and young contact angles," *Langmuir*, vol. 20, no. 18, pp. 7659–7664, 2004.
- [91] M. K. Chaudhury and G. M. Whitesides, "Correlation between surface free energy and surface constitution," *Science*, vol. 255, 1230–1232, 1992, 339.
- [92] T. Young, "Iii. an essay on the cohesion of fluids," *Philosophical Transactions of the Royal Society of London*, vol. 95, pp. 65–87, 1805.
- [93] K.-Y. Law, "Definitions for hydrophilicity, hydrophobicity, and superhydrophobicity: Getting the basics right," *The Journal of Physical Chemistry Letters*, vol. 5, no. 4, pp. 686–688, 2014.
- [94] K. Werner and D. Puotinen, "Cleaning solutions based on hydrogen peroxide for use in silicon semiconductor technology," 1970.
- [95] J. Brzoska, N. Shahidzadeh, and F. Rondelez, "Evidence of a transition temperature for the optimum deposition of grafted monolayer coatings," *nature*, vol. 360, no. 6406, pp. 719–721, Dec. 1992.
- [96] S. Mehlhose, "Biofunctionalization of gan/algan/gan high electron mobility transistors," Ph.D. dissertation, University of Heidelberg, 2019.
- [97] G. Schwoch and H. Passow, "Preparation and properties of human erythrocyte ghosts," *Molecular and Cellular Biochemistry*, vol. 2, pp. 197–218, 1973.
- [98] M. M. Bradford, "A rapid and sensitive method for the quantitation of microgram quantities of protein utilizing the principle of protein-dye binding," *Analytical Biochemistry*, vol. 72, no. 1, pp. 248–254, 1976.
- [99] W. Hasselbach, "Die calciumpumpe der erschlaeffungsgrana des muskels und ihre abhangigkeit von der atp-spaltung," *Biochem Z*, vol. 339, pp. 94–111, 1961.

REFERENCES

- [100] U. K. Laemmli, "Cleavage of structural proteins during the assembly of the head of bacteriophage t4," *nature*, vol. 227, no. 5259, pp. 680–685, Aug. 1970.
- [101] A. Nelson, "Co-refinement of multiple-contrast neutron/x-ray reflectivity data using motofit," *Journal of Applied Crystallography*, vol. 39, pp. 273–276, Mar. 2006.
- [102] J.Thoma, "Electrostatics, mechanics, and dynamics of biological interfaces at and out of equilibrium," Ph.D. dissertation, University of Heidelberg, 2022.
- [103] W.Abuillan, "Fine-structures, lateral correlation and diffusion of membrane-associated proteins on biological membrane surfaces," Ph.D. dissertation, University of Heidelberg, 2013.
- [104] E. Sackmann, "Chapter 5 - physical basis of self-organization and function of membranes: Physics of vesicles," in *Structure and Dynamics of Membranes*, ser. Handbook of Biological Physics, R. Lipowsky and E. Sackmann, Eds., vol. 1, North-Holland, 1995, pp. 213–304.
- [105] D. Gassull, A. Ulman, M. Grunze, and M. Tanaka, "Electrochemical sensing of membrane potential and enzyme function using gallium arsenide electrodes functionalized with supported membranes," *The Journal of Physical Chemistry B*, vol. 112, no. 18, pp. 5736–5741, 2008.
- [106] A. Poghossian, M. Abouzar, F. Amberger, *et al.*, "Field-effect sensors with charged macromolecules: Characterisation by capacitance-voltage, constant-capacitance, impedance spectroscopy and atomic-force microscopy methods," *Biosensors and Bioelectronics*, vol. 22, no. 9, pp. 2100–2107, 2007, Selected Papers from the Ninth World Congress On Biosensors. Toronto, Canada 10 - 12 May 2006.
- [107] R. R. Netz, "Debye-hückel theory for interfacial geometries.," *Physical review. E, Statistical physics, plasmas, fluids, and related interdisciplinary topics*, vol. 60 3, pp. 3174–82, 1999.

REFERENCES

- [108] A. Yamamoto, K. Hayashi, A. Sumiya, *et al.*, “Modulation of viscoelasticity and interfacial potential of polyelectrolyte brush by ion-specific interactions,” *Frontiers in Soft Matter*, vol. 2, p. 959–542, 2022.
- [109] F. Rehfeldt, R. Steitz, S. P. Armes, R. von Klitzing, A. P. Gast, and M. Tanaka, “Reversible activation of diblock copolymer monolayers at the interface by pH modulation, 1: lateral chain density and conformation,” *The Journal of Physical Chemistry B*, vol. 110, no. 18, pp. 9171–9176, 2006.
- [110] A. Korytowski, W. Abuillan, A. Makky, O. Konovalov, and M. Tanaka, “Impact of lipid oxidization on vertical structures and electrostatics of phospholipid monolayers revealed by combination of specular x-ray reflectivity and grazing-incidence x-ray fluorescence,” *The Journal of Physical Chemistry B*, vol. 119, no. 30, pp. 9787–9794, 2015.
- [111] A. Makky, J. Czajor, O. Konovalov, *et al.*, “X-ray reflectivity study of the heat shock protein hsp70 interaction with an artificial cell membrane model,” *Scientific Reports*, vol. 13, p. 19 157, 2023.
- [112] M. Hildebrandt, E. Shin, S. Yang, W. Ali, S. Altinpinar, and J. S. Gutmann, “Investigation of roughness correlation in polymer brushes via x-ray scattering,” *Polymers*, vol. 12, no. 9, 2020.
- [113] C. H. Fiske and Y. Subbarow, “The colorimetric determination of phosphorus,” *Journal of Biological Chemistry*, vol. 66, no. 2, pp. 375–400, 1925.
- [114] G. Cooper and K. Adams, *The Cell: A Molecular Approach*. Oxford University Press, 2022, ISBN: 9780197583722.
- [115] M. Tanaka, “Physics of interactions at biological and biomaterial interfaces,” *Current Opinion in Colloid & Interface Science*, vol. 18, no. 5, pp. 432–439, 2013.
- [116] R. Synowicki, “Spectroscopic ellipsometry characterization of indium tin oxide film microstructure and optical constants,” *Thin Solid Films*, vol. 313–314, pp. 394–397, 1998.

REFERENCES

- [117] Y. Liu, J. Hsieh, and S. Tung, "Extraction of optical constants of zinc oxide thin films by ellipsometry with various models," *Thin Solid Films*, vol. 510, no. 1, pp. 32–38, 2006.
- [118] Y. F. Dufrêne, T. Boland, J. W. Schneider, W. R. Barger, and G. U. Lee, "Characterization of the physical properties of model biomembranes at the nanometer scale with the atomic force microscope," *Faraday Discuss.*, vol. 111, pp. 79–94, 0 1999.
- [119] C. Toyoshima and H. Nomura, "Structural changes in the calcium pump accompanying the dissociation of calcium," *Nature*, vol. 418, pp. 605–611, 2002.
- [120] C. Busch, B. Nagy, A. Stöcklin, P. Gutfreund, R. Dahint, and T. Ederth, "A mobile setup for simultaneous and in situ neutron reflectivity, infrared spectroscopy, and ellipsometry studies," *Review of Scientific Instruments*, vol. 93, no. 11, p. 114 102, Nov. 2022.
- [121] A. I. López-Lorente and B. Mizaikoff, "Mid-infrared spectroscopy for protein analysis: Potential and challenges," *Analytical and Bioanalytical Chemistry*, vol. 408, pp. 2875–2889, 2016.
- [122] A. Luchini, F. Sebastiani, F. G. Tidemand, *et al.*, "Peptide discs as precursors of biologically relevant supported lipid bilayers," *Journal of Colloid and Interface Science*, vol. 585, pp. 376–385, 2021.
- [123] A. Oliva, S. García-Carrillo, A. Ortiz, F. J. Aranda, and J. A. Teruel, "Interaction of a dirhamnolipid biosurfactant with sarcoplasmic reticulum calcium atpase (serca1a)," *Archives of Biochemistry and Biophysics*, vol. 699, p. 108 764, 2021.
- [124] D. M. Blow, "Structure and mechanism of chymotrypsin," *Accounts of Chemical Research*, vol. 9, no. 4, pp. 145–152, 1976.
- [125] M. L. Bender, "The mechanism of α -chymotrypsin-catalyzed hydrolyses1-3," *Journal of the American Chemical Society*, vol. 84, no. 13, pp. 2582–2590, 1962.
- [126] F. Rehfeldt and M. Tanaka, "Hydration forces in ultrathin films of cellulose," *Langmuir*, vol. 19, no. 5, pp. 1467–1473, 2003.

REFERENCES

- [127] M.Diez-Silva, M.Dao, J.Han, C.T.Lim, and S.Suresh, “Shape and biomechanical characteristics of human red blood cells in health and disease,” *MRS Bulletin*, vol. 35, no. 5, pp. 382–388, 2010.
- [128] V.Frank, Y.Chushkin, B.Fröhlich, *et al.*, “Lensless tomographic imaging of near surface structures of frozen hydrated malaria-infected human erythrocytes by coherent x-ray diffraction microscopy,” *Sci Rep*, vol. 7, p. 14 081, 2017.
- [129] C.Li, X.Chen, and Z.Wang, “Review of the algan/gan high-electron-mobility transistor-based biosensors: Structure, mechanisms, and applications,” *Micromachines*, vol. 15, no. 3, 2024.
- [130] H.H.Lee, M.Bae, S.-H.Jo, *et al.*, “Algan/gan high electron mobility transistor-based biosensor for the detection of c-reactive protein,” *Sensors*, vol. 15, no. 8, pp. 18 416–18 426, 2015.
- [131] M.Tanaka, J.Hermann, I.Haase, M.Fischer, and S.G.Boxer, “Frictional drag and electrical manipulation of recombinant proteins in polymer-supported membranes,” *Langmuir*, vol. 23, no. 10, pp. 5638–5644, 2007.
- [132] D.Williams, J.Vicôgne, I.Zaitseva, S.McLaughlin, and J.E.Pessin, “Evidence that electrostatic interactions between vesicle-associated membrane protein 2 and acidic phospholipids may modulate the fusion of transport vesicles with the plasma membrane,” *Molecular Biology of the Cell*, vol. 20, no. 23, pp. 4910–4919, 2009.
- [133] A. Körner, C. Deichmann, F. F. Rossetti, *et al.*, “Cell differentiation of pluripotent tissue sheets immobilized on supported membranes displaying cadherin-11,” *PLOS ONE*, vol. 8, Feb. 2013.

List of Figures

1.1	(a) Schematic-illustration of an eukaryotic cell membrane, adapted from [2], (b) Supported membranes on a solid substrate and a polymer support.	2
1.2	Plant-inspired material for the selective capture of heavy metal ions (e.g., Cd^{2+}). (a) Neutralization of Cd^{2+} ions by phytochelatin in plant cells, (b) Chemical structure of phytochelatin-inspired polymer (pAA-Cys5) and (c) Lipopolymer (DOPE-pAA-Cys5).	4
1.3	(a) Fabrication of a supported lipid monolayer incorporating DOPE-pAA-Cys5 on silanized GaN, (b) GaN/AlGaN/GaN heterostructure, device geometry, and electrochemical cell used in this study.	6
1.4	Fluorescence spectra of DOPC/DOPE-pAA-Cys5 monolayer on Cd^{2+} -free and Cd^{2+} loaded buffer.	8
1.5	Illustration of SR membranes in vivo	10
1.6	(a) Healthy erythrocyte "ghost cell" onto silicon substrates coated with cellulose film, (b) SEM images of b1, healthy erythrocyte and b2, infected erythrocyte [38]. b3 scheme of simplified membrane model showing knob structure of PfEMP1 [37].	11
2.1	Structure of lipids.	12
2.2	Graphical representation of different grafting regimes, (a) Pancake, (b) Mushroom and (c) Polymer brush.	18
2.3	Crystal structure of GaN adapted from ref. [62]	19
2.4	Graphic representation of reflection and refraction of an incident beam on a smooth surface.	25
2.5	Schematic illustration of the AFM setup.	30
2.6	Illustration of a droplet on a solid surface showing the Solid-Liquid (SL), Solid-Vapor (SV), and Liquid-Vapor (LV) interfaces.	33
3.1	Illustration of erythrocyte ghost membrane fabrication.	37
3.2	Graphical representation for determining the threshold voltage (V_{th}) based on the instrument used.	43

LIST OF FIGURES

4.1	Fluorescence microscopy image of a DOPC monolayer incorporating 2 mol% DOPE-pAA-Cys5 deposited on the ODTMS-coated glass substrate, labeled with 0.2 mol% TexasRed DHPE (Illustration of DOPC/PE-pAA-Cys5 monolayer on a glass substrate).	44
4.2	(a) and (b) Drain-source current (I_{DS}) plotted against the gate voltage (V_G) for HEMT functionalized with a DOPC/DOPE-pAA-Cys5 monolayer in the absence and the presence of 10^{-2} M – 10^{-9} M $CdCl_2$ in buffer 1 at $V_{DS} = 0.3$ V . (c) Threshold voltage V_{th} determined from the maximum conductance plotted against $\log[Cd^{2+}]$	46
4.3	(a) I_{DS} against V_G for HEMT functionalized with a DOPC/DOPE-pAA-Cys5 monolayer, measured in buffer 1 in the absence and the presence of 10^{-9} M – 10^{-2} M $CaCl_2$ at $V_{DS} = + 0.3$ V and (b) Threshold voltage V_{th} plotted against $\log[Ca^{2+}]$	48
4.4	$V_{th} - \log[M^{2+}]$ plots of the HEMT functionalized with DOPC/DOPE-pAA-Cys5 monolayer, measured in buffer 2 containing (a) Cd^{2+} and (b) Ca^{2+}	50
4.5	Pressure-area isotherms of DOPC/PE-pAA-Cys5 monolayer in (a) 100 mM NaCl + 10 mM Tris (Ctrl), (b) 100 mM NaCl + 10 mM Tris + 1 mM $CaCl_2$, (c) 100 mM NaCl + 10 mM Tris + 1 mM $CdCl_2$, (d) 100 mM NaCl+10 mM Tris + 1 mM $CdCl_2$ + 1 mM $CaCl_2$ subphase at 20° C and pH 7.4	53
4.6	(a) XRR data with best fit (black line) for DOPC/PE-pAA-Cys5 monolayer (Ctrl) (b) Reconstructed electron density profile.	54
4.7	(a)+(b) XRR data (open circles) with reconstructed electron density profiles for DOPC/PE-pAA-Cys5 monolayer in the presence of 1 mM $CdCl_2$, (c)+(d) Fluorescence intensity as a function of q_z for Cd L_α signal with corresponding ion concentration profile.	55

LIST OF FIGURES

4.8	(a)+(b) XRR data with reconstructed electron density profiles for DOPC/PE-pAA-Cys5 monolayer in the presence of 1 mM CaCl ₂ , (c) Fluorescence intensity as a function of q _z for Ca ²⁺ K _α signal. The data could not be fitted, bulk intensity is indicated by dashed line	57
4.9	(a)+(b) XRR data with reconstructed electron density profiles for DOPC/PE-pAA-Cys5 monolayer in the presence of 1 mM (CaCl ₂ + CdCl ₂), (c)+(d) Fluorescence intensity as a function of q _z for Cd ²⁺ L _α signal with corresponding ion concentration profile and (e) Fluorescence intensity as a function of q _z for Ca ²⁺ . K _α signal	58
5.1	(a) SDS-PAGE of SR membranes stained with Coomassie blue shows the following: lane 1 displays the molecular weight standard and lane 2 contains SR membranes in free suspensions. The band of Ca ²⁺ -ATPase (MW = 105 kDa) is marked by an arrow. (b) Immunofluorescence microscopy image of SR membranes on a glass substrate, labeled with anti-Ca ²⁺ -ATPase.(c) Fluorescence microscopy image of supported lipid-labeled SR membrane on a glass substrate, doped with 0.2 mol% TexasRed DHPE.	62
5.2	X-ray reflectivity data (symbol) and best-fit results (black solid line) of (a) Sarcoplasmic reticulum on a silicon substrate and (b) SLD profile along the z-axis, (c) and (d) Neutron reflectivity data (symbol) and best-fit results (black solid line), SLD profile.	64
5.3	X-ray reflectivity data (symbol) and best-fit results (black solid line) of (a) Sarcoplasmic reticulum on a silicon substrate and (b) SLD profile along the z-axis, (c) and (d) neutron reflectivity data (symbol) and best-fit results (black solid line), SLD profile.	66
5.4	(a) ATR-FTIR spectra of a supported SR membrane treated chymotrypsin over 15 h (color code indicates change over time) (b) Intensity vs. time for the protein peak (amide I band, ν ≈ 1650 cm ⁻¹) and lipids (asymmetric CH ₂ stretching band, ν ≈ 2920 cm ⁻¹). A binning factor of 10 has been applied to the data. (c) Variation of relative peak intensities over time, as shown in panel (b).	68

LIST OF FIGURES

5.5	Contact angle measurement on TMSC (a) before and (b) after regeneration with HCl. (c) Tapping-AFM image of cellulose after regeneration on air, scan size: 10x10 μm (d) Band 3 immunofluorescence image of healthy erythrocyte ghost membrane on optimized cellulose.	70
5.6	NR data of dry cellulose with corresponding SLD profile, (a)+(b) Sample A and (c)+(d) Sample B	72
5.7	NR data of hydrated cellulose along with corresponding SLD profile, (a)+(b) Sample A and (c)+(d) Sample B	74
5.8	(a)+(b) NR data of healthy erythrocyte ghost along with corresponding SLD profile, and (c)+(d) infected erythrocyte ghost with the corresponding SLD profile	76
7.1	(a) HEMT functionalized surface with ODTMS and lipid composition (DOPC:Cholesterol:NTA)	82
7.2	(a) Transfer curves (I_{DS} vs. V_G) of DOPC: cholesterol:NTA (2 mol%) monolayer (Ctrl) and 10 mM eGFP with 2 mol% NTA (b) with 0.5 mol% NTA	84
7.3	(a) Transfer curves (I_{DS} vs. V_G) of DOPC: cholesterol:NTA (2mol%) monolayer at different concentrations of NaCl. and (b) with 0.5 mol% NTA	86
7.4	ΔV_{th} plotted against different NaCl concentrations (10 - 150 mM)	87
7.5	X-ray reflectivity data (symbol) and best-fit results (black solid line) of (a) + Sarcoplasmic reticulum on a silicon substrate and (b) SLD profile along the z-axis, (c)+(d) neutron reflectivity (symbol) and best-fit results (black solid line), SLD profile.	89

LIST OF TABLES

List of Tables

1	Lattice constants, spontaneous polarization of GaN and AlN [65]	19
2	List of ΔV_{th} and ΔG_{max} for Cd^{2+} and Ca^{2+} ions in buffer 1.	47
3	List of ΔV_{th} and ΔG_{max} for Cd^{2+} and Ca^{2+} ions in buffer 2.	50
4	Thickness d , scattering length density (SLD) and roughness (σ)	60
5	Thickness, SLD, and roughness of a supported SR membrane determined by XRR measurement	65
6	Thickness, SLD, and roughness of a supported SR membrane after enzymatic digestion as determined by XRR/NR measurement	67
7	Thickness, SLD, and roughness of dry cellulose (Sample A, for healthy erythrocyte ghost system)	73
8	Thickness, SLD, and roughness of dry cellulose (Sample B, for infected erythrocyte ghost system)	73
9	Thickness, SLD, and roughness of hydrated cellulose (Sample A, for healthy erythrocyte ghost system)	74
10	Thickness, SLD, and roughness of hydrated cellulose (Sample B, for infected erythrocyte ghost system)	75
11	Thickness, SLD, and roughness of healthy and infected erythrocyte ghost membranes	77
12	Summarized values for threshold voltage (V_{th}) and Debye Screening Wave Vector for the range of 10 mM - 150 mM NaCl with 2 mol% and 0.5 mol% NTA.	86